



# Imagerie multispectrale pour améliorer la détection des lésions précancéreuses en endoscopie digestive

Sergio Ernesto Martinez Herrera

## ► To cite this version:

Sergio Ernesto Martinez Herrera. Imagerie multispectrale pour améliorer la détection des lésions précancéreuses en endoscopie digestive. Médecine humaine et pathologie. Université Paris Saclay (COmUE), 2016. Français. NNT : 2016SACLV055 . tel-01385103

**HAL Id: tel-01385103**

**<https://theses.hal.science/tel-01385103>**

Submitted on 20 Oct 2016

**HAL** is a multi-disciplinary open access archive for the deposit and dissemination of scientific research documents, whether they are published or not. The documents may come from teaching and research institutions in France or abroad, or from public or private research centers.

L'archive ouverte pluridisciplinaire **HAL**, est destinée au dépôt et à la diffusion de documents scientifiques de niveau recherche, publiés ou non, émanant des établissements d'enseignement et de recherche français ou étrangers, des laboratoires publics ou privés.

NNT : 2016SACLV055



THESE DE DOCTORAT  
DE  
L'UNIVERSITE PARIS-SACLAY  
PREPAREE A  
L'UNIVERSITE VERSAILLES SAINT-QUENTIN EN YVELINES

ÉCOLE DOCTORALE N°577  
Structure et dynamique des systèmes vivants

Spécialité de doctorat : Sciences de la Vie et de la Santé

Par

**M Sergio Ernesto MARTINEZ HERRERA**

Multispectral imaging to improve the detection of  
precancerous lesions in digestive endoscopy

**Thèse présentée et soutenue à Palaiseau, le 19 juillet 2016 :**

**Composition du Jury :**

Mme. Sylvie TREUILLET  
M. Jean SEQUEIRA  
M. Arnaud DUBOIS  
M. Franck MARZANI  
M. Yannick BENEZETH  
M. Thierry PONCHON  
M. Dominique LAMARQUE  
M. François GOUDAIL

MCF HdR, Université d'Orléans  
Professeur, Aix Marseille Université  
Professeur, IOGS  
Professeur, Université de Bourgogne  
MCF, Université de Bourgogne  
MD, Professeur, Université de Lyon  
MD, Professeur, UVSQ  
Professeur, IOGS

Rapporteur  
Rapporteur et Président du jury  
Examineur  
Examineur  
Examineur  
Examineur  
Directeur de thèse  
Co-directeur de thèse



# Acknowledgements

It has been a privilege to perform research in different institutions, in the Laboratory Le2i of the Université de Bourgogne, in the Institut d'Optique Graduate School and in the Université de Versailles Saint Quentin en Yvelines. The intellectual stimulation and the good environment were propitious for scientific development. This environment depends on the people. I would like to express my thankful to all the people involved in this work.

I am deeply in debt to all my supervisors for their guidance, scientific discussions, support and infinite patience mentoring me. I would like to start with the team from Dijon, Prof. Franck Marzani and MCF Yannick Benezeth thanks for welcoming to Dijon, for sharing insights and infinite help in the development of the acquisition systems and the treatment of the data. I also would like to thank Prof. Dominique Lamarque, for your guidance and discussions on the medical field, for showing us the needs in the medical domain as well as the challenges for the new technologies. Thank you to the gastroendoscopic unit in the Hospital Ambroise Paré in Boulogne-Billancourt who helped in the conduction of this research as well as Prof. Jean Francois Emile and the people from the anatomopathological unit of the same hospital.

Thank you to the team from the Institut d'Optique Graduate School who welcomed me in Palaiseau. Prof. Francois Goudail, MCF Matthieu Boffety and MCF Hervé Sauer, for all the valuable advise during my formation as a researcher and their help in the design of the system GEMS. Special thanks to the SPIM team, Caroline, Marie-Anne, Nicolas, Lijo, Rafael, Remy, Corentin, Henri-Francois for your friendship and help at all times during the thesis. I would like also to thank the members of the mechanical workshop Andres, who designed and constructed mechanically the system GEMS and also the people from LEnsE who helped me in the optical measurements of the system.

I owe a debt to the team from the Institut Pasteur, Prof. Eliette Touatti, Valerie Michele and Laurence Fiette for their help in the model of infection of *H. pylori* and the analysis of histological samples.

Thanks to my family, who provided big efforts and sacrifices on my education, thank you for supporting my dreams. Thanks to my friends, spread around the world, which gave me hope and encouraged me to search my passion in science and also thanks to my colleagues in France and overseas, who supported me all the way up to this stage.

Special thanks to Bruno, Beto and Marcos, for your friendship, help and advice in crucial moments of research. I would like also to thank my flatmates and friends in different cities,

especially Hayyan, Remi and Julie who saw this work at different points, thank you for your friendship and support during the different challenging moments of research.

I would like to also to thank my new colleagues in Pollen metrology for the new adventure that begins providing contributions to sciences.

Finally, I would like to thank the University of Versailles Saint Quentin en Yvelines, with the IDEX Paris Saclay for the funding,

In summary: thanks to all the people who bring significant contributions to my career.

# Contents

List of figures

List of tables

List of abbreviations and symbols

Preface

Introduction

## Chapter 1

<b>Review on gastritis, precancerous lesions and their diagnosis</b>	<b>23</b>
1.1 Anatomy of the stomach	23
1.2 Evolution of gastritis	24
1.1.2.1 Chronic active gastritis, infection by <i>Helicobacter pylori</i>	24
1.1.2.2 Atrophy	25
1.2.3 Intestinal metaplasia	25
1.2.4 Dysplasia	25
1.2.5 Cancer Lesion	26
1.3 Gastroendoscopy and biopsy collection techniques for diagnosis.	27
1.3.1 Random collection of multiple biopsies from antrum and corpus	28
1.3.2 Oriented biopsies on mucosal changes	28
1.3.2.1 Narrow Band Imaging (NBI)	28
1.3.2.2 Flexible Spectral Imaging Color Enhancement (FICE)	29
1.3.2.3 i-scan	30
1.3.2.4 Chromoendoscopy	30
1.4 Summary	31

## Chapter 2

<b>Acquisition and processing of the reflectance spectrum</b>	<b>33</b>
2.1 Principles of Spectroscopy and Multispectral imaging	33
2.2 Acquisition of reflectance spectra $R(\lambda)$	35
2.2.1 Acquisition techniques	35
2.2.2 Reflectance and sensor calibration	36
2.3 Light transportation in biological tissues	36
2.3.1 Phenomena occurring during light tissue interaction	37
2.3.2 Theoretical model of light tissue interaction	39

2.4 Statistical analysis of the spectrum	42
2.4.1 Hypothesis test and p value [71], [73], [74]	42
2.4.2 Statistical non-parametric analysis	43
2.4.2.1 Analysis of variance (ANOVA) [72], [73]	43
2.4.2.2 Wilcoxon-Mann Whitney [72], [73], [76], [77]	44
2.4.2.3 Kruskal Wallis test [72], [73], [76]	45
2.5 Classification framework	45
2.5.1 Preprocessing of the spectrum	46
2.5.2 Feature extraction and selection	46
2.5.2.1 Wrapper approach	47
2.5.2.2 Filter approach	48
2.5.2.3 Embedded approach	49
2.5.3 Classification algorithms	49
2.5.3.1 K nearest neighbor [86], [88]	49
2.5.3.2 Support Vector Machine (SVM) [86], [88], [89]	50
2.5.3.3 Neural Networks using Generalized Relevance Learning Vector Quantization [90]–[94]	51
2.5.4 Evaluation of the classification performance	52
2.6 Summary	53

### Chapter 3

<b>Reflectance of gastritis pathology under controlled conditions</b>	<b>55</b>
3.1 Model of experimentation	55
3.1.1 Mice model	56
3.1.2 <i>H. pylori</i> strain SS1	56
3.2 Mice experiments	57
3.2.1 Infection by <i>H. pylori</i> strain SS1	57
3.2.2 Campaigns of acquisition	57
3.2.3 Analysis of biopsies from mice stomachs	59
3.3 Acquisition of the reflectance from mice stomachs	59
3.3.1 Spectrometer Konica Minolta CM-2600d	60
3.3.2 Multispectral camera Flux Data FD1665	60
3.3.2.1 Characteristic of the camera	60
3.3.2.2 Stomach segmentation from multispectral image	62
3.4 Bacterium colonization and histopathological results	64
3.5 Statistical analysis of the reflectance	65
3.5.1 Analysis of the control group	66
3.5.2 Analysis between inoculated and control group	68
3.5.3 Analysis between the acquisition campaigns	71
3.6 Summary	72

## **Chapter 4**

<b>Clinical study of gastritis</b>	<b>73</b>
4.1 Filter wheel based prototype for multispectral acquisition	73
4.1.1 Acquisition system	73
4.1.2 Registration of multispectral images	75
4.1.3 Processing of multispectral images	76
4.2 Database	77
4.2.1 Subjects	77
4.2.2 Collected multispectral images	77
4.3 Analysis of gastritis	78
4.3.1 Qualitative analysis of multispectral images	78
4.3.2 Statistical analysis	79
4.4 Summary	82

## **Chapter 5**

<b>Clinical studies on precancerous lesions</b>	<b>83</b>
5.1 Differentiation of precancerous lesions from the prototype based on a filter wheel	83
5.1.1 Database	84
5.1.1.1 Subjects	84
5.1.1.2 Collected multispectral images	84
5.1.2 Statistical analysis	85
5.1.3 Classification of multispectral images with precancerous lesions.	87
5.1.3.1 Balance of the database for classification tasks	87
5.1.3.2 Extraction of features	88
5.1.3.3 Feature ranking	88
5.1.3.4 Classification	89
5.1.3.5 Results of the classification	90
5.2 Identification of precancerous lesions from the prototype GEMS (Gastro Endoscope MultiSpectral)	92
5.2.1 Acquisition system	92
5.2.1.1 Gastroendoscopic unit	93
5.2.1.2 Microendoscope	93
5.2.1.3 Source of light	94
5.2.1.4 Optical relay block	97
5.2.1.5 Software for GEMS	100
5.2.2 Preprocessing of multispectral images	101
5.2.3 Database	103
5.2.3.1 Subjects	103
5.2.3.2 Collected multispectral images	104
5.2.4 Statistical analysis	104
5.2.5 Classification of multispectral images with precancerous lesions.	106



5.2.5.1 Balance of the database for classification tasks	106
5.2.5.2 Extraction of features	107
5.2.5.3 Feature ranking	107
5.2.5.4 Classification	108
5.2.5.5 Results of the classification	108
3. Summary	108
<b>Conclusions and future perspectives</b>	<b>111</b>
Annexe. Synthèse. Imagerie multispectrale pour améliorer la détection des lésions précancéreuses en endoscopie digestive	<b>115</b>
<b>Bibliography</b>	<b>117</b>

# List of figures

## Chapter 1

Figure 1	Parts of the stomach.	23
Figure 2	Gastric tissue diagnosed with intestinal metaplasia observed under a) white light and b) NBI.	28

## Chapter 2

Figure 3	Multispectral cube from the antrum, where each pixel includes the full spectrum.	34
Figure 4	Principal phenomena involved in light tissue interaction.	38
Figure 5	Individual contributions of the optical properties in the shape of the reflectance spectrum. a) varying the scattering power. b) variation of blood concentration. c) Modifications due to oxygen saturation and d) Changes due to water content.	41
Figure 6	Possible results from a statistical test, where a small p value is evidence of rejection of the null hypothesis [75].	42
Figure 7	Hyperplane which defines the decision boundaries between two groups in a SVM classifier.	50

## Chapter 3

Figure 8	Acquisition campaigns and mice infected with <i>H. pylori</i> strain SS1.	58
Figure 9	Stomach from a mouse, with a chess pattern of 2 mm side of the square for reference.	58
Figure 10	Histological analysis of gastric mucosa magnified 10x, a) non infected mice and b) mice infected with <i>H. pylori</i> SS1 and sacrificed after 12 months post inoculation, which displays granulation tissue associated with inflammatory infiltrates.	59
Figure 11	Acquisition systems a) spectrometer Konica Minolta CM-2600d and b) multispectral camera Flux Data FD1665.	59
Figure 12	Point measurement of reflectance by the spectrometer at 4 random locations.	60

Figure 13	Normalized sensibility of each channel of the multispectral camera Flux Data FD1665.	61
Figure 14	Set up for the acquisition for the multispectral acquisition of ex vivo samples from mice stomach a) front view and b) isometric view.	61
Figure 15	Segmentation of the stomach from mice. a) Original image b) monoband image centered at 520 nm c) result from a sobel filter d) opening on the image, e) threshold and inversion, f) entropy filter and identification of the centroid of the stomach, g) estimated mask of the stomach and h) segmented stomach.	63
Figure 16	Colonization of the bacterium <i>H. pylori</i> in the stomach of mice, sacrificed in each acquisition campaign.	65
Figure 17	Box plots from the samples of the control group at a) 1 month, b) 3 months, c) 7 months and d) 12 months after inoculation.	67
Figure 18	Box plot from the samples from the control group acquired with the multispectral camera.	68
Figure 19	Normalized data from the spectrometer at each acquisition campaign. The statistical significant wavelengths retrieved from Wilcoxon-Mann-Whitney analysis are highlighted.	68
Figure 20	Normalized data from the multispectral camera and the results from the statistical analysis.	69

## Chapter 4

Figure 21	Block diagram of the first acquisition prototype based on a filter wheel.	74
Figure 22	Images acquired from gastric tissue at different wavebands from the prototype based on a filter wheel.	74
Figure 23	Simulation of white light image calculated from a) overlapping the raw monoband images and b) registered monoband image.	76
Figure 24	a) Registered image and b) selected region of interest from the image.	76
Figure 25	Images under white light from control group (a) and gastritis (b). In the band at 560 nm, we observe that the tissue from the control group (c) is smooth, in comparison with the gastritis one (d) which presents black spots and a non-uniform surface. We observe that the band at 560 nm highlights areas with a wooly dark weft appearance on the patients with active inflammation as is presented in figure (d).	79
Figure 26	Distribution of samples with a healthy diagnosis.	80
Figure 27	Ratio of variation in the spectrum from patients with active inflammation compared with the reference spectrum from control group.	80

## Chapter 5

Figure 28	Box plot of samples from the control group having a healthy profile.	85
Figure 29	Ratio of variation in the spectrum from patients with precancerous lesions compared with the spectrum from the control group.	86
Figure 30	Measurement of the discriminative potential of the ranked features from table 12 by using pooled variance t test.	89
Figure 31	Quantitative evaluation of the classifiers with different number of features, increased progressively by order of rank, a) accuracy, b) sensitivity and c) specificity.	90
Figure 32	Elements of the system GEMS.	92
Figure 33	Gastroendoscopic unit. The gastroendoscope has two connections, one to the video unit and the other to the source of light.	93
Figure 34	Elements at the tip of the gastroendoscope and the microendoscope in the operational channel.	94
Figure 35	Spectrum from the light source of the a) Gastroendoscopic unit, which does not provide illumination above 700 nm and b) Xenon lamp from the system GEMS which includes the NIR.	95
Figure 36	Distribution of light when using only the source of light from the gastroendoscope. The distances D1 (gastroendoscope to tissue), D2 (gastroendoscope to microendoscope) and D3 (microendoscope to the tissue) are not assured to be constant.	95
Figure 37	Acquisition of a chess pattern illuminated with the gastroendoscope. a) image from the gastroendoscope and b) image from the microendoscope in the first channel of the multispectral camera, which is considerably dark.	96
Figure 38	Illumination using the gastroendoscope and GEMS, the captured light (bold red arrows) is mainly the contribution from the microendoscope (dotted red arrows) and in lower amount the light from the gastroendoscope (thin red arrows).	96
Figure 39	Acquisition of a chess pattern illuminated with the source of light from the microendoscope. a) image from the gastroendoscope and b) image from the microendoscope.	97
Figure 40	Optical design to transfer the image from the microendoscope to the sensor of the camera Flux Data.	98
Figure 41	Mechanical components of the optical relay block.	99
Figure 42	Image from the microendoscope a) In focus where the Moiré pattern is clearly observed, b) Image out of focus to be slightly blurred in order to avoid the Moiré pattern.	100

Figure 43	Graphical user interface for the system GEMS. On the left is the image from the gastroendoscope where the microendoscope is observed. On the right is the image collected by the microendoscope.	101
Figure 42	Image from the microendoscope a) In focus where the Moiré pattern is clearly observed, b) Image out of focus to be slightly blurred in order to avoid the Moiré pattern.	100
Figure 44	Active area of the microendoscope, identified with circular Hough transform.	102
Figure 45	a) Simulation of white light image from the multispectral image where we observe the antrum (left) and specular reflections (top and right). b) Manually selection of the region of interest.	102
Figure 46	Distribution of samples from the control group.	104
Figure 47	Ratio of variation in the spectrum from patients with precancerous lesions compared with the spectrum from the control group.	105
Figure 48	Measurement of the discriminative potential of the ranked features from table 17 by pooled variance t test.	108
Figure 49	Quantitative evaluation of the classifiers with different number of features, increased progressively by order of rank, a) accuracy, b) sensitivity and c) specificity.	109

# List of tables

## Chapter 1

Table 1	Evolution of the gastritis associated with <i>H. pylori</i> into precancerous lesions and their reversibility.	26
---------	----------------------------------------------------------------------------------------------------------------	----

## Chapter 2

Table 2	Spectrum of light [57].	37
Table 3	Example of features.	47
Table 4	Confusion matrix of possible outcomes from the classification.	52

## Chapter 3

Table 5	Evolution of the inflammation of the gastric mucosa after infection by <i>H. pylori</i> .	65
Table 6	Band of wavelengths which are candidates for diagnosis of the gastritis.	70
Table 7	Wavebands with significant differences between acquisition campaigns from the normalized inoculated data.	71

## Chapter 4

Table 8	Clinical features from the patients.	77
Table 9	Multispectral images from the two clinical groups.	78

## Chapter 5

Table 10	Clinical features from the patients.	84
Table 11	Multispectral images from the two clinical groups.	85
Table 12	Ordered list of features.	88
Table 13	Best performance of the classifiers.	91
Table 14	List of elements of the optical relay block.	98
Table 15	Clinical features from the patients.	103
Table 16	Mean number of multispectral images for the two clinical groups.	104



# List of abbreviations and symbols

[ W ]	Expression for units, in this case, Watts
$\alpha$	Mean of the samples
$\alpha_i$	Mean of the samples from the $i^{th}$ group
$\beta$	Unit vector from the hyperplane for the SVM classifier
$\beta_0$	Constant from the hyperplane defined in SVM classifier
$\varepsilon$	Normal random error
$\lambda$	Wavelength
$\mu$	Mean
$\mu_a$	Absorption coefficient [ $cm^{-1}$ ]
$\mu_s'$	Reduced scattering coefficient [ $cm^{-1}$ ]
$\sigma$	Variance
$\vartheta$	Shift in the distribution
$a'$	Transport albedo
$A$	Internal reflection
$C$	Number of classes
$D_{jl}$	Indicator used in Mann Whitney - Wilcoxon test
$E(\lambda)$	Irradiance [ $Wm^{-2}$ ]
$E_{black}(\lambda)$	Irradiance from a black patch, used as a black reference
$E_{white}(\lambda)$	Irradiance from a white patch, used as a white reference
$F_{val}$	Result from the statistical test under a F distribution
$f$	Sigmoidal function
$f_1$	Feature
$G$	Space of the classes
$G(x)$	Distribution function of the samples from the population $x$
$H$	Result from the statistical test under a $\chi^2$ distribution
$H_0$	Alternative hypothesis
$J$	Space of the samples
$k$	Total of groups. In classification with k nearest neighbor is the number of neighbors
MAD	Median of absolute deviation
$N$	Total of samples
NA	Numerical aperture
$N_k(x)$	Neighborhood of $k$ samples from $x$
NS	Not significant
$n_i$	Total of samples from the $i^{th}$ group
$n_{rel}$	Refractive index mismatch between air and tissue surface of tissue



$n_t$	Refractive index from the surface of tissue
$n_v$	Refractive index from the air
$Pr$	Conditional probability
$q$	Total of wavelengths in the spectrum
$R_i$	Summation of ranks in the $i^{th}$ group
$R_T$	Decision rule
SEM	Standard error of the mean
$T$	Vector of features
$U$	Indicator of the Mann whitney U statistics, from the mann whitney - wilcoxon test
$W$	Parameter computed in Mann Whitney Wilcoxon non-parametric test
$x$	Training samples
$x$	Group of samples and it can also be used to represent the spectrum
$x_j$	$j^{th}$ sample from the group $x$ . The $j^{th}$ wavelength from the spectrum
$x_j^q$	The $q^{th}$ element from the $j^{th}$ sample from $x$
$Y_j$	Class of the $j^{th}$ sample
$\hat{Y}_j$	Assigned class of the $j^{th}$ sample
$y_{ij}$	$j^{th}$ sample from the $i^{th}$ group
$z$	Normalized spectrum
$\bar{z}$	Mean of the normalized spectrum
$Z_{val}$	Result from the statistical test under a Z distribution

# Preface

This thesis was prepared at the laboratory Le2i from the University of Burgundy in Dijon, the laboratory Charles Fabry of the Institut d'Optique Graduate School and the University of Versailles Saint Quentin en Yvelines, University Paris Saclay. The project started in October 2012 and was completed in September 2015. Throughout this period, the project was supervised by Prof. Dominique Lamarque (UVSQ), Prof. Francois Goudail (IOGS) and Prof. Franck Marzani (le2i, UB).

## Publication note

Parts of the presented work have previously been published in journals and at conference proceedings. Following are the paper contributions from the research work on the subject.

### *Journal*

[1] Identification of precancerous lesions by multispectral gastroendoscopy S. E. Martinez-Herrera, Y. Benezeth, M. Boffety, J.-F. Emile, F. Marzani, D. Lamarque et F. Goudail *Signal, Image and Video Processing*, Springer London, 2015, pp. 1-8.

### *International conferences*

[2] Multispectral Endoscopy to Identify Precancerous Lesions in Gastric Mucosa S. E. Martinez-Herrera, Y. Benezeth, M. Boffety, J.-F. Emile, F. Marzani, D. Lamarque, and F. Goudail In *Image and Signal Processing*, vol. 8509, A. Elmoataz, O. Lezoray, F. Nouboud, and D. Mamass, Eds. Springer International Publishing, 2014, pp. 43–51.

[3] Development of a multispectral endoscope to improve the detection of precancerous lesions in digestive gastroendoscopy S. E. Martinez-Herrera, Y. Benezeth, M. Boffety, F. Goudail, D. Lamarque, J.-F. Emile, F. Marzani, *Doctoral Consortium of the Int. Conf. on Computer Vision, Imaging and Computer Graphics Theory and Application (VISIGRAPP)*, 2014.

### *Medical conferences*

[4] L'analyse spectrale de la lumière réfléchie permet de différencier les différentes étapes des lésions inflammatoires de la muqueuse gastrique dans un modèle expérimental d'infection à *Helicobacter pylori* chez la souris S.E. Martinez-Herrera, E. Touati, Y. Benezeth,

M. Boffety, V. Michel, L. Fiette, J.-F. Emile, F. Marzani, F. Goudail, D. Lamarque Journées Francophones d'Hépatogastroentérologie et d'Oncologie Digestive, Paris, 2015

[5] Intérêt de l'analyse multispectrale des images endoscopiques de la muqueuse gastrique pour reconnaître la gastrite inflammatoire et ses différents types : résultats d'une étude préliminaire S.E. Martinez-Herrera, R. Akka, Y. Benezeth, M. Boffety, F. Goudail, J.-F. Emile, F. Marzani, D. Lamarque Journées Francophones d'Hépatogastroentérologie et d'Oncologie Digestive, Paris, 2014

# Introduction

The last decades have shown the improvements on computing and imaging, leading to significant advances in medical research. They are used as a supplementary tool in the identification of malignancies, in view of providing the most adequate treatments for the patients. These tools are particularly relevant in the identification of malignancies which are developed without symptoms or poorly identified, opening an important area of new contributions.

The worldwide estimation of gastric cancer in 2012 was 951 594 cases (6.8 % of all cancers) and a mortality of 723 027 (8.8 % of total death tolls due to cancer) which makes it one of the top 5 deadly cancers [1]. The risk to develop this malignancy depends on different factors, for instance infection with *H. pylori* and environmental conditions including hygienic, alimentation, smoking, high salty diet and genetic predisposition [2] [3].

The development of cancer follows a cascade of well-defined stages which most of the time are asymptomatic. Under these circumstances, the accurate diagnosis of these early stages is highly valuable since it allows low aggressive treatments. Unfortunately, most of the time, there are no macroscopic differences between healthy and malignant tissue. Therefore, in order to provide a diagnosis, practitioners require evaluating the symptoms and the risk factors of the patient. Then, according to this information, they can decide if further studies are required.

Nowadays, the diagnosis of gastric pathologies is divided in two procedures. The first one is gastroendoscopy which is the visual exploration of the stomach under white light. The second one is the collection of biopsies for histological analysis. This procedure has a high probability of establishing the correct diagnosis but the collection of biopsies requires a significant amount of time, demands extra resources from the gastroenterology and histopathology departments [4] and it strongly depends on the accurate collection of samples from damaged tissues. Therefore, it is clear that additional sources of information are required in order to help on targeting the biopsies.

The identification of precancerous lesions during gastroendoscopy is a challenge for practitioners and also for computer-assisted diagnosis systems (CAD) because the lesions are multifocalized and present low macroscopic differences with respect to healthy tissue [5][6]. Every disease requires its own unique procedure, in order to identify it. The time available for gastroendoscopy is limited, taking into consideration that it includes

preparation of the patient, navigation in the stomach, collection of biopsies and if necessary, start a medical treatment. As a result, the exploration time could be reduced to 5 minutes. In this small amount of time, it has been shown that lesions could be lost, and there is always the risk for a complication. Under these circumstances, it is clear that immediate feedback about the status of the mucosa could help on providing a faster diagnosis, allowing more time for treatment instead of tissue exploration.

There are multiple strategies proposed in order to improve the diagnosis. They include label by dyes such as chromoendoscopy, chemicals for fluorescence and markers for new techniques in molecular imaging. Besides these approaches, we can consider those where no substance is used, for instance techniques based on vibration signatures of tissue in the case of Raman and light tissue interaction such as autofluorescence, light scattering, spectroscopy and multispectral imaging. The principle that the interaction between the light and the tissue is related to the physical properties of the tissue is a well-known fact [7]. In particular, changes in the gastric tissue during the development of malignancies include chemical structure and architectural modifications, so that histopathological tissues may reflect light with different spectrum from those with normal mucosa. This property allows us to access absorption, scattering coefficients and blood content, which encode information that could help in the diagnosis of precancerous lesions. In this sense, we use multispectral imaging to analyze spectral and spatially the surface of the mucosa.

Our vision is that the techniques of light tissue interaction will provide a practical and accurate tool to be used in a daily basis during medical procedures, oriented to “see and treat concept”. In a first stage, it could provide relative information to improve the detection of gastric lesions at an early stage. Then, it can also be extended to evaluate the performance of medical treatments and the response of tissues to new medicines. Additionally, the development of more accurate models of light tissue interaction, similar to those that have been developed for skin, will provide more details of the characteristics and elements of the tissue, which could be used as features to improve the diagnosis and also to reduce the interobservability presented in gastroendoscopic and histological images. These efforts could lead to an increment of survival rate from the patients and most important, their quality life.

This project focuses on the study of gastric mucosa by multispectral imaging to improve the diagnosis of malignancies in the stomach. Thanks to the new advances in technology we can capture multispectral images from gastric tissue during gastroendoscopy. The main contribution is the clinical study of multispectral imaging to differentiate pathologies poorly diagnosed or that can only be diagnosed by histological analysis. For this purpose, we performed ex vivo studies in a mice model under controlled conditions and we present two prototypes developed to acquire multispectral images from gastric tissue. Additionally, we present a first group of algorithms to estimate and differentiate between normal and pathological tissues based on statistics and machine learning techniques.

The content of this thesis is organized in the following way:

**Chapter 1** gives a review of the development of gastric cancer, focusing on the different stages. It is also presented a review of the techniques and technology used for diagnosis. A discussion about the advantages and limitations of these technologies is included. The chapter concludes with an evaluation of these technologies and their applications in clinical studies.

**Chapter 2** is dedicated to the principles of spectroscopy and multispectral imaging, including the light tissue interaction, the measurement of the light spectrum, the statistical analysis, the extraction of features and an overview of the data mining techniques used to differentiate malignant tissues.

**Chapter 3** describes the development of precancerous lesions under controlled conditions; we explain the mice model and discuss the results obtained from the analysis of ex vivo tissues.

**Chapter 4** is oriented to a clinical study of the gastritis. We describe a multispectral acquisition system based on a filter wheel to collect the spectra and we discuss the results from the statistical analysis.

**Chapter 5** explains the performed clinical studies in order to evaluate the differentiation of malignancies. We describe the data acquired with the prototype based on a filter wheel and a second prototype developed based on the learned lesions from the previous one. We describe the machine learning techniques used to differentiate the malignancies. We discuss the results obtained and finally, we conclude.

Finally, a conclusion summarizes the work and presents the future directions.



# Chapter 1

## Review on gastritis, precancerous lesions and their diagnosis

The subject of this chapter is the gastritis due to infection by *H. pylori*, its evolution into precancerous lesions and different approaches for its diagnosis. We introduce the anatomy of the stomach and how the gastritis, as well as the others precancerous lesions develop. Their diagnosis is difficult since one has to detect subtle variations in the mucosa. In order to diagnose these stages, a number of different techniques are currently used in medicine. These technologies will be discussed in this chapter and we will focus on their clinical importance.

### 1.1. Anatomy of the stomach

The stomach can be divided in 3 regions based on the histological differences present in the mucosa. In figure 1 are presented these regions: fundus, body and antrum. It has been reported that some areas of the stomach are more susceptible to develop pathologies. 35% are present in the fundus, 25% in the body and finally the antrum with 40% [8]. This difference in the areas of development could be the result of the permanence of gastric juice in the stomach.

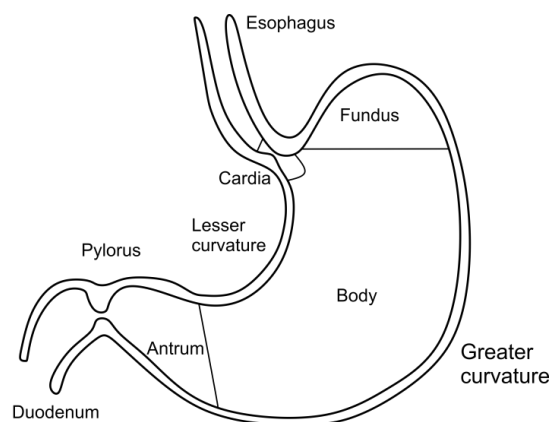


Figure 1. Parts of the stomach.



Considering that the area of tissue from the antrum is small and has high probability of develop malignancies, we will focus this study on this area.

The epithelium of the mucosa in a normal state includes glandules and other specialized structures for the digestion such as parietal cells (producer of acid HCl), endocrine cells (regulator of parietal cells) and chief cells (producer of pepsinogens, which in conjunction with the HCl convert proteins into amino acids). These structures are altered during the evolution of the gastritis, as it will be described in the following subsections.

## **1.2. Evolution of gastritis**

During the development of pathologies, the structures in the epithelium could change their organization or even be replaced by others. Multiple studies have shown the cascade of well-defined stages [9]. In the following subsections are described the modifications observed in the epithelium during the progression of the disease.

### **1.2.1. Chronic active gastritis, infection by *Helicobacter pylori***

Gastritis is defined as the inflammation of the gastric mucosa. The diagnosis is performed by histological analysis of biopsies collected during gastroendoscopy. This inflammation displays a diffuse distribution in the stomach that is mainly characterized from the histopathological point of view as an accumulation of infiltrating leukocytes, such as polymorphonuclear neutrophils, mononuclear cells and also by the presence of follicular lymphocytes [10][11]. At this stage, the risk of cancer is low.

This inflammation is typically the result of a chronic infection by *Helicobacter pylori*, which could last for life if it is not treated. This responsible bacterium sizes between 2 and 4  $\mu\text{m}$  by 0.5 to 1  $\mu\text{m}$ . It has 2 to 6 unipolar flagella for motion and is adapted to the harsh environment of the stomach. It creates an alkaline microenvironment by converting urea into ammonia and carbamate [12][6].

This bacterium colonizes preferentially the area of the antrum. In order to diagnose the infection there are 2 main approaches: invasive and non-invasive methods. The invasive methods include biopsy for histology analysis, culture and serology. The non-invasive methods are blood, urine, saliva and breathe tests. It is important to highlight that during gastroendoscopy the infection cannot be diagnosed with traditional approaches [13], since there are no significant macroscopic changes.

The biological mechanisms of defense of the body to this bacterium are still a mystery. However, as this bacterium remains on the surface, the defense of the body results in

epithelial cell damage through malignant tissue due to a combination of inflammatory and anti-inflammatory responses [14].

Though this bacterium is considered as a carcinogen by the World Health Organization since 1994 [15], its true risk factor is still in discussion, since only some patients develop advanced stages of the diseases and gastrointestinal complications.

### **1.2.2. Atrophy**

The atrophy is considered as a precancerous lesion [16][17]. Even though its origin is from active gastritis, it shows multifocalized diffusion in the stomach. The diagnosis is performed by histological analysis of biopsies collected from gastroendoscopy because the changes are currently observed microscopically. This pathology is discovered when the native glands from the gastric mucosa shrink or disappear. These glands are typically parietal cells oriented to produce acid (HCl) whose disappearance produces hypoacidity [12] [60]. The remaining space from the glands is taken by fibrous tissue and infiltrates of leukocytes, allowing the submucosal vessels of the gastric mucosa sometimes to be more visible but this feature is reported to have a low sensitivity [18].

### **1.2.3. Intestinal metaplasia**

Intestinal metaplasia is a well-known precancerous condition, which is characterized by the replacement of the gastric glands by intestinal type glands [9][17]. Similar to the previous stages, the diagnosis is performed by histological analysis of biopsies collected during gastroendoscopy. This stage has a significant risk of developing cancer.

The development of this pathology shows at first stage enterocytes (intestinal absorptive cells), goblet cells (producer of mucin) and Paneth cells (protection of stem cells to renovate the epithelium), which are typically observed in the intestine. This stage is defined as complete type. On the other hand, the incomplete type is diagnosed when all the cells contain mucin [19] [20]. The complete type could evolve into an incomplete type and potentially into a more dangerous stage. These modifications show changes in the relief of the surface of the mucosa.

Histologically, it is discovered by staining with hematoxylin and eosin (H&E): the first one is for cell nuclei, the second one for cytoplasm [21][5].

### **1.2.4. Dysplasia**

Dysplastic lesions have more often their origin in tissue with intestinal metaplasia. At this stage the gastric mucosa presents muddle mucosal architecture and loss of native glands.

One observes mitotic activity in the gastric cells, as well as major changes in their shape and organization due to loss of nuclear polarity, cell enlargement and nucleus over pigmentation [9][22][23]. This is considered as the last stage before the evolution into a cancerous lesion [24][25].

It can be diagnosed as low grade or high grade dysplasia, depending on morphological changes such as epithelial atypia and architecture of the mucosa [26]. At this stage there is a controversy between western and Japanese diagnosis since high grade dysplasia is diagnosed as cancerous by Japanese physicians. Since there are strong relationships between a dysplastic lesion and cancerous lesion, the main difference is related to the histological evidence of infiltrations in the stroma.

### 1.2.5. Cancer Lesion

This is the last stage of the evolution, where the disease invades deeper tissue layers and there is high risk that the cancerous cells could be spread in the body. The morphological changes include an increase in the thickness of the mucosal layer, reduction of collagen and the development of a dense irregular vessel network [27][24]. At this stage, the 5 year survival rate is low, the patients most of the time follow strong treatments with chemotherapy, removal of the stomach surgically and palate treatments [28].

The affected population shows a median age for diagnosis of early gastric carcinomas at 63 years old, showing that men are more affected than women with a ratio of 1.4 – 2.4:1 [3].

It is known that the best prognosis is achieved for patients whose precancerous lesions are identified at an early stage, as mentioned in table 1. Under these circumstances, the main advantage for the patient is the high reversibility of the disease, the survival rate, low cost and low impact of the treatments, which finally leads to a fast recovery and returns to his normal daily life.

Table 1. Evolution of the gastritis associated with *H. pylori* into precancerous lesions and their reversibility.

Stage	Reversibility
Normal mucosa	--
Chronic active gastritis	100%
Atrophy	50 %
Intestinal metaplasia	20 %
Dysplasia	8 %
Cancer	1 %

The diagnosis at an early stage is a well-known challenging task because most of the stages of the disease fail to develop symptoms, making them a silent disease which is typically discovered at advanced stage.

In order to understand this pathology, malignancies in the stomach have been a research subject for a long time, mainly oriented to identify the biological mechanism involved. Different approaches have been proposed and are currently used in a daily basis for diagnosis, which will be discussed in the following subsection.

### **1.3. Gastroendoscopy and biopsy collection techniques for diagnosis.**

In the previous paragraphs were described the modifications in the tissue, which are presented at microscopical level. As the diagnosis depends on the correct collection of biopsies, multiple techniques have been proposed in order to predict the histology during gastroendoscopy.

Gastroendoscopy and biopsy collection is currently the gold standard medical procedure to diagnose pathologies in the stomach. It follows two stages: visual exploration of the stomach (gastroendoscopy, typically under white light) and collection of biopsies. The area of the stomach to sample strongly depends on the endoscopist. Studies have shown that gastritis is inconstantly diagnosed. In fact, 50% of patients with intestinal metaplasia are being missed in current routine gastroenterology practice [29][30]. The reason why gastritis cannot be identified during gastroendoscopy is because the gastric mucosa shows poor correlation with the histological diagnosis.

In case of other pathologies such as intestinal metaplasia, the traditional features for identification are related to subtle mucosal alterations, discoloration (pale gray or reddish discoloration), nodular or depressed mucosa, ulcerations, disorganization of the vascular pattern and capillaries organized as a honeycomb pattern [31][32] as presented in figure 2a. It is important to highlight that all these changes are strongly subjective.

In order to diagnose gastritis and preneoplastic lesions, there are two main approaches used. The first one is the collection of multiple biopsies, randomly in the antrum and corpus. The second one is oriented biopsies, from mucosal changes seen by computed virtual chromoendoscopy.

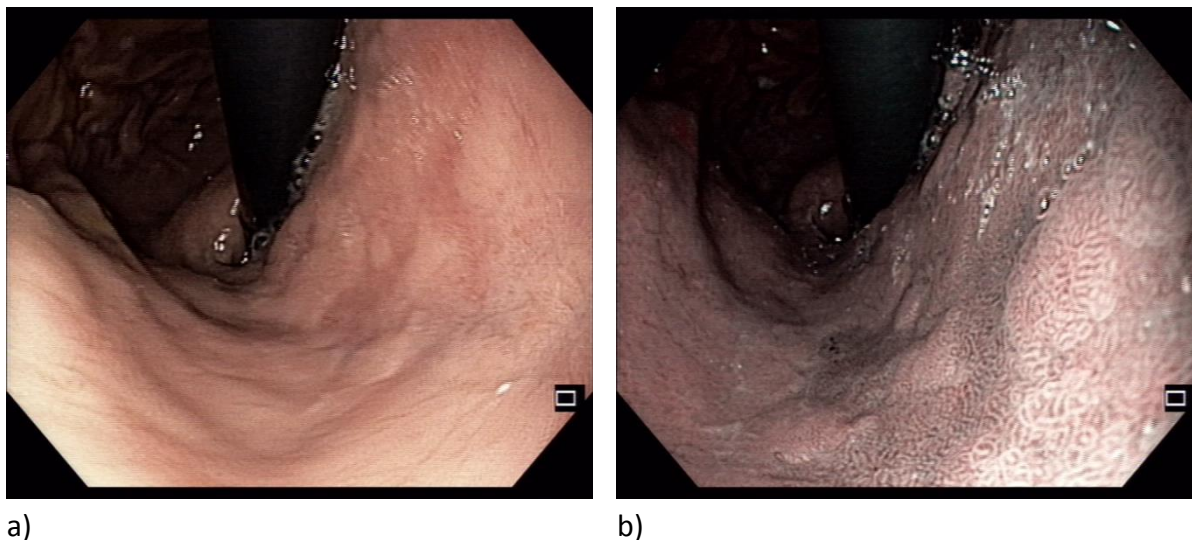


Figure 2. Gastric tissue diagnosed with intestinal metaplasia observed under a) white light and b) NBI.

### **1.3.1. Random collection of multiple biopsies from antrum and corpus**

Histologic examination of 4-5 biopsies taken at random remains in practice the most widely used approach for dysplasia recognition according to the Sydney protocol [33] [34]. Following the current European recommendations for monitoring of patients with severe or extensive intestinal metaplasia [35][36][37], such lesions should be monitored every 3 years by endoscopy with mucosal biopsies. In practice, four to five non-targeted biopsies of two topographic sites in antrum and corpus are recommended [35].

This approach has the disadvantage that multiple biopsies are required in order to assess the right diagnosis; it presents interobserver variations and requires time and resources from different departments. Taking in consideration these disadvantages, we consider that the target biopsies oriented to suspicious areas of gastric tissue identified automatically could improve the sensibility of the diagnosis.

In the following subsections we will focus on the current techniques available in medical practice for the identification of suspicious tissues.

### **1.3.2. Oriented biopsies on mucosal changes**

#### **1.3.2.1. Narrow Band Imaging (NBI)**

The NBI is a commercially available technology proposed by Olympus Medical Co., Tokyo, Japan, which is oriented to provide a false color image that produces high contrast

between vascular network and the surrounding mucosa [38][39][40]. This technique also known as virtual chromoendoscopy is promising in the detection of intestinal metaplasia.

The configuration is nowadays based on two filters (415 and 540 nm), which correspond to the main peaks of absorption from hemoglobin. The false color image is created by placing the monoband image of 540 nm in the red channel. Then, the monoband image of 415 nm is duplicated in the green and blue channels [41].

As a result of this configuration, the blood vessels are observed in dark colors due to the absorption property of the blood. The band of 415 nm is oriented to observe the abnormalities of the surface of the mucosa, displaying the superficial capillaries in brown. In contrast, the deeper vessels are visible in cyan [38].

The examination of the gastric mucosa with NBI is oriented to identify abnormalities at the surface of the mucosa and blood vessels abnormalities from the vascular network, highlighting the pattern associated with intestinal metaplasia, observed with light blue crest, irregularities, white opaque substances and tubule-villous aspects [42]. As an example, intestinal metaplasia is displayed in figure 2b.

Similar to other techniques, NBI requires a training period and presents observer variation.

### **1.3.2.2. Flexible Spectral Imaging Color Enhancement (FICE)**

FICE is a commercial equipment from Fujifilm Medical Co., Tokyo, Japan, which is oriented to enhance the visual information of mucosal structures, by estimating the spectral transmission from RGB images.

Images at a single wavelength or monoband are algorithmically estimated between 400 and 695 nm each 5 nm. It displays false color images based on the combination of the estimated monoband images. It includes 10 preconfigured setups oriented to enhance the characteristics of the mucosa. In general it uses a combination of the bands at 470 nm, 500 nm and 550 nm to observe depressed, flat and elevated gastric lesions [43]. Additionally, the user can select its own configuration of monoband images.

LASEREO system is a recent improvement of the FICE system that includes two lasers, one at 410 nm  $\pm$  10 nm and the other at 450 nm  $\pm$  10 nm. The first one is used to obtain the blood vessels and superficial mucosal structures. The second one displays deep blood vessels. Additionally, it also excites phosphors to create white light illumination. This technology has interobserver variations and requires a training period.

### 1.3.2.3. i-scan

The equipment i-scan from Pentax, Tokyo, Japan applies post-processing algorithms to the images acquired under white light. The treatment is mainly oriented to image enhancement, including edge detection to improve the appearance of mucosal structures. It allows the differentiation between structures and depression areas by improving the visualization of low-density areas. Additionally, it includes a tone enhancement depending on the observed tissue such as esophagus, stomach and colon.

Similar to other techniques displaying false color images, these technologies require a training period and present low interobserver agreement.

Up to our knowledge, there are no publications evaluating the role of FICE, lasereo nor i-scan in the diagnosis of the gastritis [44][43]. Even with NBI which has been the more studied, the gastritis remains not detectable with these different techniques.

### 1.3.2.4. Chromoendoscopy

Chromoendoscopy is based on the use of a dye in order to highlight specific features from the tissue. It is considered as a fast, inexpensive and safe technique used to improve the visualization of the gastrointestinal mucosa. The dye used on the tissue can be classified in three types depending on their function [39].

- *Vital stain* which are absorbed by the cells. Oriented to highlight the "mosaic" pattern. An example is methylene blue at 0.5% dilution, with which the normal mucosa is stain into dark-blue color; stainless tissue is related to the presence of metaplastic changes [45][46][47].
- *Contrast stain* as indigo carmine between 0.1 and 0.4% dilution. It highlights the relief from the mucosa accumulated in pitch and valleys of the tissue [48][41].
- *Reactive stain* is oriented to modify its color due to the presence of a chemical process [45]. An example is congo red at 0.5% dilution as a pH indicator, which changes from red at a pH of 5 to dark blue-black at a pH under 3. Therefore, it is used to detect acid-secreting gastric cells. Other example is phenol red at 0.1% dilution, used to identify *H. pylori* infection by staining tissue from yellow to red.

The main advantage is that specific features can be highlighted from the tissue using this technique. However, there are some drawbacks, for instance the specialized equipment required to perform this procedure, the low interobserver agreement and the training period required in order to achieve a uniform coating of the mucosa.

In the stomach, the dyes most commonly used for advanced lesions are indigo carmine and methylene blue. However, the interest is low because the subtle changes in the mucosa are difficult to be colored, specifically at an inflammatory stage such as gastritis. Under these circumstances, there is no study for the identification of gastritis using this technique.

## **1.4. Summary**

The evolution of the gastritis into precancerous lesions follows a cascade of multiple stages. The modifications of the pathological tissues are presented at microscopic level, producing low variations with respect to normal mucosa. In order to diagnose them, different approaches have been proposed to identify these changes macroscopically. Nowadays, the gold standard is the visual exploration of the mucosa and the collection of biopsies for histological analysis. This approach has high probability of establishing the correct diagnosis but it depends on sampling the pathological tissue.

The modifications of the tissue from a macroscopical point of view display low correlation with respect to the histological results. Even though some features could be identified, they remain strongly subjective. In fact, up to now, there is no available technology which recognizes satisfactorily without biopsy the inflammation stages at a macroscopic level, such as inflammatory gastritis or intestinal metaplasia.

Current technologies used for diagnosis rely on imaging light tissue interaction, typically under white light or on collecting partial spectral information. The objective of this doctoral work is to acquire the full reflectance spectrum from gastric tissue in order to perform classification for diagnosis.





## Chapter 2

# Acquisition and processing of the reflectance spectrum

The subject of this chapter deals with the reflectance spectrum, oriented to explain how spectroscopy and multispectral imaging are used to acquire the reflectance spectrum and particularly on how to extract information from it. In this sense, we focus on model fitting, statistical analysis and machine learning techniques. As a support, we apply a model of light tissue interaction based on diffusion theory to show the variations in the spectrum from the biological parameters of gastric tissues, demonstrating that the reflectance spectrum encodes biological characteristics of the tissues.

Generally speaking, the interpretation of the spectrum is not an evident task. For instance, two different spectrums after being partially sampled by our eyes could be perceived with the same color by our brain. This well-known phenomenon is named metamerism, which in gastric tissues produces normal and pathological tissues being perceived with the same color. This situation makes difficult to identify the pathological tissues during gastroendoscopy [56]. Therefore, there is a strong interest on the analysis of the information encoded in the reflectance in order to help the human eye to distinguish the changes in the tissues and their relation with histology. With this aim, we include the statistical analysis in order to identify differences between normal and pathological tissues and a methodology based on spectrum preprocessing, feature extraction, feature selection and finally, machine learning techniques for classification.

### 2.1. Principles of Spectroscopy and Multispectral imaging

Multispectral imaging and spectroscopy are oriented to measure the spectral reflectance of an object at different wavelengths. Historically, spectrometry has been widely used for more than half a century in mineralogy to identify specific chemical signatures [49]. This technology has been also exploited in the identification of some specific biological reactions and also to study the surface of the earth, military purposes and recently as a tool for diagnosis in medicine [50] [51].

The main characteristic to differentiate spectroscopy and multispectral imaging is with respect to the spatial dimensions acquired. In this sense, spectroscopy acquires one dimension (point measurement) and multispectral imaging acquires two spatial dimensions as an image. Since spectroscopy is oriented to acquire only one dimension, it is used for a single point acquisition from the surface, providing high spectral resolution (sometimes more than the nanometric precision). This characteristic makes it non-suitable for mapping the observed scene (such as the stomach), or it will require long time to scan a whole region of the sample [52]. In the case of multispectral imaging, the three dimensions acquired are two spatial dimensions for the image and one spectral dimension for the wavelength [53]. The images captured at each wavelength are named monoband images. When all the images are stacked according to their wavelength, a multispectral cube is obtained, as shown in figure 3. In this case, each pixel of the 2D image could be considered as a point measurement or a single spectrum.

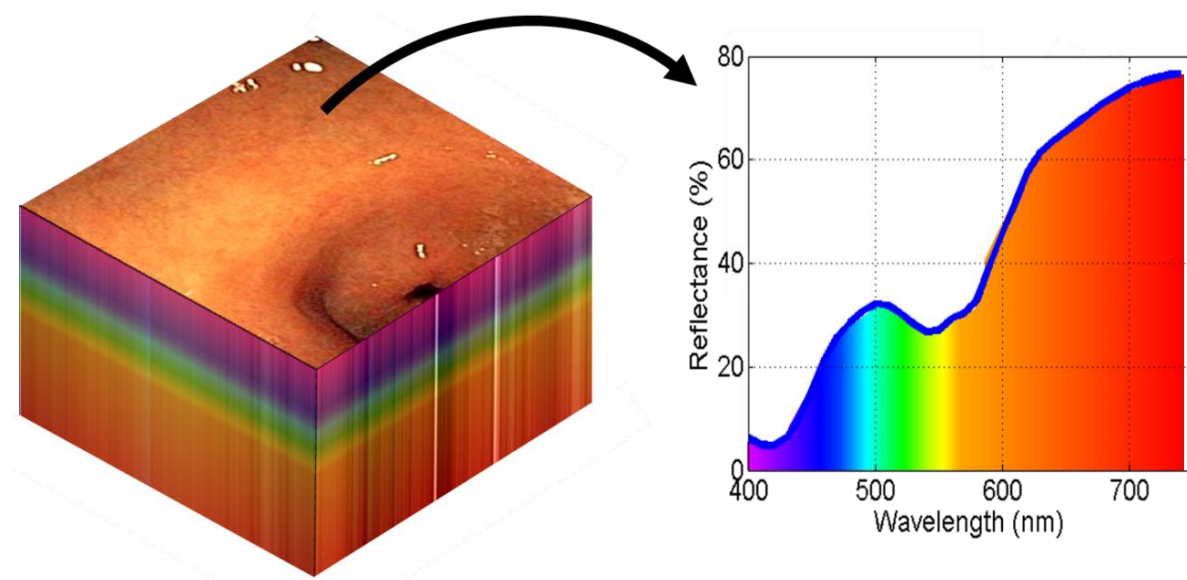


Figure 3. Multispectral cube from the antrum, where each pixel includes the full spectrum.

Due to the multiple wavelength nature of multispectral images, three main challenges are identified. The first one is the required memory space to store the 3 dimensions (width, height and wavelength) from the multispectral image. The second one is that the high amount of data from a single multispectral image is preferable to be acquired in a single shot and stored as fast as possible in memory. The third one is due to the treatment and analysis of big data quantities [54]. With this in mind, we start with the acquisition of the spectrum.

## 2.2. Acquisition of reflectance spectra $R(\lambda)$

This subsection deals with the different configurations to collect multispectral images, definition of the reflectance and calibration of the sensors.

### 2.2.1. Acquisition techniques

This measured reflectance is the principle of spectroscopy and multispectral imaging. Different options have been proposed to acquire multispectral images, they can be classified in 4 groups: whiskbroom, pushbroom, staring and snapshot [53][55].

- **Whiskbroom.** It is known as a point-scanning method, where the light is diffracted by a prism and acquired by a line array detector. The multispectral image is generated by moving the sample or the sensor in the two spatial dimensions. Commercial spectroscopic systems and confocal scanning instruments use this approach.
- **Pushbroom.** It is also mentioned as line scanning, where one spatial and the spectral dimension are acquired at a time, so that only a line of the image is generated. Then, a physical movement of the camera is required in order to capture the remaining spatial dimension [55]. This technique could be used in production lines with a conveyor belt.
- **Staring.** In this approach, successive images at different wavelengths are acquired in a short period of time. It could take advantage of a filter wheel with interference filters, electronically tunable filters or even acousto-optic tunable filters among others.
- **Snapshot.** It acquires the 3 dimensions at the same time. Nowadays we can find different examples of this approach, for instance the camera from Flux Data Inc, Rochester, USA, where the light is split into different sensors so that each of them can capture the full image at a specific wavelength. Other example is from the company IMEC international, Heverly, Belgium, where filters are included in the sensor; in this approach, a pixel from the multispectral image is acquired from a window of 4x4 (optional 5x5) pixels in the image, so that each pixel of this window acquires one wavelength, producing 20 monoband images (optional 25) in a single shot. The disadvantage is that the multispectral image has a smaller resolution.

Generally speaking the first three approaches produce motion artifacts since the scene cannot be assured static during the acquisition. With this in mind, registration is required between the monoband images in order to reduce the impact of tissue deformation and shifting in case of the stomach.

### 2.2.2. Reflectance and sensor calibration

In the formulation of the reflectance spectrum  $R(\lambda)$  from a surface element, let us consider the spectral irradiance from a source of light  $I(\lambda)$  in  $[W \cdot m^{-2}]$ . This light is partially back-scattered by the sample typically in all directions and is characterized by its spectral exitance  $E(\lambda)$  in  $[W \cdot m^{-2}]$  over  $2\pi$  steradians. Therefore, we can define the reflectance [56] at each wavelength as shown in equation 1.

$$R(\lambda) = \frac{E(\lambda)}{I(\lambda)} \quad \text{eq (1)}$$

It is important to highlight that the reflectance is dimensionless subject to  $R(\lambda) \leq 1$  (or 100%). The exitance  $E(\lambda)$  can be acquired by our eyes or a sensor but in general, we are interested in the reflectance  $R(\lambda)$  since it is related to the properties of the object and it is independent from the source of light.

The reflectance can be estimated from  $E(\lambda)$  by performing a spectral calibration, where  $I(\lambda)$  is measured through a ColorChecker® (X-Rite Inc, Grand Rapids, Michigan), Spectralon® (Labsphere Inc, North Sutton, New Hampshire) or Zenith Polymer® (SphereOptics GmbH, Germany) from which their reflectance is constant and known at near UV, visible and near infrared wavelengths. In this sense, the exitance is acquired from two calibrated references, which are a black patch at 2% to obtain  $E_{black}(\lambda)$  and a white patch at 99% to get  $E_{white}(\lambda)$ . The reflectance is retrieved by using equation 2.

$$R(\lambda) = \left( \frac{E(\lambda) - E_{black}(\lambda)}{E_{white}(\lambda) - E_{black}(\lambda)} \right) \left( \frac{99}{100} \right) \quad \text{Eq (2)}$$

In the following subsection we focus on the different configurations to acquire the reflectance.

Despite of the procedure to acquire the spectra, the next section introduces how the reflectance from gastric tissue can be modeled based on diffusion theory, focusing on the modifications of the reflectance from biological parameters. We mention the most relevant algorithms to estimate biological parameters from the reflectance.

### 2.3. Light transportation in biological tissues

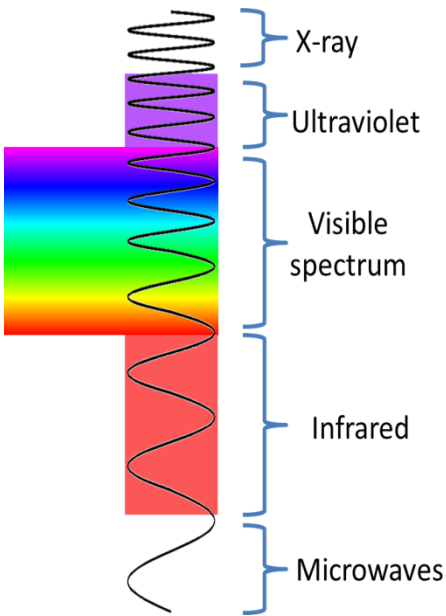
This section deals with the description of the phenomena that occurs during light tissue interaction. We start from the photon and the path that it could take once it interacts with tissue. In particular, we focus on how it can be absorbed or scattered depending on the chemical content and how the reflectance spectrum is generated from the biological

properties of the tissue. Then, we discuss the estimation of biological parameters from the spectrum.

### 2.3.1. Phenomena occurring during light tissue interaction

The photon is a quantum of electromagnetic energy, the elementary particle of light and electromagnetic (EM) radiation. This radiation is included in the EM spectrum, which is divided according to wavelengths. The visible region that humans can perceive is a small portion of the EM spectrum as presented in table 2.

Table 2. Spectrum of light [57].

Electromagnetic spectrum	Acronym	Name	
Below 100 nm	X-ray	X-ray	
100 to 400 nm	UV	Ultraviolet	
400 to 770 nm	VIS	Visible	
770 to 2500 nm	NIR	near infrared	
2500 to 25000 nm	MIR	mid infrared	
Above 25000 nm	Microwaves	Microwaves	

When a photon from a light source interacts with the tissue, there are 4 different possible paths that it can follow, depending on the architectural and chemical properties of the tissue [52][58]. These paths are scattering, absorption, reflection and transmission, as presented in figure 4. The main phenomena presented in tissues are absorption and scattering.

**Absorption.** Depending on the chemical content of the tissue, selective photons are absorbed at specific wavelengths. The main absorbers are named chromophores, such as hemoglobin or water [56], [59].

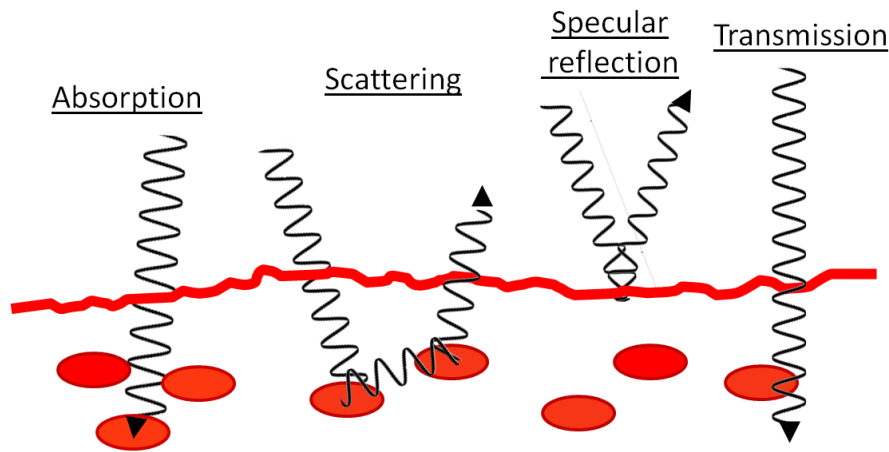


Figure 4. Principal phenomena involved in light tissue interaction.

**Scattering.** This phenomenon occurs when an element of the tissue makes the photon to change its direction. From the microscopical point of view, the scattering is mainly due to variations in the refractive index of particles in the medium. There are two types of scattering phenomena which depends on the size of the particles [56], [59], [60].

- *Rayleigh scattering* is experienced in a medium with particles that are smaller than the photon wavelength, such as small organelles and membrane of cells.
- *Mie scattering* is observed in a medium where particles are larger or equal than the photon wavelength; it includes collagen fibers.

**Reflection.** The photons interacting with the tissue follow the law of reflection so that the surface of the tissue acts as a mirror, making that angle of the incident light equal to the angle of the outgoing light. In this case, what is observed is the light source as a specular reflection [56], [59].

**Transmission.** The photon passes through the tissue to another layer.

Additionally to these phenomena, we must consider that each wavelength has a different penetration depth [58], which in practice, gives us the advantage of the analysis of a certain volume by sampling different paths. For example, the red wavelengths have a large penetration depth, whereas blue wavelengths have low penetration. In this case, blue wavelengths are used to highlight features from the surface.

In the following section we describe a model of light tissue interaction where the reflectance is estimated from optical properties such as absorption and scattering, which depend on biological parameters.

### 2.3.2. Theoretical model of light tissue interaction

It is important to realize that in light tissue interaction, the path of the photons is modified due to the phenomena previously described. There are different physical models developed to analyze this path, such as diffusion theory, Monte Carlo, Kubelka Munk theory among others [61], [62]. These methods are used to estimate the reflectance as a function of the optical and biological parameters.

Based on diffusion theory, the equation 3, which was proposed in [63], models the reflectance  $R(\lambda)$  of soft tissues, just as the one found in the stomach. It is based on applying the optical properties of tissues such as reduced scattering coefficient  $\mu_s'(\lambda)$  in  $[cm^{-1}]$ , absorption coefficient  $\mu_a(\lambda)$  in  $[cm^{-1}]$ , among others. In fact, the biological and morphological characteristics of tissue are encoded in these optical properties.

$$R(\lambda) = \frac{a'(\lambda)}{2} \left( 1 + e^{-(4/3)A\sqrt{3(1-a'(\lambda))}} \right) \frac{1}{1 + \sqrt{3(1-a'(\lambda))}} \quad \text{eq (3)}$$

where  $A$  is the internal reflection, which is defined in equation 4.

$$A = \frac{(1 + r_d)}{(1 - r_d)} \quad \text{eq (4)}$$

so that  $r_d = -1.4040n_{rel}^{-2} + 0.710n_{rel}^{-1} + 0.668 + 0.0636n_{rel}$ , taking into consideration that  $n_{rel} = n_t/n_v$  is the refractive index mismatch between air  $n_v$  and tissue surface  $n_t$ . In the case of the stomach,  $n_{rel}$  could vary between 1.36 and 1.45 [64][65].

Additionally,  $a'$  is the transport albedo defined in equation 5.

$$a'(\lambda) = \frac{\mu_s'(\lambda)}{(\mu_a(\lambda) + \mu_s'(\lambda))} \quad \text{eq (5)}$$

where  $\mu_s'(\lambda)$  is the reduced scattering coefficient, which describes the diffusion of photons undergoing several scattering events.  $\mu_s'(\lambda)$  is a decreasing function of wavelength and it could be modeled as presented in equation 6.

$$\mu_s'(\lambda) = \mu_{s'630nm} \left( \frac{\lambda}{630 \text{ (nm)}} \right)^{-b} \quad \text{eq (6)}$$

where the wavelength at 630 nm acts as a reference to normalize the wavelength  $\lambda$ ,  $b$  is the scattering power and it is dimensionless. It models the decreasing function of scattering and it could be interpreted as the size of the scatters. In the case of gastric tissue we assume  $\mu_{s'630nm}$  as  $7.7 \text{ cm}^{-1}$  and  $b$  as 1.4 [66][60].



Then,  $\mu_a(\lambda)$  from equation 5 is the absorption coefficient which gives information about the density of chromophores in a medium, modeled in equation 7.

$$\mu_a(\lambda) = B(S\mu_{a,oxy}(\lambda) + (1 - S)\mu_{a,deoxy}(\lambda)) + W\mu_{a,water}(\lambda) \quad \text{eq (7)}$$

where  $B$  is the blood volume fraction [ $B/100\%$ ],  $S$  is the oxygen saturation of hemoglobin [ $S/100\%$ ],  $W$  is water content [ $W/100\%$ ],  $\mu_{a,oxy}(\lambda)$  in [ $cm^{-1}$ ],  $\mu_{a,deoxy}(\lambda)$  in [ $cm^{-1}$ ] and  $\mu_{a,water}(\lambda)$  in [ $cm^{-1}$ ] are respectively the absorption spectra for oxygenated blood, deoxygenated blood and water [61][66].

In particular, we can analyze each of the 4 parameters individually ( $b$ ,  $B$ ,  $S$  and  $W$ ) in order to identify their contributions to the shape of the spectrum as illustrated in figure 5. The nominal values for the simulations are  $b = 1.4$ ,  $b \in [0.5 \dots 2.5]$ ,  $B = 0.005$ ,  $B \in [0.0005 \dots 0.0500]$ ,  $S = 0.75$ ,  $S \in [0 \dots 1]$  and  $W = 0.75$ ,  $W \in [0 \dots 1]$ . The ranges of these parameters are considered from extreme possible values [60], [66], [67].

We can clearly observe in figure 5.a that the changes in the scattering power are mainly in the UV and near infrared, with some significant variations in red wavelengths. In the case of the blood concentration from figure 5.b, variations are reported in UV, visible and near infrared spectrum. When the oxygen saturation varies as in figure 5.c, we observe changes in 420 nm which is an absorption peak of hemoglobin, some variations below 500 nm and in the red wavelengths; in particular, around 530 nm is observed complex changes which more likely are not suitable for diagnosis. Finally, the modifications in water content in figure 5.d are mainly presented in the near infrared.

Having a model of light tissue interaction, it is possible to simulate the reflectance from optical properties, which are calculated from biological parameters. However, diagnosis needs to reverse the model to estimate biological parameters from the spectrum. The exact solution exists for infinite media, which is never the case in our applications. In order to approximate a solution, strong assumptions and a priori hypotheses with respect to the range and initialization of biological parameters are required, with an initial guess close to the true values.

The nominal value and range of the optical parameters from the gastric tissue have been studied in [64]. Then, in order to estimate the biological parameters, the main approach is based on a Newton-type problem, so that some hypotheses of biological parameters are iteratively modified in the model of light tissue interaction to estimate a theoretical reflectance. Then, it is compared with the experimental data to find the closest match [61], [67]. This analysis was performed in [68] for normal, atrophic gastritis, ulcers and cancerous gastric tissues. The results of this study show that the blood concentration and oxygen saturation decreases in atrophic gastritis. The blood concentration is increased in a cancerous stage but with lower oxygen saturation. Additionally, there is an increase in

concentration of scatters with different sizes in atrophic gastritis, whereas in cancerous tissues, the concentration is reduced but the size is increased.

It is important to realize that fitting a model rarely produces exact solutions. In fact, it could lead to different situations, from non to multiple solutions. It is also possible to obtain biological values which are not physically possible. Besides these issues, we must add that the ground truth of biological parameters is very difficult to obtain. An acceptable global error in fitting the model is 20 % [68]. Other approaches already used in skin and excised colon tissues could be implemented in gastric tissue. For instance genetic algorithms [69], discrete Markov Random fields [70] among others.

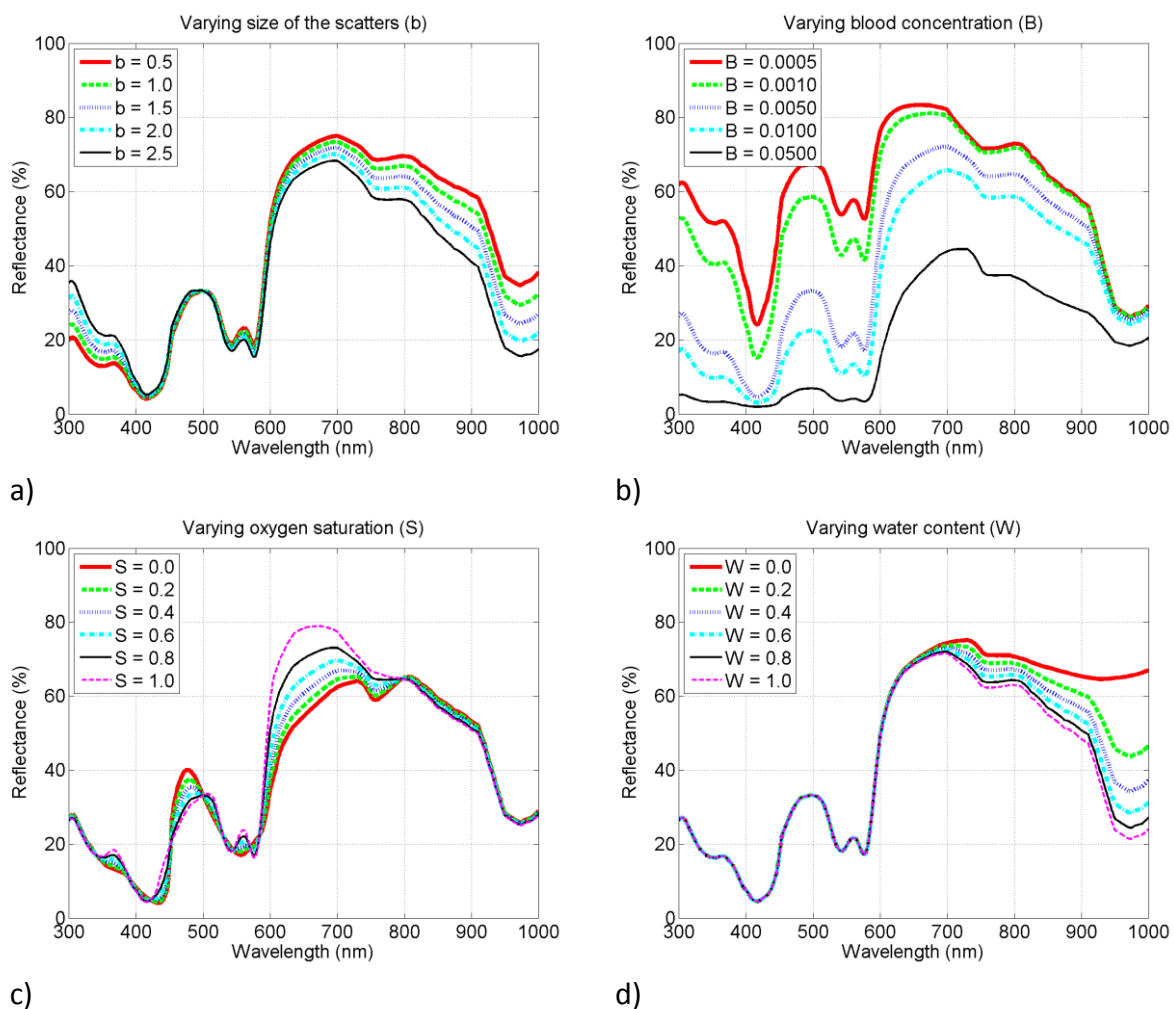


Figure 5. Individual contributions of the optical properties in the shape of the reflectance spectrum. a) varying the scattering power. b) variation of blood concentration. c) Modifications due to oxygen saturation and d) Changes due to water content.

Generally speaking, the most relevant constrains are related to the acquisition under controlled conditions of a high spectral resolution from the reflectance, which in particular, cannot be achieved during gastroendoscopy. Under these circumstances, other options have to be considered, based on statistical analysis and machine learning, aimed for

interpretation and classification of the spectra. These methodologies are explained in the following sections.

## 2.4. Statistical analysis of the spectrum

One widely used approach for the interpretation of the collected spectra is its statistical analysis. Generally speaking, when the distribution of a population is unknown, studies based on hypothesis test and non-parametric analysis are applied [71][72] and can be used for instance in medicine, in the evaluation of treatments and effectiveness of a drug.

In the case of this doctoral work, we can apply these analyses to identify the wavelengths that display significant changes between normal and pathological tissues, and can be used for diagnosis. The following subsections include the description of hypothesis test, how to compute the p value according to some relevant non-parametric methods for the statistical analysis of the collected spectra.

### 2.4.1. Hypothesis test and p value [71], [73], [74]

The hypothesis test is a tool to evaluate the data which is assumed as a random variable. It is the result from a statistical test, where suppositions about the mean or the probability distribution from the random variable are evaluated. It is typically based on the formulation of two mutually exclusive hypotheses and the acceptance of one of them. The first one is known as  $H_0$  or null hypothesis which is the hypothesis under test. The second one is  $H_1$  or alternative hypothesis.

In order to reject the null hypothesis, the p value is used and defined as “...the probability, when the null hypothesis  $H_0$  is true, of obtaining a sample result as extreme as, or more extreme than the observed sample result.” [73]

In consequence, if the p value is small, it is very unlikely that the sample is related to the observations by chance as observed in figure 6. In this sense, the p value is used as a collector of evidence from the data to reject the null hypothesis  $H_0$ .

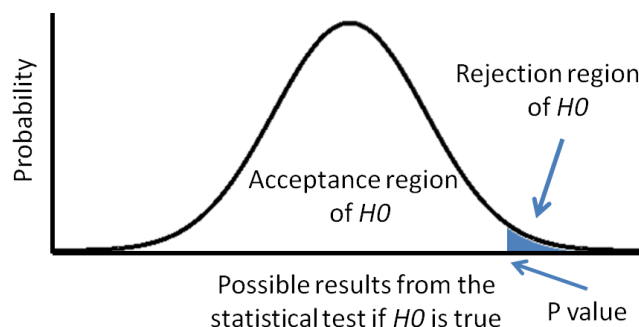


Figure 6. Possible results from a statistical test, where a small p value is evidence of rejection of the null hypothesis [75].

As an example, let us consider a group of samples  $x$ , originated from a normal distribution  $\mathcal{N}(\mu, \sigma^2)$  subject to  $\mu \gg 0$ , we formulate  $H0: \mu = 0$  and  $H1: \mu > 0$  so that,  $H1$  indicates low probability that the samples in the group were acquired from a population with  $\mu = 0$ . In this case, the p value is computed as  $\Pr(\alpha = 0 | \mu = 0)$  where  $\alpha$  is the mean of  $x$ . In general, this conditional probability is estimated by using a statistical test, such as Analysis of variance, Wilcoxon rank sum, Kruskal Wallis among others. Since in this example  $\mu \gg 0$ , the resulting p value from the statistical test is smaller than 0.05, which is a typical critical value to reject the null hypothesis.

It is also possible to be more rigorous than 0.05 in the level of significance, for instance 0.01 or even smaller [51]. This selection is defined in advance and depends on the nature of the data, the statistical test and the experience from the person performing the analysis.

The example discussed is a one-tail event (right tail), but it could be tested the left tail configuration by modifying the definition of the hypotheses as  $H0: \mu = 0$  and  $H1: \mu < 0$ . If the rejection region includes left and right tail, the hypotheses are defined as  $H0: \mu = 0$  and  $H1: \mu \neq 0$  to create a two-tailed test. It depends on the formulation of the hypotheses.

## 2.4.2. Statistical non-parametric analysis

In the statistical analysis of the data from unknown populations, it is typically preferable to use non-parametric test since in general no assumptions are required with respect to the population distribution [72]. Typically, the hypothesis  $H1$  is related to possible variations in centrality and changes in the distribution with respect to the observed samples. The following subsections are addressed to three non-parametric tests: analysis of variance, Wilcoxon-Mann-Whitney and Kruskal-Wallis. It is very important to highlight that there are many other non-parametric tests available.

### 2.4.2.1. Analysis of variance (ANOVA) [72], [73]

The analysis of variance (ANOVA) is a qualitative evaluation of independent samples based on the F-test. It is assumed that the samples were originated from a normal distribution. This test is applied to evaluate the evidence for significant differences between the means of the groups.

Let us assume that having  $N$  independent samples separated in  $k$  groups, each of them with  $n_i$  samples  $i \in (1, 2, \dots, k)$  so that  $N = \sum_{i=1}^k n_i$ . Each sample group has a mean  $\alpha_i$  which allows us to define the linear model in equation 8.

$$y_{ij} = \alpha_i + \varepsilon_{ij} \quad \text{eq (8)}$$

Where  $y_{ij}$  is the  $j^{th}$  sample from the  $i^{th}$  group and  $\varepsilon_{ij}$  is a normal random error  $N(0, \sigma_\varepsilon^2)$ . The hypothesis test is defined as  $H0: \alpha_1 = \alpha_2 = \dots = \alpha_k$  and  $H1: \text{Differences in the means}$ . The evaluation is based on an F distribution as illustrated in equation 9.

$$F_{val} = \frac{\frac{\sum_i^k n_i (\alpha_i - \alpha)^2}{k-1}}{\frac{\sum_i^k \sum_j^{n_i} (y_{ij} - \alpha_i)^2}{N-k}} \quad \text{eq (9)}$$

Then the exact p value is computed from the F distribution, by providing  $F_{val}$  with  $(k-1, N-k)$  degrees of freedom. Finally, it is compared with the level of significance defined for the study in order to reject the null hypothesis.

#### 2.4.2.2. Wilcoxon-Mann Whitney [72], [73], [76], [77]

Wilcoxon-Mann-Whitney is also known as Wilcoxon rank sum test. This test is applied to identify if the population medians is the same for the two groups. Let us consider two independent populations  $X$  and  $Y$ , with  $n_1$  and  $n_2$  samples respectively. When the samples are arranged together and ranked, we can identify patterns and relationships between the two populations. For instance, if the samples have the same median, the probability that  $x_j$  is greater or smaller than  $y_l$  is the same.

Let us define the distribution function for each group as  $G(x)$  and  $G(y)$ . Then we can define a shift  $\vartheta$ , so that  $G(y) = G(x - \vartheta)$ . Consequently the two hypotheses to test are  $H0: G(y) = G(x)$  and  $H1: G(y) = G(x - \vartheta)$  for a  $\vartheta \neq 0$ .

In order to proceed with the test, the samples from the two groups are sorted incrementally in a single sequence, which allows us to define the indicator in equation 10.

$$D_{jl} = \begin{cases} 1 & \text{if } y_l < x_j \\ 0 & \text{Otherwise} \end{cases} \quad \text{for } j = 1:n_1, l = 1:n_2 \quad \text{eq (10)}$$

Then, Mann Whitney U statistic is defined in equation 11.

$$U = \sum_{j=1}^{n_1} \sum_{l=1}^{n_2} D_{jl} \quad \text{eq (11)}$$

This is used to compute the parameter W in equation 12.

$$W = U + \frac{n_1}{2} (n_1 + 1) \quad \text{eq (12)}$$

Then the Z value is calculated following equation 13.

$$Z_{val} = \frac{\left| W - \frac{n_2(n_1 + n_2 + 1)}{2} \right|}{\sqrt{\frac{n_1 n_2 (n_1 + n_2 + 1)}{12}}} \quad \text{eq (13)}$$

The p value is obtained from  $Z_{val}$  in a Z distribution. Finally, the p value is computed with the level of significance from the study. The advantage of this approach is that it works with ranks and can be used with normal or discrete data. Therefore, it is widely applied in the biological and medical domains [71] [72].

### 2.4.2.3. Kruskal Wallis test [72], [73], [76]

It is considered as an extension for more than 2 groups of the Wilcoxon rank sum test, which is applied to establish if the samples are originated from the same distribution. Since it is oriented to  $k$  groups ( $k > 2$ ), the hypotheses to test are defined as  $H0: \vartheta_1 = \vartheta_2 = \dots = \vartheta_k$  and  $H1: \text{There is at least a pair } \vartheta_i \neq \vartheta_j$ . The statistical test is defined in equation 14.

$$H = \left( \frac{12}{N(N+1)} \sum_{i=1}^k \left( \frac{R_i^2}{n_i} \right) \right) - 3(N+1) \quad \text{eq (14)}$$

where  $N$  is the total of samples and  $R_i$  is the summation of ranks in the  $i$  group. The  $H$  value is used to compute the p value in a chi-square distribution with  $(k - 1)$  degrees of freedom. Finally, the obtained p value is compared with the level of significance defined in the statistical study.

After the statistical evaluation of the spectrum and the validation that there is a significant statistical difference between the two groups, the next step is the classification of tissues according to their pathology.

## 2.5. Classification framework

This section is devoted to supervised machine learning approaches for the classification of tissues according to their pathology. It is based on extraction of statistical features from the spectrum and classification algorithms.

### 2.5.1. Preprocessing of the spectrum

Multispectral images collected during gastroendoscopy display in general strong variations in the amplitude of the measured spectrum. This situation is the result from the non-homogeneous illumination and the different distances between gastric tissue and the camera during the acquisition.

Under these circumstances, we can rely only on the shape of the spectrum and not on its amplitude to differentiate pathological tissues. Therefore, in order to compare the collected spectrum, it is considered as scattering points in a  $q$ -dimensional Euclidean space [78], so that the spectrum of a pixel is defined in equation 15.

$$x = \{x_1, x_2, \dots, x_q\} \quad \text{eq (15)}$$

where  $q$  is the number of wavelengths of the multispectral image. We consider the normalization L1 as presented in equation 16.

$$z_i = \frac{x_i}{\sum_{j=1}^q x_j} \quad \text{so that} \quad \sum_{i=1}^q z_i = 1 \quad \text{eq (16)}$$

where  $x_i$  is the  $i^{th}$  wavelength of the collected spectrum and  $z_i$  is the  $i^{th}$  wavelength of the normalized spectrum. This normalization forces the energy of the spectrum to be the same for all the samples.

Once the acquired spectrum is normalized, the next step is to extract and select features from the spectrum for classification, which are addressed in the following section.

### 2.5.2. Feature extraction and selection

In this work, we are interested in the shape of the spectrum since it encodes the biological characteristics of the mucosa. In order to extract features from it, we consider the spectrum as a probability distribution, so that it can be modeled statistically [79]–[81]. The advantage of statistical features is that they represent quantitative values of the collected data.

Let us define as an example a vector of features  $T = \{f_1, f_2, \dots, f_w\}$  presented in table 3, where it is included the statistical descriptors and the measurements of the normalized spectrum as defined in equation 16.

Table 3. Example of features.

Feature	Definition
Mean of absolute deviation	$\frac{1}{q} \sum_{i=1}^q  z_i - \text{mean}(z) $
Mean deviation about median	$\frac{1}{q} \sum_{i=1}^q  z_i - \text{median}(z) $
Standard deviation	$\sigma(z)$
Median of absolute deviation	$\text{MAD}(z)$
Variance	$\sigma^2(z)$
Skewness	$\left( \frac{1}{q} \sum_{i=1}^q (z_i - \bar{z})^4 \right) / \left( \frac{1}{q} \sum_{i=1}^q (z_i - \bar{z})^2 \right)^{3/2}$
Entropy	$-\sum_{i=1}^q \left( \frac{k_i}{N} \log \frac{k_i}{N} \right) + \log \left( \frac{\max(z) - \min(z)}{N - 1} \right)$
Kurtosis	$\left( \frac{1}{q} \sum_{i=1}^q (z_i - \bar{z})^4 \right) / \left( \frac{1}{q} \sum_{i=1}^q (z_i - \bar{z})^2 \right)^2$
Reflectance	Spectral measurement at specific wavelengths
Ratios	Ratio between different wavelengths

After having a set of descriptors, a key point in a classification approach is to select among these features the ones that have high discriminative potential to differentiate between the groups. In this sense, we search for an efficient feature subset. In general, we consider the evaluation criteria of the features to differentiate between three main approaches which are wrappers, filters and embedded methods [82].

### 2.5.2.1. Wrapper approach

Wrapper approaches are strongly related to the classification algorithm since it searches for the subset of features that produces high performance from the learning algorithm. In general, it takes in consideration the interaction of a feature subset, handling their dependencies and redundancies. It includes as disadvantages the high risk of overfitting, its computational cost and the strong dependence with the classifier [83], [84].

There are different examples in the literature of this approach, such as exhaustive search, where all possible combinations of subsets of features are tested. This case can only be applied with low numbered features since it is impractical in a big feature set. Another approach is forward selection which is an iterative method. It starts from an empty feature vector in which a feature is added at each iteration. In this step, all the variables that are not part of the set are evaluated, so that only the feature which inclusion is the most significant for the classification task will be added. Similar case for backward elimination,



with the difference that it starts with the full set of features, from which non-significant features are removed at each iteration. There are different options to stop these methods, such as reaching a fix number of variables, identifying no improvement when features are added or removed [82], [83], [85]. Another interesting approach includes the use of artificial intelligence which is the case for example of genetic algorithms, which is a stochastic search inspired in biological evolution [82], [83].

### 2.5.2.2. Filter approach

In the case of filter approaches, the evaluation criterion does not involve the classifier algorithm, providing ranked features independent from the classification algorithm. The output is a relevance index where the features are sorted according to their discriminative power to differentiate the groups. The main disadvantage of this approach is with respect to the interdependences between features, since they are not taken into account. In some specific circumstances, this situation could be considered as an advantage since redundant features are more robust in the case of noisy data.

There are different examples of filter approaches for instance those based on statistical test which have been proof to be powerful methods and therefore, they have been widely used. It includes correlation based filters, where the strength of association between features is measured by Pearson correlation, by Chi square statistics or by t-test statistics [82]–[84].

The application of t-test for feature selection requires two assumptions: normal distribution and equal variance between the classes. The t-test [83] is divided in two parts. Firstly the pooled variance  $\sigma_p^2$  is computed as presented in equation 17 where  $n_1$  and  $n_2$  are the number of samples for each class and  $\sigma_1$  and  $\sigma_2$  are their standard deviations.

$$\sigma_p^2 = \frac{(n_1 - 1)\sigma_1^2 + (n_2 - 1)\sigma_2^2}{n_1 + n_2 - 2} \quad \text{eq (17)}$$

The second step is the computation of the t value as presented in equation 18, where  $\alpha_1$  and  $\alpha_2$  are the mean of each class.

$$t = \frac{|\alpha_1 - \alpha_2|}{\sqrt{\sigma_p^2 \left( \frac{1}{n_1} + \frac{1}{n_2} \right)}} \quad \text{eq (18)}$$

As a result of this procedure, the features are ranked according to their contributions on the separability between two classes.

### 2.5.2.3. Embedded approach

This approach is oriented to learn the features which contribute to the classification while the classifier is trained. Therefore, it could be oriented as an optimization problem where the use of a large number of features is penalized, aimed to create a compact subset of features which are significant for the prediction of the classes. They have the advantage that it is not required to split the data set for training and testing [83], [84].

Some examples of this approach include regularization algorithms such as LASSO (Least Absolute Shrinkage and Selection Operator), which is used for feature selection and shrinkage [83], [86], [87]. We can also find decision trees [82] where the feature vector is divided depending on the “splitting criterion”, such as mutual information.

Some significant algorithms for classification are discussed in the next subsection.

### 2.5.3. Classification algorithms

The analysis and interpretation of the data collected from multispectral imaging is a non-trivial task. Thus, we take advantage of classification and learning algorithms in order to highlight differences in the tissues due to pathology. Generally speaking, classification is oriented to define the separation rule  $R_T$  so that  $R_T: J \rightarrow G$ , where  $G \in \{\text{normal tissue, pathological tissue}\}$  and  $J$  is the sample set so that unseen samples can be separated in one of the two classes.

In the present doctoral work we apply three common supervised approaches to create the separation rules. In this sense, the following paragraphs are oriented to describe these methods for classification, which are  $k$  nearest neighbor, support vector machine and neural networks [52].

#### 2.5.3.1. K nearest neighbor [86], [88]

The  $K$  nearest neighbor classifier ( $k$ -nn) is considered a simple and highly performing algorithm which is applied as a baseline to compare other classifiers. This algorithm is based on the minimal Euclidean distance between the sample under test  $x$  and the  $k$ -closest samples from the training sample, depending on  $k$  as the number of neighbors to be considered. Then, the sample under test will be assigned the class of the majority of its  $k$  nearest neighbors. This principle is defined in equation 19.

$$\hat{Y}(x) = \frac{1}{k} \sum_{x_j \in N_k(x)} y_j \quad \text{eq (19)}$$

Where  $\hat{Y}(x)$  is the assigned class for the sample under test  $x$ ,  $N_k(x)$  is the neighborhood of  $x$  which includes  $x_j$  samples so that  $j \in \{1:k\}$  and  $y_j$  is the class of those closest neighbors.

### 2.5.3.2. Support Vector Machine (SVM) [86], [88], [89]

SVM is a well-known classifier which shows high performance and robustness in many classification tasks.

The principle of SVM is that the input data is projected into a high dimensional space. Then, it is in this space where a hyperplane is defined, as shown in figure 7.

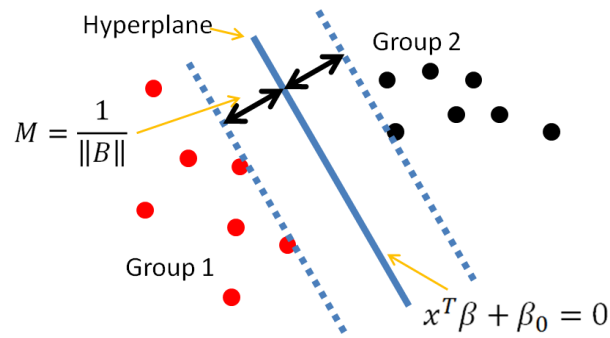


Figure 7. Hyperplane which defines the decision boundaries between two groups in a SVM classifier.

The hyperplane is defined according to equation 20.

$$f(x) = x^T \beta + \beta_0 = 0 \quad \text{eq (20)}$$

where  $x$  are the training samples,  $\beta$  is a unit vector, so that  $\|\beta\| = 1$ ,  $\beta_0$  is a constant and  $f(x)$  is the function of the hyperplane which produces the maximum separation between the training samples from the two classes. This margin  $M$  in equation 21 is not surprisingly equidistant to the closest nearest samples from the two classes.

$$M = \frac{1}{\|B\|} \quad \text{eq (21)}$$

The classification rule in the hyperplane is defined in equation 22.

$$\hat{Y}(x) = \text{sign}[x^T \beta + \beta_0], \quad \hat{Y} \in \{1, -1\} \quad \text{eq (22)}$$

### 2.5.3.3. Neural Networks using Generalized Relevance Learning Vector Quantization [90]–[94]

Neural Networks (NN) using generalized relevance learning vector quantization is a robust and performant classifier. Similar to other neural network approaches, it has three layers implemented. The input layer is oriented to include the input data. The output layer contains the possible classes or outcomes of the classification. The hidden layer is where the separation rules are estimated.

Let us consider having a set of training samples  $x$  with  $C$  number of classes, where each sample  $x_i$  has multiple components such that  $x_i^q$  is the  $q^{th}$  element of the  $i^{th}$  samples of  $x$ . Additionally, a fix number  $M$  of prototypes  $W = \{w_1, w_2, \dots, w_M\}$  also named codebook or weight vectors are initialized for each class. The prototypes which are better representatives of the class have higher weights. Thus, the learning is performed by minimizing the sigmoid function  $f$  of a relative distance measurement defined in equation 23.

$$S = \sum_{j=1}^N f\left(\frac{d_{\gamma}^{+}(x_j) - d_{\gamma}^{-}(x_j)}{d_{\gamma}^{+}(x_j) + d_{\gamma}^{-}(x_j)}\right) \quad \text{eq (23)}$$

where  $d_{\gamma}^{+}(x_j)$  is the square Euclidean distance between  $x_j$  and the closest prototype  $w_{+}$  belonging with the same class of  $x_j$  and  $d_{\gamma}^{-}(x_j)$  is for the closest prototype  $w_{-}$  with different class of  $x_j$ . In particular, a relevance factor is included in the distance measurement as shown in equation 24

$$\|x_j - w_l\|_{\gamma}^2 = \sum_{i=1}^q \gamma_i (x_j^i - w_l^i)^2 \quad \text{eq (24)}$$

where  $\gamma_i$  is the  $i^{th}$  weight, subject to  $\sum_i^q \gamma_i = 1$  and  $\gamma_i \geq 0$ . We used  $\gamma_i$  instead of  $\lambda_i$  which is typically used in literature to avoid confusion with the wavelength. The update of this relevance factor is shown in equation 25.

$$\gamma_j = \begin{cases} \gamma_j - \epsilon (x_j - w_l)^2 & \text{if } x_j \text{ and } w_l \text{ belong to the same class} \\ \gamma_j + \epsilon (x_j - w_l)^2 & \text{otherwise} \end{cases} \quad \text{eq (25)}$$

where  $\epsilon$  is a learning factor subject to  $\epsilon \in [0, \dots, 1]$ . The learning rules are computed from the derivatives of equation 23, so that the prototypes  $W$  which are near to the correct classified training samples are better representatives of the classes.

After reviewing these three common supervised classification algorithms, the next subsection is dedicated to evaluate the performance of the classification methodology.

## 2.5.4. Evaluation of the classification performance

Generally speaking it is required to separate the dataset in training and testing in order to evaluate the performance of a classifier. However, in many cases this cannot be achieved due to the small size of the database.

Typically, cross validation is performed to estimate the performance of the classification methodology when the available database is small. Additionally, the bias is reduced since each iteration has different data for training. In practice, if a filter approach is applied, the selection of features should also be included in the cross validation in order to avoid any bias.

In our case, we apply Leave One Patient Out Cross Validation (LOPOCV) [95] since it is observed that samples from the same patient are in general strongly correlated. LOPOCV is an iterative process where the full information from a patient is removed in order to be used for testing, whereas the remaining of the database is used for training the classifier. This procedure is repeated until all the patients have been tested.

There are different metrics to estimate the performance of a classifier. In a binary classification, we compare the ground truth with the predicted outcome. For this purpose, a confusion matrix is presented in table 4 which includes the different possible outcomes from a sampled after classification.

Table 4. Confusion matrix of possible outcomes from the classification.

		<u>Ground truth</u>	
		Pathological tissue (positive)	Normal tissue (negative)
<b>Predicted results</b>	Pathological tissue (positive)	True positive ( <b>TP</b> )	False positive ( <b>FP</b> )
	Normal tissue (negative)	False negative ( <b>FN</b> )	True negative ( <b>TN</b> )

Some parameters related to the performance of the classification include the accuracy, which indicates the percentage of samples that are correctly classified. The sensitivity or recall shows the percentage of spectra from pathological tissues that are correctly classified. The specificity is the percentage of spectra from normal tissues that are correctly identified [96], [97]. These parameters are shown in equations 26, 27 and 28 respectively.

$$Accuracy = \frac{TP + TN}{TP + FP + FN + TN} \quad \text{eq (26)}$$

$$Sensitivity = \frac{TP}{TP + FN} \quad \text{eq (27)}$$

$$Specificity = \frac{TN}{TN + FP} \quad \text{eq (28)}$$

Other parameters are the precision or positive prediction factor, which indicates the chance that a positive prediction is correct, defined in equation 29

$$Positive\ prediction = \frac{TP}{FP + TP} \quad \text{eq (29)}$$

F-score combines the precision and sensitivity so that  $F_1 = \frac{(Precision)(sensitivity)}{Precision + sensitivity}$

There are many options to estimate the performance of the classification approach. Depending on what is desired to evaluate, some parameters could be more significant than others, for instance, having high sensitivity and high specificity is the ideal case because there are few chances that pathological tissue will be missed. However, this cannot be always achieved; it could be the case of a system which shows high sensitivity and low specificity. In this case, a sample identified as pathology will have high chances of being pathological but, there could be many false positives due to the low specificity. On the other hand, high specificity and low sensitivity could bring some certainty that the tissue is normal but once more, the risk of having false negative is traduced in pathological tissue missed. Between these two circumstances we would rather have false positives, so that these patients could have further medical studies to corroborate the results. The selection of the evaluation parameters remains to the user.

## 2.6. Summary

In this section we have addressed how to acquire multispectral images, the reflectance spectrum and how it is related to biological parameters of the tissue. In particular, we have described a model of light tissue interaction based on diffusion theory, describing the different phenomena involved. These phenomena modify the path of the photons and are the responsible for the changes in the spectrum, mainly modifying absorption and scattering. These properties are modified in the tissues depending on their biological and architectural composition of the tissue.

Taking in consideration the acquisition conditions in the stomach, an interesting option in the task of identifying changes in the spectrum due to the development of the pathology could be performed by statistical analysis, taking advantage of non-parametric analysis. Another option is the use of machine learning techniques. In this sense, we detailed how to process the acquired spectrum, focusing on the extraction of features from the spectrum based on a statistical approach and the methodology to select those who could be more

relevant for the classification task. In particular, the filter approach allows obtaining an independent rank of features from the classifier applied.

We also briefly described well-known supervised algorithms for classification, i.e. K-nn, SVM and Neural Networks. We explained also how to evaluate their performance: in particular LOPOCV is a powerful tool in case of data sets with a low number of patients. It is important to realize that LOPOCV requires performing the feature selection and the training of the classifier with the same subgroup of patients to avoid a possible bias in the classification. Different parameters were discussed for the analysis of the classification performance. They strongly depend on the characteristics that the user decides to evaluate from the classifier.

## Chapter 3

# Reflectance of gastritis pathology under controlled conditions

Gastritis is part of the stages described in the cascade of cancer development resulted from a chronic infection by *H. pylori* [9]. As mentioned in the chapter 1, there is a direct link between *H. pylori* and gastric lesions which has been demonstrated by epidemiological studies in animal models and also in humans [98], [99]. The mice model develops different stages of a chronic gastritis, originated in a chronic infection from *H. pylori* within months after inoculation. This bacterium infects half of the world population and it is considered type I carcinogen by the World Health Organization [15], [100], [101].

The subject of this chapter turns on the analysis of the reflectance acquired from a mice model of infection of *H. pylori*, aimed to identify the wavelengths which show the most significant changes due to the development of the pathology. These identified wavelengths are candidates for diagnosis of gastritis.

### 3.1. Model of experimentation

The pathogenesis resulting from the infection by *H. pylori* is a dynamic process where the mechanisms involved are difficult to identify. Under these circumstances, a fundamental part of biological research is the development of animal models of infection in a controlled environment. These models are used to understand the origin and development of diseases, the response of the host, the mechanisms involved and the environmental influences and could also be used to test reverting strategies, treatments and vaccinations [100].

Studies under controlled conditions require monitoring factors such as culture viability of the bacteria *H. pylori*, infection process, frequency of dosing, diet of the animal model, temperature conditions and microbial circumstances of the setting. In this sense, we worked with the unit of pathogenesis of *Helicobacter* in the department of microbiology from the Institut Pasteur in Paris, which has been studying *H. pylori* infection.



In the study of pathologies in the stomach originated in a *H. pylori* infection, we must consider two characteristics to develop an accurate model infection. The first one is the animal model or host. The second one is the strain of the bacteria which can colonize the stomach. In the following sections we will detail the applied combination of animal host and bacterium strain implemented for this doctoral work.

### **3.1.1. Mice model**

Early studies on *H. pylori* tested several potential hosts, such as piglets, primates, cats, mice, dogs, gerbils and ferrets which are colonized by their own species of *Helicobacter*. Generally speaking, it is preferable to use the smallest practical animal which models the features of the pathology under study, such as the mouse. It includes the advantage of fast reproduction; it is easy to inoculate and cost-efficient for the study.

In spite of the mentioned advantages of using a mice model, there are some disadvantages that should be taken into consideration, for instance the biological variations in mucosa, physiology of the stomach and the limited genetic diversity of the host and the bacteria. Unfortunately, these disadvantages could not represent the pathology in a diverse population of host or patients. Besides, the mice could develop gastric lesions which are only specific for the mouse such as mucous metaplasia [100].

Nowadays, there are different mice models available for studies such as the Swiss mice, strains NMRI, C57BL/6, C3H/HE [77] among others. It is important to mention that the infection in each model could vary. In the present doctoral work, we used the mice NMRI which could develop a chronic infection by *H. pylori* [102]. The next section will address the *H. pylori* strain SS1.

### **3.1.2. *H. pylori* strain SS1**

There are more than 35 discovered species of *helicobacter* but only few of them could produce gastritis in humans, which are *H. pylori*, *H. felis*, *H. fennelliae*, *H. cinaedi* and *H. Heilmannii* [103]. This is due to the species barrier which is a natural mechanism that limits a disease to spread between one type of animal to another. This constraint reduces the capability of the bacterium to colonize the host, which in our case, restricts the development of models of infection of a bacterium specialized in humans. Under these circumstances, early studies worked with strains obtained from cats and ferrets which were successfully tested in mice, but the studies were limited to specific lesions, for instance *H. felis* could induce advanced gastric lesions and *H. Heilmannii* could develop lymphomas [100].

The human *H. pylori* strain SS1 was successfully developed in 1997. Also named Sydney strain, it adheres to the epithelium of mice stomach in high numbers and for a long period.

The gastric mucosa of the mice showed strong similarities in the development of the infection in humans, including histology and architectural modifications. Additionally, it is *cagA* and *vacA* positive, which are antibodies for identification of the bacterium [99], [100], [104]. Thanks to these advantages, it has been widely used on research.

## **3.2. Mice experiments**

The ideal case to study the development of pathology is having sufficient amount of subjects from which we can follow their evolution so that multiple samples could be acquired during a period of time. Unfortunately, this is not our case, since the sacrifice of the mice is required to analyze its stomach. Under these circumstances, a typical approach is to use two groups: pathological (inoculated with *H. pylori*) and control (*H. pylori* free). This configuration allows collecting independent samples at different stages of the pathology with the control group as a reference. The experiments on mice were approved by the Institut Pasteur safety animal care and ethic committee in accordance with European guidelines.

In this subsection, we will describe the infection methodology and the different campaigns of sacrifice, giving special emphasis to the characteristics of the pathological tissues.

### **3.2.1. Infection by *H. pylori* strain SS1**

For this study, the bacteria were grown on blood agar base 2 (Oxoid Lyon, France) plates supplemented with 10% defibrinated horse blood (bioMérieux, Marcy L'Etoile, France) and an antibiotic-antifungal mixture consisting of vancomycin (10mg/ml), polymixin B (2.5IU/L), trimethoprim (5mg/ml) and amphotericin B (4mg/ml). The plates were incubated at 37°C for 24 to 48h under microaerobic conditions (7% O<sub>2</sub>, 10% CO<sub>2</sub>; Anoxomat™ system).

In total twenty five NMRI female mice of five-weeks old were acquired from Charles River Laboratories (France). These pathogen-free mice were housed in polycarbonate cages and acclimatized during one week before starting the experiments. 15 mice were orogastrically inoculated with 150 µl of a suspension of bacteria (10<sup>8</sup> colony forming unit (cfu)/ml) and 10 non-infected mice received 150 µl of peptone broth.

### **3.2.2. Campaigns of acquisition**

In the study of the stages of gastritis development, we consider that the changes in tissue are originated on the development of the pathology. For this purpose, a total of 25 mice were sacrificed after 1, 3, 7 and 12 months post inoculation, as presented in figure 8.

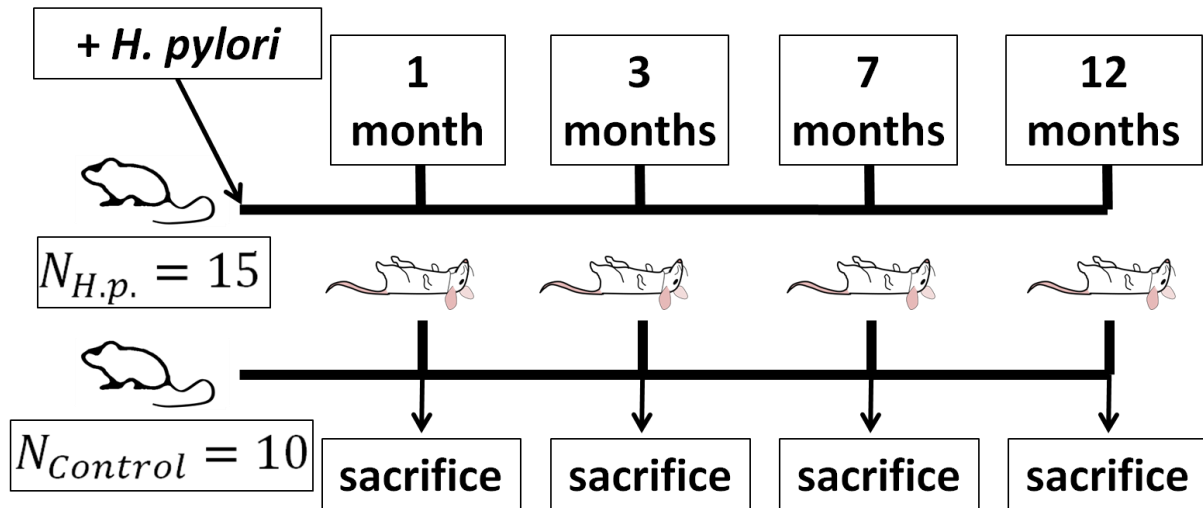


Figure 8. Acquisition campaigns and mice infected with *H. pylori* strain SS1.

In each acquisition campaign the mice were euthanized using CO<sub>2</sub> inhalation. Their stomachs were excised and opened from the greater curvature. In figure 9 is displayed a stomach on one side with a chess pattern for reference, where each square is 2 mm side. Thanks to this information we estimate the surface of the stomach as 130 mm<sup>2</sup>. This example is slightly bigger than the average of the sacrificed mice with mean size equals to 119 mm<sup>2</sup> with a standard error of the mean of 15.

In all the acquisition campaigns no macroscopical lesions were observed on the surface of the mucosa. Fragments containing antrum and fundus were used for histology analysis of the gastric inflammatory lesions and *H. pylori* gastric colonization assessment. This procedure is described in the next subsection.

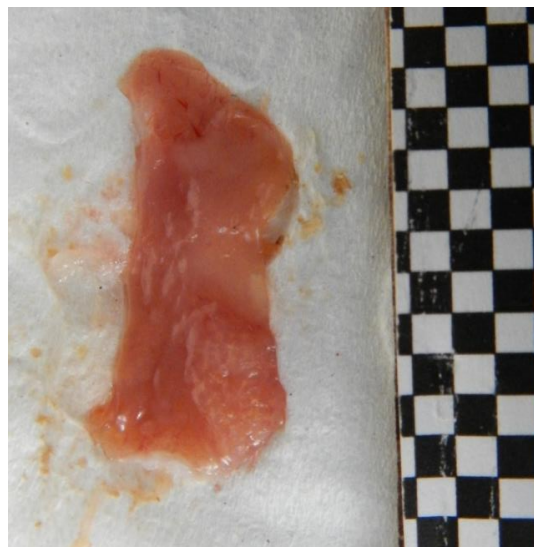


Figure 9. Stomach from a mouse, with a chess pattern of 2 mm side of the square for reference.

### 3.2.3. Analysis of biopsies from mice stomachs

The biopsies from gastric tissue were fixed in RCL2® (Alphelys, France) and embedded in low-melting-point paraffin wax (Poly Ethylene Glycol Distearate; Sigma, USA). Sections of 4  $\mu\text{m}$ -thick were stained by hematoxylin and eosin treatment (H&E) and examined blindly for histopathologic lesions [105], [106] by L. Fiette, senior pathologist from the Institut Pasteur. A typical image of histology is observed in figure 10. We observe the presence of granulated tissue associated with inflammatory cell infiltrates.

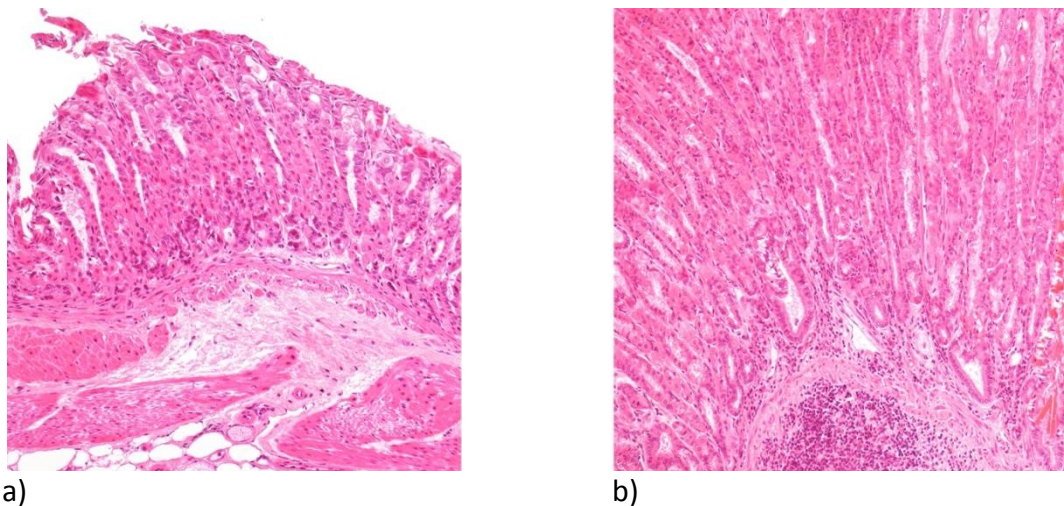


Figure 10. Histological analysis of gastric mucosa magnified 10x, a) non infected mice and b) mice infected with *H. pylori* SS1 and sacrificed after 12 months post inoculation, which displays granulation tissue associated with inflammatory infiltrates.

### 3.3. Acquisition of the reflectance from mice stomachs

The reflectance from the dissected stomach was measured using two systems. The first one is the spectrometer Konica Minolta CM-2600d from Konica Minolta Co Ltd, Osaka, Japan. The second one is the multispectral camera Flux Data FD1665 from Flux Data Inc, Rochester, USA. These devices are displayed in figure 11.

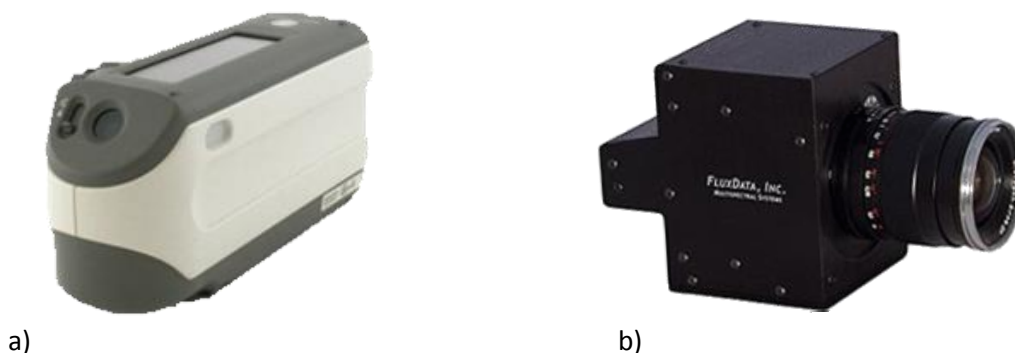


Figure 11. Acquisition systems a) spectrometer Konica Minolta CM-2600d and b) multispectral camera Flux Data FD1665.

### 3.3.1. Spectrometer Konica Minolta CM-2600d

The spectrometer Konica Minolta includes a light source and a small integration sphere of 52 mm diameter. This instrument is used to retrieve the reflectance of the measured surface from 400 nm to 740 nm each 10 nm in a circular area of 6 mm diameter. This system acquires a high spectral resolution in the visible range but it does not include NIR wavelengths. Additionally, it requires a black and white calibration before being used. Measurements of the intensity of the reflectance were performed on 4 randomly distributed areas of mucosa on each stomach, as displayed in figure 12.

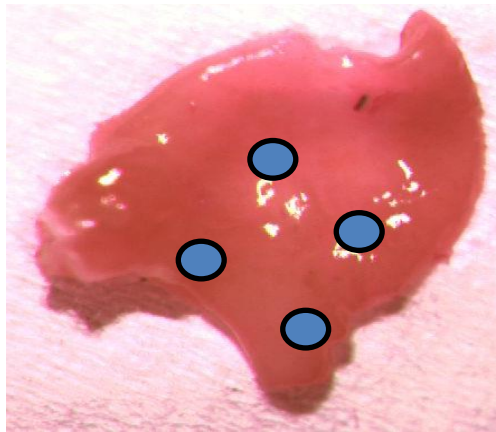


Figure 12. Point measurement of reflectance by the spectrometer at 4 random locations.

### 3.3.2. Multispectral camera Flux Data FD1665

#### 3.3.2.1. Characteristic of the camera

The multispectral camera Flux Data retrieves 7 monoband images, from which 6 are from the visible spectrum (2 images at different bands from the blue, green and red wavelengths) and 1 in the near infrared. Even though the spectral resolution is inferior in comparison with the spectrometer, the advantage is the spatial resolution and the acquisition of the NIR waveband.

Physically, this camera has 3 independent sensors for the acquisition. The images are acquired almost at the same time. The measured delay between the trigger from each sensor is 1 ms. The acquisition software was developed in C++ and it takes advantage of the SDK from the manufacturer. In figure 13 is displayed the normalized sensibility of each channel from the multispectral camera.

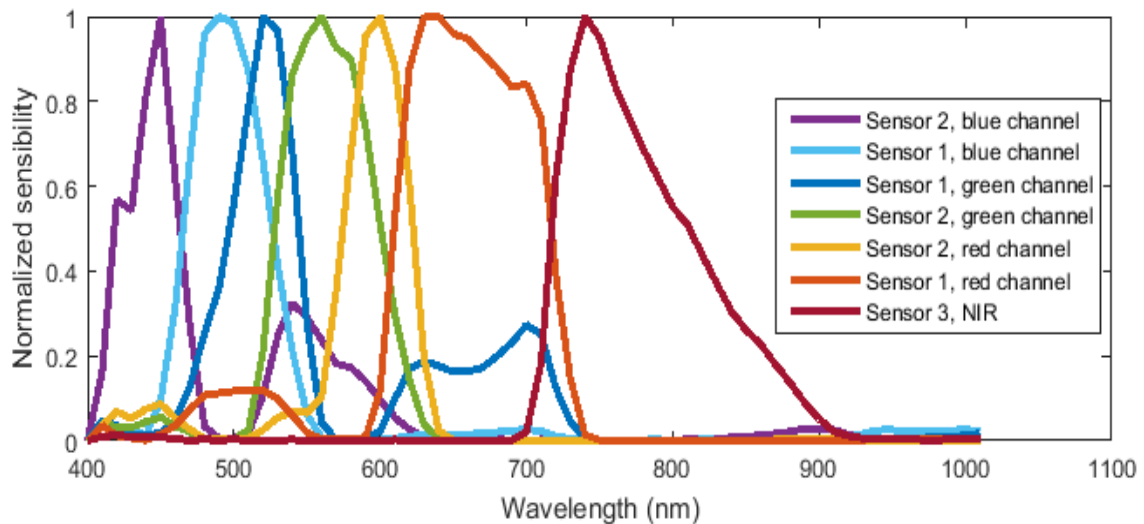


Figure 13. Normalized sensibility of each channel of the multispectral camera Flux Data FD1665.

The light source used for the acquisition of the reflectance was a Xenon lamp, which is typically found in the medical domain. The geometry between the multispectral camera and the light source plays an important role in the measurement. The system is configured at  $45^\circ$  between the light source and the multispectral camera. Additionally, 2 linear polarizers are included, one for the light source and the other for the multispectral camera configured in cross polarization. The polarizers and the geometric alignment are used to reduce the areas of specularity in the multispectral images. The general view of the setup is displayed in figure 14. A white calibration was performed before each acquisition campaign.

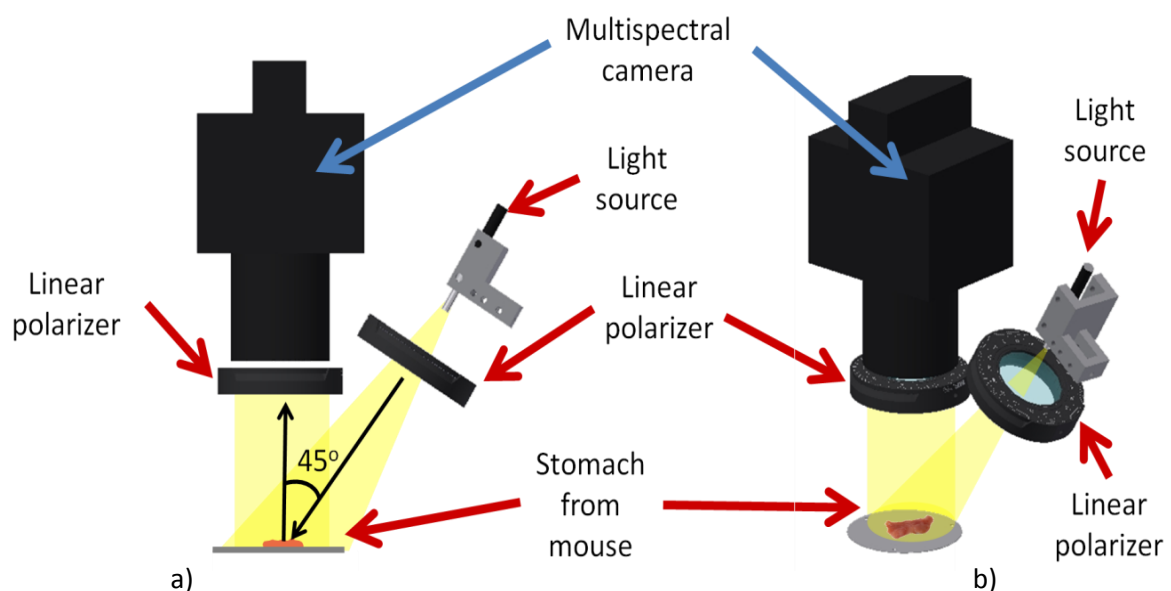


Figure 14. Set up for the acquisition for the multispectral acquisition of ex vivo samples from mice stomach a) front view and b) isometric view.

### 3.3.2.2. Stomach segmentation from multispectral image

In the acquired multispectral images from the mice we can observe the stomach, the background which is a white tissue and sometimes some traces of blood. In order to extract the mice automatically we take in consideration the homogeneity of the surface of the stomach in comparison with the rugosity from the background. Taking advantage of this characteristic we developed an algorithm based on texture. This procedure is detailed in figure 15 and explained in the following paragraphs.

The multispectral image includes the wavelengths in the visible range. Thus it is straight forward to compute a white light image as if it were observed by the naked eye. For this work, the computed image has only visualization purposes since it facilitates the observation of the background, the stomach and its shadow as displayed in figure 15.a).

The simulated white light image is obtained by removing the NIR channel and separating the 6 remaining channels in pairs which are later on averaged to obtain an RGB image so that the first two wavebands are used for the blue channel, the third and fourth channels are the green channel and the fifth and sixth wavebands are used for the red channel.

In the case of the automatic segmentation, we use the third waveband of the multispectral image which is the green channel from the first sensor. This image is displayed in figure 15.b). In general, the green channel is used in applications of computer vision because most of the color cameras are based on a Bayern patter. This configuration has the particularity that green sensors are more numerous than red and blue [107] so that, the output green image is the result from a higher population of samples.

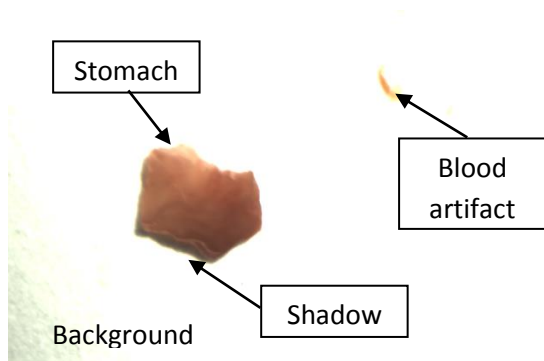
The edges of the object are obtained by applying a high pass sobel filter of 3x3 pixels in horizontal configuration which is displayed in equation 30. Thanks to this filtering we obtain an image  $I_x$  with the horizontal edges. The pixels in the border of the image were duplicated so that 2 extra rows and 2 extra columns are included to apply the filter and retrieve an image of the same size.

$$I_x = \begin{bmatrix} 1 & 2 & 1 \\ 0 & 0 & 0 \\ -1 & -2 & -1 \end{bmatrix} \quad \text{eq (30)}$$

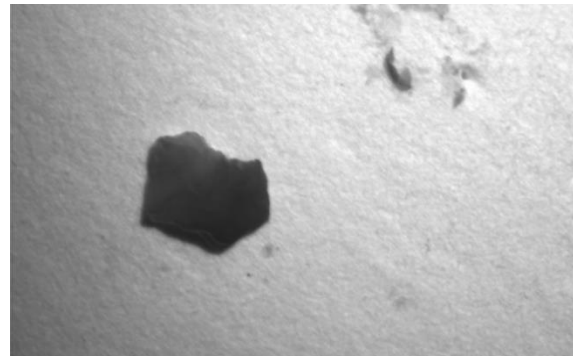
The transpose of this sobel filter is used to obtain the image  $I_y$  with the vertical edges. The magnitude of the gradient is obtained by equation 31. The resulting image with the edges is displayed in figure 15.c).

$$I_{edges} = \sqrt{I_x^2 + I_y^2} \quad \text{eq (31)}$$

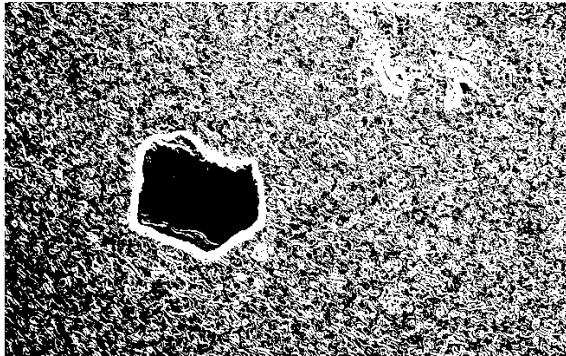




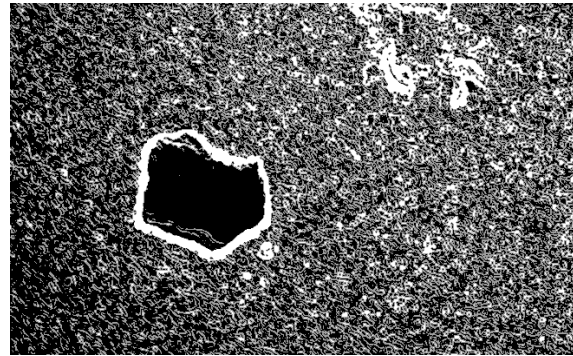
a)



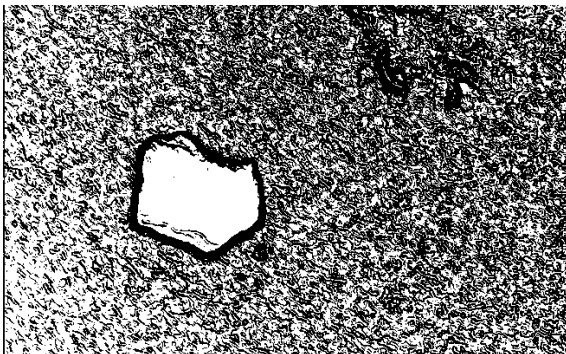
b)



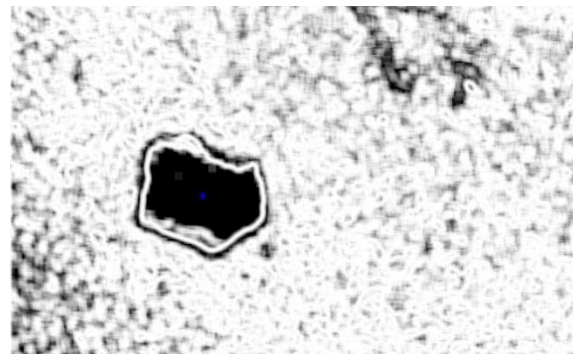
c)



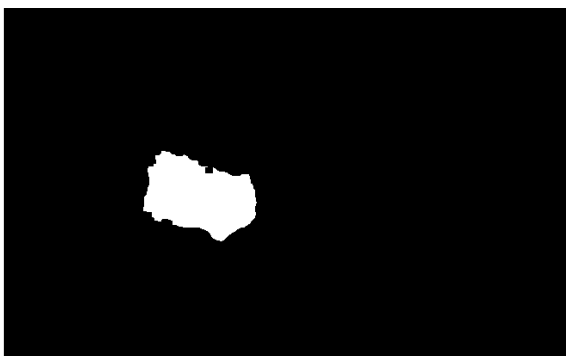
d)



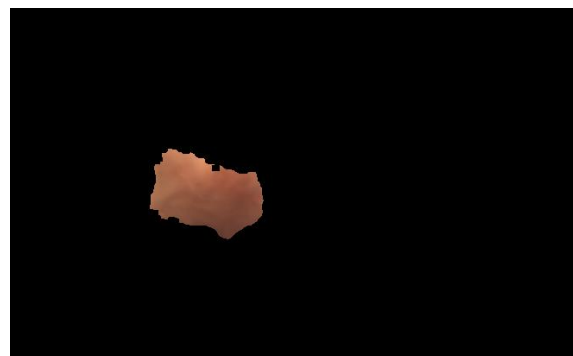
e)



f)



g)



h)

Figure 15. Segmentation of the stomach from mice. a) Original image b) monoband image centered at 520 nm c) result from a sobel filter d) opening on the image, e) threshold and inversion, f) entropy filter and identification of the centroid of the stomach, g) estimated mask of the stomach and h) segmented stomach.



The next step includes the morphological operator opening which is applied with a circular mask of 5x5 pixels in order to increase the edges as observed in figure 15.d). Then, the image is binarized so that any edge superior to a threshold of 0.01 is equalized to 1. Then, the image is inverted to obtain the stomach in white as displayed in figure 15.e).

At this point, we observe a clear contour of the stomach but unfortunately, this segmentation also included the shadow from the stomach on the tissue. In order to identify this area, we compute the entropy in a window of 9x9 pixels so that the shadow will appear as a soft white area under the contour from the mice clearly observed in figure 15.f). After that, the centroid from the mice is estimated and displayed as a blue spot. The coordinates of this centroid are used as a seed to a region growing algorithm to segment the stomach which mask is displayed in figure 15.g). Finally, the segmented mouse from the color image is displayed in figure 15.h) for reference.

After that, four areas of 6 mm diameter (5784 neighbor pixels in a diamond shape) were randomly extracted from the multispectral image, following the description in figure 12. A mean spectrum from each area is computed and used for the statistical analysis. This procedure was repeated 10 times obtaining homogeneous results at each iteration. In order to validate this conclusion, we take advantage of the statistical analysis Anova which returned a p value higher than 0.1, confirming that there is no statistical significant difference between the iterations. The aim of this procedure is to simulate the random acquisition performed with the spectrometer and therefore, facilitate the comparison of the two acquisition systems with the statistical tools.

### **3.4. Bacterium colonization and histopathological results**

The results from colonization of *H. pylori* are displayed in figure 16. The colonization is expressed in cfu/g (colony-forming unit per grams). The colonization was slightly reduced within time but finally stabilized which is an indicator of the infection of the bacterium in the tissue. Generally speaking we observe that the mice scarified at 7 and 12 months after inoculation had a similar concentration of the bacteria. In the particular case at 12 months the high variation in the bacterium indicates that the colonization in one mouse was higher than the other subjects. In any case, taking in consideration the concentration of the bacteria after 12 months post inoculation, it is clear that the stomachs had developed gastritis.

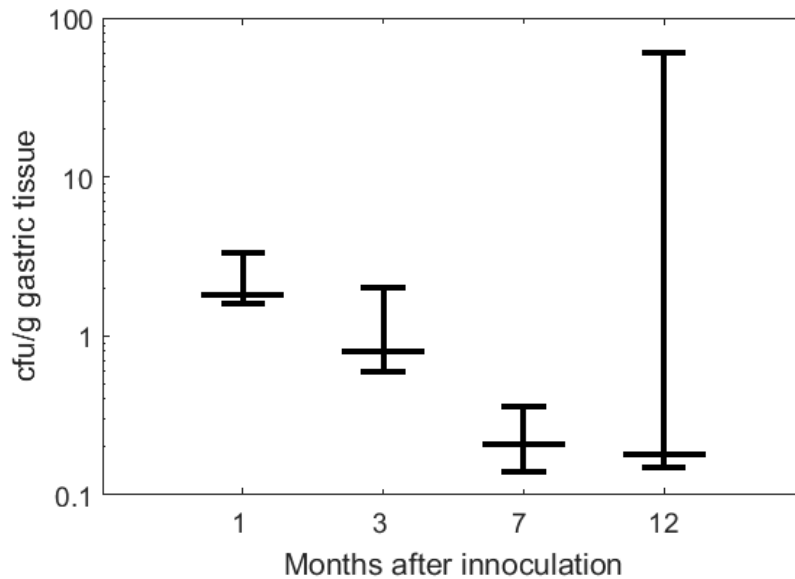


Figure 16. Colonization of the bacterium *H. pylori* in the stomach of mice, sacrificed in each acquisition campaign.

All the infected mice showed inflammatory cells infiltrates. The evolution of the disease is displayed in table 5 from precocious to a chronic inflammation. A mixed inflammatory infiltrates and glandular structures were identified by histological analysis at each acquisition campaign in the inoculated group. As expected, these modifications in the tissue were not observed in the control group. These gastritis modifications at microscopical level are the aim of this study. In particular, their identification based on the analysis of the reflectance will be discussed in the next section.

Table 5. Evolution of the inflammation of the gastric mucosa after infection by *H. pylori*.

Time after inoculation of <i>H. pylori</i>	Infiltration	Diagnosis
1 month	Discreet erythema	Precocious inflammation
3 months	Dense with polynuclear cells	Severe acute inflammation
7 months	lymphoplasmocytic	Mild chronic inflammation
12 months	lymphoplasmocytic	Chronic inflammation

### 3.5. Statistical analysis of the reflectance

This section is devoted to the analysis of the reflectance acquired from the tissue. In order to identify the wavelengths which are candidates for the differentiation of the pathology, we take advantage of statistical analysis. In this sense, we take in consideration that the samples are originated from two independent groups and that the reflectance is the quantitative response variable. In chapter 2 was detailed some of the statistical non parametric test that could deal with these constraints.

As a departing point, we assume that mice from the control group have normal mucosa so that they can be used as a reference to normalize the spectra from the inoculated mice between the different acquisition campaigns. This normalization is performed by using a ratio between the spectra from inoculated mice and the mean of the control group of the session. The advantage of this normalization is that it allows us to observe the trend of the data and a fair comparison between the different acquisition campaigns.

The statistical analysis is divided in two parts for each acquisition system. The first one is oriented to identify the wavelengths which display statistical significant differences. It includes a comparison between the two groups (inoculated and control group) at each acquisition campaign following an individual evaluation of each acquired wavelength. This analysis is performed by Wilcoxon-Mann-Whitney non-parametric test. This test is oriented to identify a difference in the medians as was explained in chapter 2 so that having the distribution functions  $G(x)$  and  $G(y)$  for the control and inoculated group respectively, we test the null hypothesis where both groups have the same distribution and the alternative hypothesis  $H1$  where a shift is included in the distribution ( $G(y) = G(x - \vartheta)$  for a  $\vartheta \neq 0$ ).

The second part of the analysis is oriented to verify that from the inoculated group, we can observe statistically significant variation of the reflectance in each acquisition campaign. For this purpose, an extension of the Wilcoxon-Mann-Whitney non-parametric test is Kruskal-Wallis which is applied on the data from the normalized inoculated mice, so that we test the null hypothesis where the distribution from the normalized inoculated data at each campaign is the same ( $\vartheta_{1\text{ month}} = \vartheta_{3\text{ months}} = \vartheta_{7\text{ months}} = \vartheta_{12\text{ months}}$ ) and the alternative  $H1$  where there is at least a pair  $\vartheta_i \neq \vartheta_j$ .

### 3.5.1. Analysis of the control group

In figure 17 are displayed the box plots of the raw spectra acquired with the spectrometer from the control group. The first point to highlight is the similitude on the measurements in each acquisition campaign, so that mice with normal mucosa display the same trends on the spectrum.

On the other hand, we observe from this figure variations in the amplitude of the spectrum between the different acquisition campaigns, even though the samples were collected from *H. pylori* free mice. This situation was expected because these changes could be related to the biological conditions such as diet, environmental temperature, month of the year, humidity, etc. Overall, it is important to highlight that we assume that these variations on the amplitude of the spectrum are related to the biological conditions and not to the infection and therefore, we expect that the inoculated mice will be affected by these biological conditions in the same proportion as the control group.

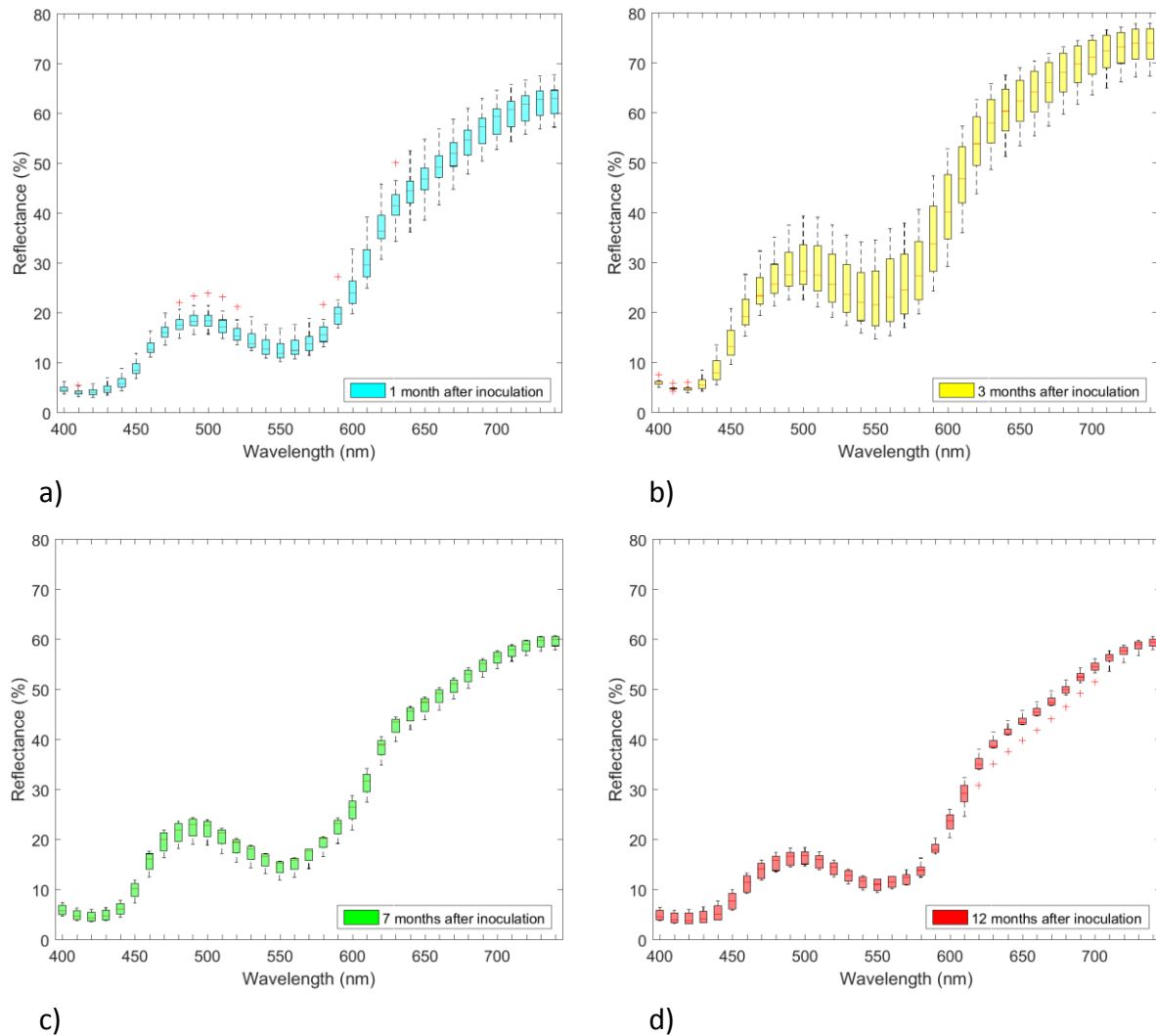


Figure 17. Box plots from the samples of the control group at a) 1 month, b) 3 months, c) 7 months and d) 12 months after inoculation.

In the case of the spectra acquired with the multispectral camera, it displayed a similar trend that the spectra acquired with the spectrometer. In figure 18 is displayed the spectra collected from the control group. Similar to the spectrometer, we first highlight the homogeneity on the collected spectrum at each acquisition campaign. The exception is the control group at 3 months post inoculation. In this acquisition campaign the acquired reflectance from the control group was observed homogeneous in the measurements from the same stomach but different between the subjects from the same acquisition campaign. This situation is mainly related to the illumination conditions which were not completely homogeneous between the stomachs, producing as a consequence the observed variation in the reflectance. Even though the acquired reflectance shows some differences in amplitude, the average behavior of the data is similar to the one acquired by the spectrometer. Under these circumstances, we decide to pursuit the study considering this variation of the illumination as part of the inherent noise of the signal. The next section is devoted to the analysis between the inoculated and control group.

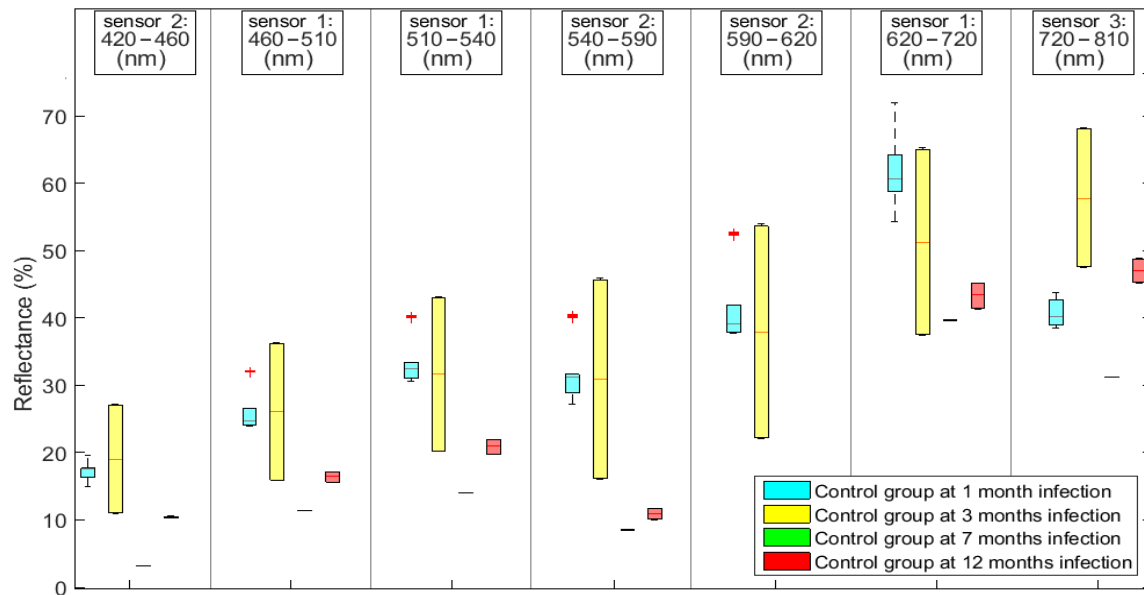


Figure 18. Box plot from the samples from the control group acquired with the multispectral camera.

### 3.5.2. Analysis between inoculated and control group

This analysis is oriented to identify the wavelengths which could be used for diagnosis of gastritis. In figure 19 is displayed the mean of the normalized spectrum from the inoculated group from each acquisition campaign. It also highlights the wavelengths which were statistically significant at each acquisition campaign resulted from Wilcoxon-Mann-Whitney non-parametric statistical test at a level of significance ( $p < 0.05$ ). In our case, these are the wavelengths which are candidates for the diagnosis that will be discussed in the following paragraphs.

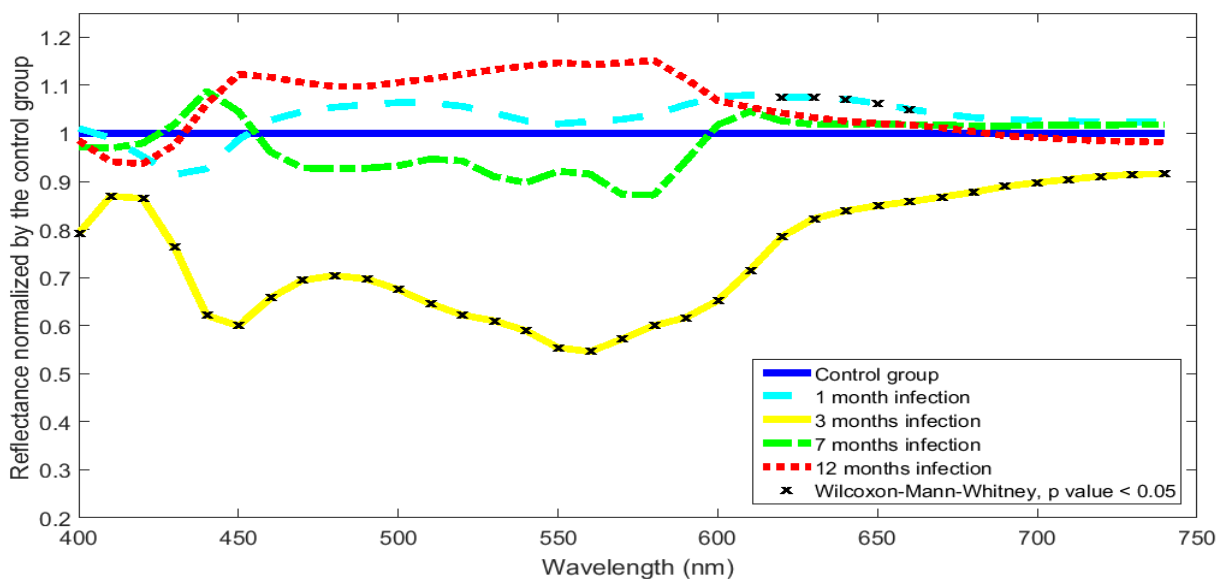


Figure 19. Normalized data from the spectrometer at each acquisition campaign. The statistical significant wavelengths retrieved from Wilcoxon-Mann-Whitney analysis are highlighted.

In the statistical analysis on the data acquired with the spectrometer we observe that the bands between 620 and 660 nm are statistically significant at 1 and 3 months after inoculation. The changes at these wavelengths could be originated on the blood oxygenation or on the variation in the size of the scatters as showed in the curves from the theoretical model of light tissue interaction detailed in chapter 2.

In the case of 3 months after inoculation, all the wavelengths were identified as significant with the spectrometer. This situation makes us consider the origin of these changes on the blood concentration which modifies the full spectrum as showed in the theoretical model of light tissue interaction from chapter 2. In this sense, this result is coherent because a change in the blood concentration is known to be related to an acute inflammation due to the increment on fluids, coagulation factors and inflammatory infiltrates [108].

In figure 20 are displayed the results of the normalization of inoculated mice with respect to the control group acquired with the multispectral camera and the significant wavelengths resulted from Wilcoxon-Mann-Whitney non-parametric test.

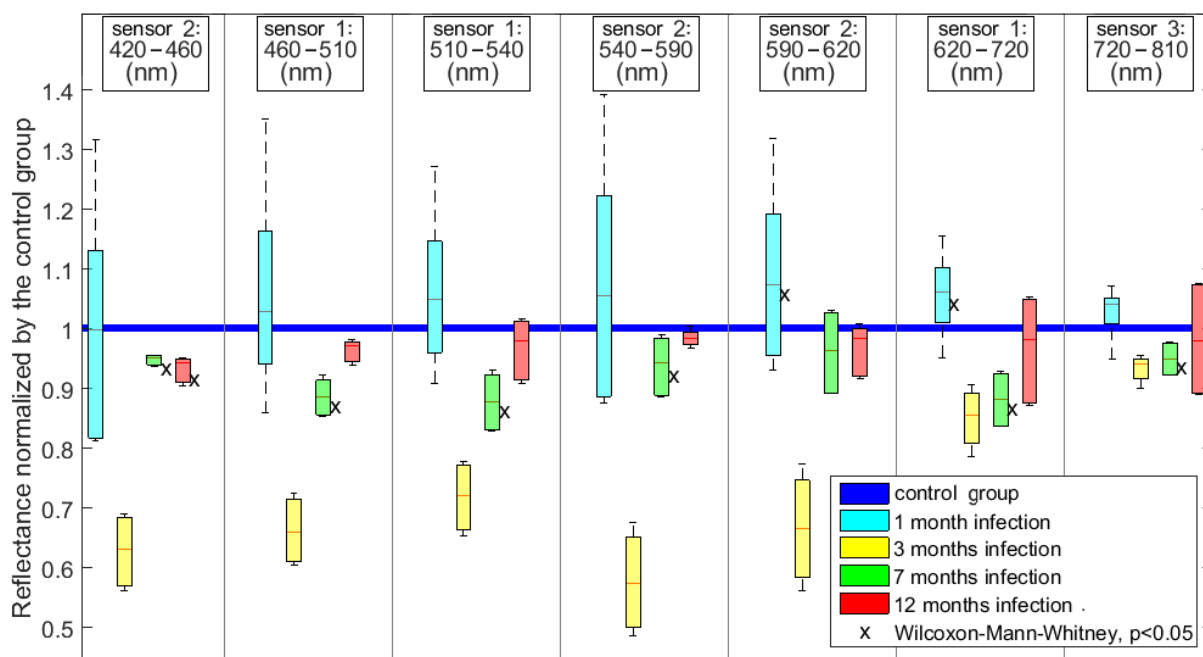


Figure 20. Normalized data from the multispectral camera and the results from the statistical analysis.

We first highlight that in general the data displays similar trends with both acquisition systems; only the acquisition campaign at 12 months after inoculation shows a different trend. There is a strong variability on the acquired data, which is expected considering its biological origin and the acquisition conditions. The red wavelengths are statistically significant in the first and seventh month after inoculation. In contrast with the data from the spectrometer, the infection at 3 months is not considered statistically significant even though there is a marked difference with respect to the control group. This situation was

expected due to the wide variation in the samples from the control group as previously described. As a consequence of this situation, we consider that the low signal to noise ratio makes more difficult the identification of the differences between the inoculated and the control group.

In the case of the acquisition campaign at 7 months post-inoculation almost all wavelengths were statistically significant from the multispectral camera. This situation makes us consider the cross talk between the channels from the multispectral camera since each measurement includes other wavelengths as can be observed in figure 13, in particular the first channel where an expected measurement between 420 and 460 nm will also include the wavelengths between 510 and 550 nm.

Another point to consider is the fact that ex vivo samples display different constant modifications [109]. In particular the blood concentration, a main feature that is typically reduced after dissection. Even though most of the blood remains after sacrifice, it could leak in random proportions during the preparation and acquisition of the reflectance. Additionally, the cells will die slowly due to a lack of oxygen and the mucosa will dry within time.

The results from the statistical analysis from the spectrometer and the multispectral camera allow us to consider some wavelengths that could be candidates for diagnosis of the gastritis. For this purpose, we take into account the sensibility of each channel from the multispectral camera. These wavelengths are displayed as a summary in table 6.

Table 6. Band of wavelengths which are candidates for diagnosis of the gastritis.

	<b>430 - 450 nm</b>	<b>470 – 590 nm</b>	<b>620 – 680 nm</b>
<b>Precocious inflammation</b>	Decrement of the reflectance	NS	Increment of the reflectance
<b>Severe acute inflammation</b>	Decrement of the reflectance	Decrement of the reflectance	Decrement of the reflectance
<b>Mild chronic inflammation</b>	Decrement of the reflectance	Decrement of the reflectance	Decrement of the reflectance
<b>Chronic inflammation</b>	Decrement of the reflectance	Increment of the reflectance	NS

NS: Not significant

Generally speaking the band of wavelengths between 430 to 450 nm and 470 to 590 nm could be related to an increase of the oxygen saturation during the development of gastritis. The changes in the band between 620 to 680 nm could be related to the oxygen saturation and the size of the scatters presented in the tissue.

### 3.5.3. Analysis between the acquisition campaigns

The second part of the analysis is based on Kruskal-Wallis to identify if the data between the acquisition campaigns have significant differences. This analysis is based on the reflectance from the inoculated mice which were normalized by the control group from their respective acquisition campaign. The results are displayed in table 7.

Table 7. Wavebands with significant differences between acquisition campaigns from the normalized inoculated data.

	Wavebands identified as statistical significant ( $p < 0.05$ )	Wavebands not identified as statistical significant ( $p \geq 0.05$ )
<b>Spectrometer</b>	400 – 410 nm 430 – 740 nm	420 nm
<b>Multispectral camera Flux Data</b>	420 – 810 nm	None

In the case of the spectrometer, we observe that only the waveband at 420 nm was not significant between the acquisition campaigns; all the others were statistical significant at  $p < 0.05$ . This particular situation indicates that the spectrum evolve differently during the development of the gastritis, the exception was the band at 420 nm, which had the same behavior in all the stages of the pathology, making it not relevant for diagnosis.

A similar procedure was followed for the case of the multispectral camera Flux Data. In this case all the wavebands were identified as statistically significant between the acquisition campaigns at  $p < 0.05$ . The waveband at 420 nm could not be identified as significant because the acquisition channel from the multispectral camera collects a wide spectrum which includes mainly wavebands identified as statistical significant.

Given these points and the non-significant variations between the samples at the same acquisition campaign, the interpretation of the analysis performed with Kruskal-Wallis is that there are different diagnosis between the acquisition campaigns for the inoculated mice and that this situation is observed with both acquisition systems. Additionally, this situation is confirmed with the diagnosis from the histological analysis.

The encouraging results from this study with the statistical analysis of the reflectance and the identification of wavelengths which are candidates for the diagnosis are considered as evidence that there are measured differences in the reflectance related to the development of gastritis. Therefore, a main outcome from this pilot study is the foundations to start a similar study with a larger group of mice.



### 3.6. Summary

Mice model of infection of *H. pylori* is a key element in the analysis of the development of gastritis. We oriented this study to the identification of potential wavelengths which could be used in the diagnosis of gastritis.

The mice were separated in two groups, the inoculated with *H. pylori* and the control group bacterium free. There were 4 acquisition campaigns at 1, 3, 7 and 12 months after inoculation where mice from both groups were sacrificed.

The reflectance from mice stomach was collected by two different acquisition systems. The first one was a spectrometer which allows collecting point measurements at high spectral resolution. The second one was a multispectral camera with high spatial resolution but low number of wavelengths available.

The study was based on the analysis of the reflectance by applying two non-parametric statistical tests. The first one is Wilcoxon-Mann-Whitney oriented to identify if there is a change in the reflectance between the group inoculated with *H. pylori* and the control group bacterium free. The second one is Kruskal-Wallis to identify changes in the normalized data from inoculated mice between acquisition campaigns.

The results from this study shows a significant variations in the mucosa measured at different stages of the development of the pathology between the two groups analyzed. The conclusion from these analyses shows that 3 bands of wavelengths are candidates for the diagnosis of gastritis. These bands are delimited to 430 to 450 nm, between 470 and 590 nm and between 620 and 680 nm and could be related to changes in the size of the scatters, blood concentration and increments in the oxygen saturation during the development of the pathology.

# Chapter 4

## Clinical study of gastritis

Following the previous chapter oriented to the development of gastritis in a mice model, this chapter turns on the clinical study of the reflectance and how it could help in the identification of gastritis in humans. For this purpose, a first multispectral acquisition prototype was developed in order to collect multispectral images from the stomach. We describe the equipment and the algorithms developed to process the multispectral images. In this sense, we focus on statistical analysis of the reflectance to show the changes in the spectrum between pathological and normal mucosa. These modifications will be discussed and we will emphasize the wavelengths which are candidates to improve their diagnosis.

### 4.1. Filter wheel based prototype for multispectral acquisition

This subsection deals with the first prototype used to acquire multispectral images and the processing of these images to extract the spectrum.

#### 4.1.1. Acquisition system

A general view of the first prototype developed for this doctoral work is shown in figure 21. White light is produced by a Xenon lamp of 175W which is typically used in gastroendoscopy. This light is filtered sequentially by one of six interference filters of 25mm diameter placed in a rotating filter wheel. The filtered light is transported by the illumination fibers of the gastroendoscope in order to be delivered at the stomach and used to illuminate the gastric tissue with a single waveband at a time. The RGB camera from the gastroendoscope acquires the image, which is transferred into the gastroendoscopic unit (Olympus Exera II). Finally a computer connected to the gastroendoscopic unit stores the images in a video sequence ( $640 \times 480$  pixels, 25 fps).

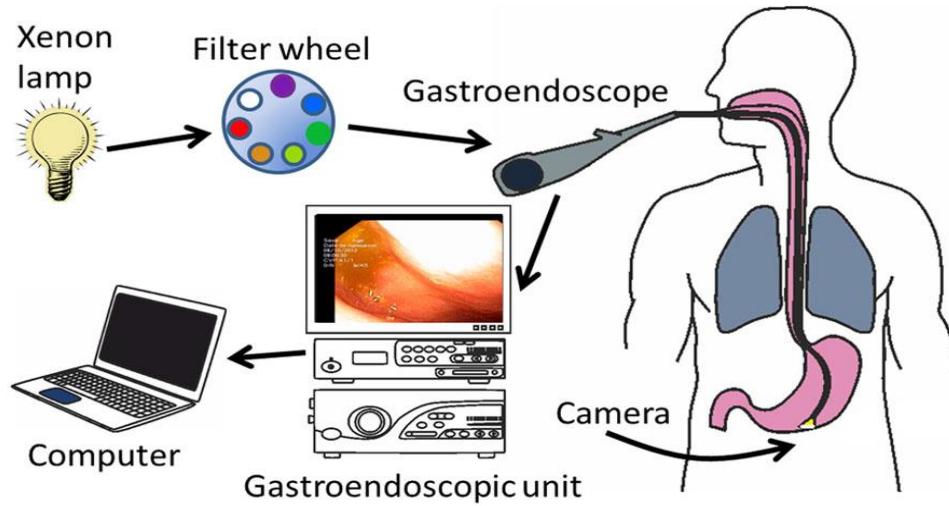


Figure 21. Block diagram of the first acquisition prototype based on a filter wheel.

The six interference filters used in the filter wheel have center wavelength of 440, 480, 520, 560, 600 and 640 nm with a full width at half maximum of 80 nm. These filters were selected in order to measure the visible spectrum equitably, taking into consideration the spectral sensitivity of the camera from the gastroendoscope, which is limited for red wavelengths. Additionally, the measurements of the absorption peaks of hemoglobin were also considered, in particular, the first peak at 420 nm and those occurring between 530 and 650 nm. This configuration is advantageous for a fast implementation since only the illumination is modified which allows to be used with any commercial endoscope. An example of the acquired images at different wavebands is displayed in figure 22.

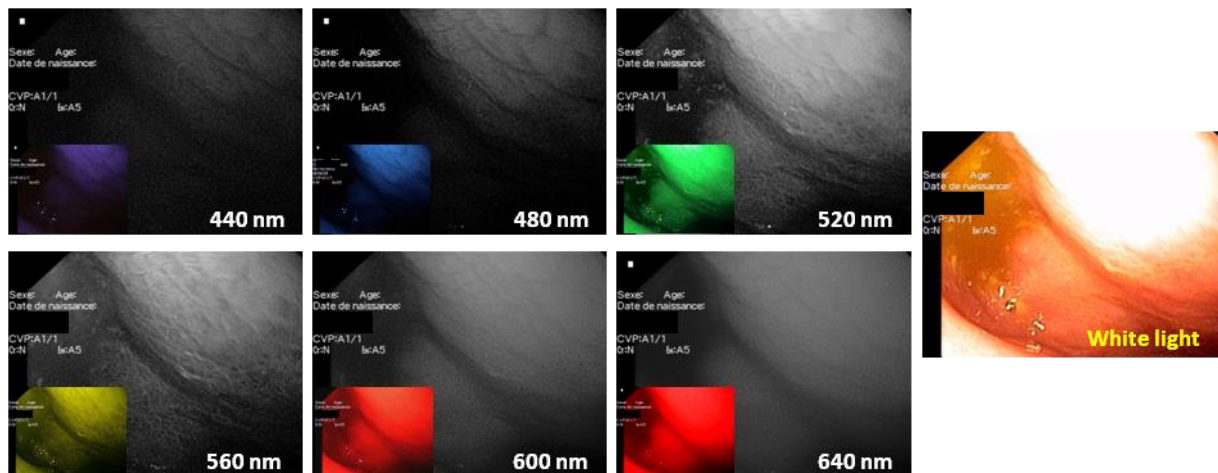


Figure 22. Images acquired from gastric tissue at different wavebands from the prototype based on a filter wheel.

The video containing the multispectral images was deinterlaced using Yadif algorithm [110]. After that, the image from each waveband was extracted semiautomatically, taking in consideration the frame rate, the illumination time of each filter and their transition

time. The resulting acquisition time is approximately one second for each multispectral image. This acquisition time is not negligible, since involuntary movements of the gastric tissue introduce motion artifacts. With this in mind registration was performed between the monoband images in order to reduce the impact of the tissue deformation and shifting.

#### **4.1.2. Registration of multispectral images**

The registration of images acquired during gastroendoscopy includes some constraints due to the nature and conditions of acquisition. For instance, due to the high homogeneity of gastric tissue, the moist environment and the use of different wavebands for illumination, traditional registration methods using salient points fail to register the images. In the present doctoral work, CLAHE algorithm [111] was first applied as an image contrast enhancement to improve the quality of the image. This algorithm is based on Adaptive Histogram Equalization algorithm where the image is divided in 64 regions or tiles from which a histogram is calculated in each of them and transformed into a uniform distribution. The maximum number of elements at each gray level is limited or clipped in order to avoid noise enhancement, specifically from homogeneous areas. Finally bilinear interpolation is applied to neighboring tiles to create the final image [112]–[114].

After performing contrast enhancement on each monoband image, hierarchical motion-based estimation [115] was used for registration. In this superresolution approach, 5 levels of Gaussian pyramids are calculated, the size of the image at each level is half the size of the previous one. These images are then used to estimate the motion according to an affine model [54]. Starting from the smaller image, the affine transformation is calculated and transferred between the different levels of the pyramid, where it is used as initial estimation and refined by including the local information, aimed to obtain at the end the best matching.

Taking in consideration the sequential acquisition, the first and the last monoband images acquired have the longer elapsed time and therefore, more difficult to register. Under these circumstances, the image at 560 nm was used as a reference for the registration, since it is in the middle of the sequence, having as an advantage that the elapsed time is only half compared to the extreme images of the sequence. The computed transformations are then applied to the original raw multispectral images. In figure 23 is displayed a simulated white light image from the multispectral image. We highlight the improvements in the sharpness of the computed image before and after registration.

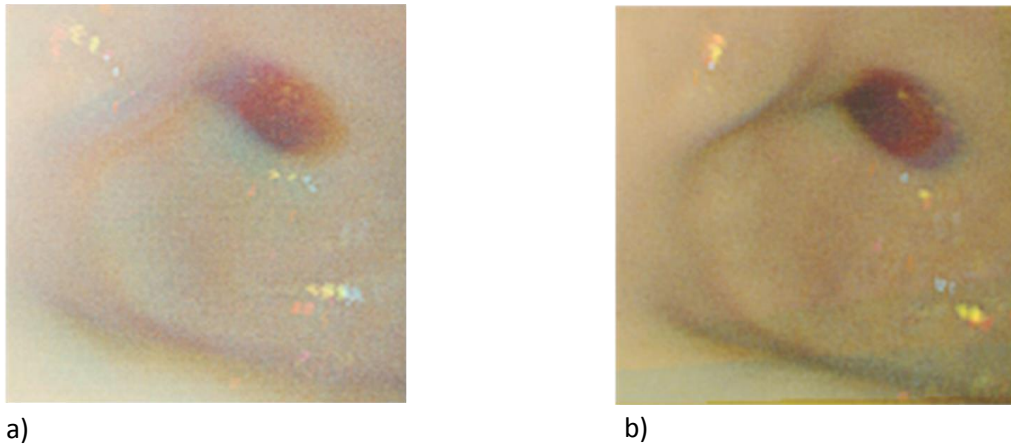


Figure 23. Simulation of white light image calculated from a) overlapping the raw monoband images and b) registered monoband image.

#### 4.1.3. Processing of multispectral images

The acquired multispectral images could show areas of tissue such as the pylorus, tissue folds and artifacts including gastric bubbles and specularities which are not interesting to analyze. Thus, aimed to extract the spectrums for the analysis of the pathology, a region of interest was selected manually by the user to remove these artifacts. Only the specular areas were removed automatically by thresholding, which was set to a value of 240 / 255. In figure 24 is showed the result of this procedure.

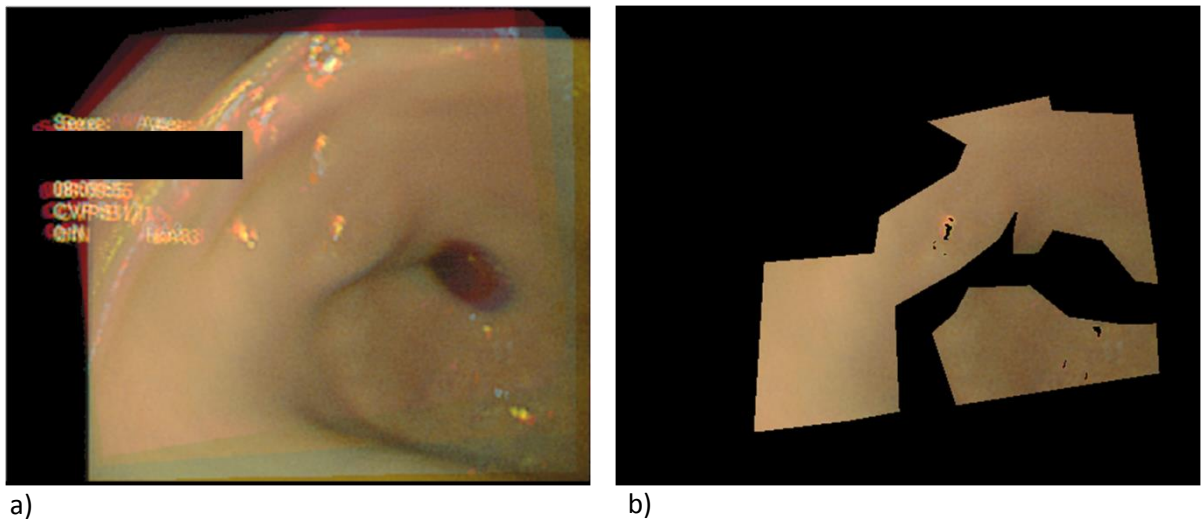


Figure 24. a) Registered image and b) selected region of interest from the image.

From the region of interest, 20 patches of size 5 x 5 empirically chosen were randomly selected and averaged in order to obtain a single spectrum from the multispectral image. Then, the spectrum was normalized using L1-normalization according to equation 16 from the chapter 2. This procedure was repeated 10 times per multispectral image to include the possible variations of the spectrum in the multispectral image. The next section is devoted to the analysis of the extracted spectra.

## 4.2. Database

This subsection is oriented to the description of the subjects and the multispectral images that were collected.

### 4.2.1. Subjects

The population for this clinical study included patients referred to endoscopic unit of the hospital Ambroise Paré, Boulogne-Billancourt, France, during the period of one year between October 2012 and November 2013. These patients provided informed consent and were scheduled for gastroendoscopy under general anesthesia with the indicator for biopsy collection from the antrum and corpus. These biopsies were placed in 10% formalin and embedded in paraffin in order to cut transversal sections of 4  $\mu$ m thickness. These samples were stained by HES for routinely histological analysis. Additionally, PCR (Polymerase Chain Reaction) and immunochemistry using PFLEX Polyclonal Rabbit antibody were performed to grade the infection from *H. pylori* and the gastric pathology according to the recommendations from the Updated Sydney System. The histopathological diagnosis was performed by a senior pathologist.

The characteristics of the patients are displayed in table 8. Most of the patients displayed normal mucosa and therefore are placed in the control group. The Standard Error of the Mean (SEM) estimates the discrepancy on the ages of the patients. There were no significant differences in gender or age for this study between the groups ( $p > 0.1$ ).

Table 8. Clinical features from the patients.

	<b>Number of patients</b>	<b>Age (+/-SEM)</b>	<b>Gender ratio (H:F)</b>
<b>Gastritis group</b>	8	54.87 (5.77)	3:1
<b>Control group</b>	17	59.64 (2.61)	0,7:1

### 4.2.2. Collected multispectral images

Multispectral images from the antrum were collected from 25 patients who were eligible if no visible lesions were observed during gastroendoscopy whereas histological analysis found one of two diagnoses: active gastritis or normal mucosa.

In this study, the waveband at 480 nm was removed because the filter was broken in the middle of the acquisition campaign. Under these circumstances, the data at this waveband was erratic and therefore, not suitable for this study.

Taking into consideration that the source of light was constant, the images acquired when the gastroendoscope was far away from the gastric tissue were considerably dark, producing a low signal to noise ratio. In consequence, these multispectral images were not taken in consideration. Additionally, since the stomach could move during the acquisition, we used the multispectral images where the images at each waveband were sharp and display low movements between them so that they were suitable to be registered according to the procedure described in the previous section.

The mean number of studied images for each clinical condition is presented in table 9. There was no significant statistical difference between the two groups in terms of mean number of multispectral images ( $p > 0.1$ ).

Table 9. Multispectral images from the two clinical groups.

<b>Diagnosis</b>	<b>Gastritis group (N=8)</b>	<b>Control group (N=17)</b>
<b>Mean number of multispectral images per patient (+/- SEM)</b>	4.63 (1.13)	5.29 (0.92)

Granted that there is no bias in the database related to the number of patients, age, gender or mean number of multispectral images, the next step is the statistical analysis of gastritis which will be addressed in the following section.

### 4.3. Analysis of gastritis

This subsection deals with the clinical study of inflammatory gastritis due to infection by *H. pylori*. The study is divided in a qualitative and a quantitative analysis between patients diagnosed with gastritis and those diagnosed with normal mucosa. This analysis is oriented to identify the changes in the spectrum due to the development of the gastritis.

#### 4.3.1. Qualitative analysis of multispectral images

The multispectral images were observed by senior endoscopist Dominique LAMARQUE. There were no visible differences between images under white light from control or gastric patients as illustrated in figure 25 (a-b). The band at 560 nm highlighted areas with a wooly dark weft appearance on one patient with active inflammation as presented in figure 25d. This showed evidence of texture modification which is not visible under white light. In contrast, the images from subjects in the control group showed a smooth uniform mucosal surface as shown in figure 25 c.

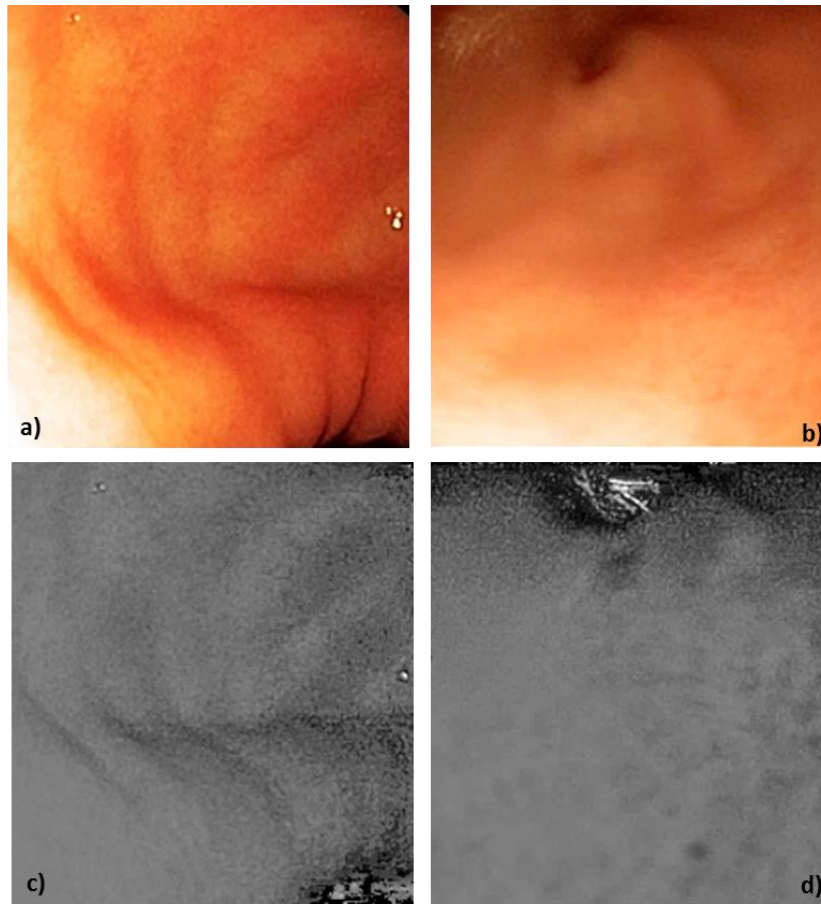


Figure 25. Images under white light from control group (a) and gastritis (b). In the band at 560 nm, we observe that the tissue from the control group (c) is smooth, in comparison with the gastritis one (d) which presents black spots and a non-uniform surface. We observe that the band at 560 nm highlights areas with a wooly dark weft appearance on the patients with active inflammation as is presented in figure (d).

#### 4.3.2. Statistical analysis

The patients were grouped under one of two clinical conditions based on the gastroendoscopic and histological results: control group or pathological group (active gastritis). The control group presented few mononuclear cells in the mucosa and no *H. pylori* infection. On the other hand, the pathological group showed positive *H. pylori* infection, as assessed by immunohistochemistry or by specific PCR and inflammatory infiltrates, including mononuclear and polynuclear cells.

We computed a reference spectrum for the normalized data of the control group, as the mean response at each captured waveband. Later on, each patient from the gastritis group was compared to the control group in order to measure the percentage of variation. In order to quantify the differences between the normalized spectra from the two groups, we use ANOVA statistical test to identify if there is a significant statistical difference between them. Additionally, this analysis allows us to identify the wavebands which are candidates to be used for diagnosis.



The samples from the patient with a healthy diagnosis are displayed in figure 26. General speaking we observe a homogeneous distribution.

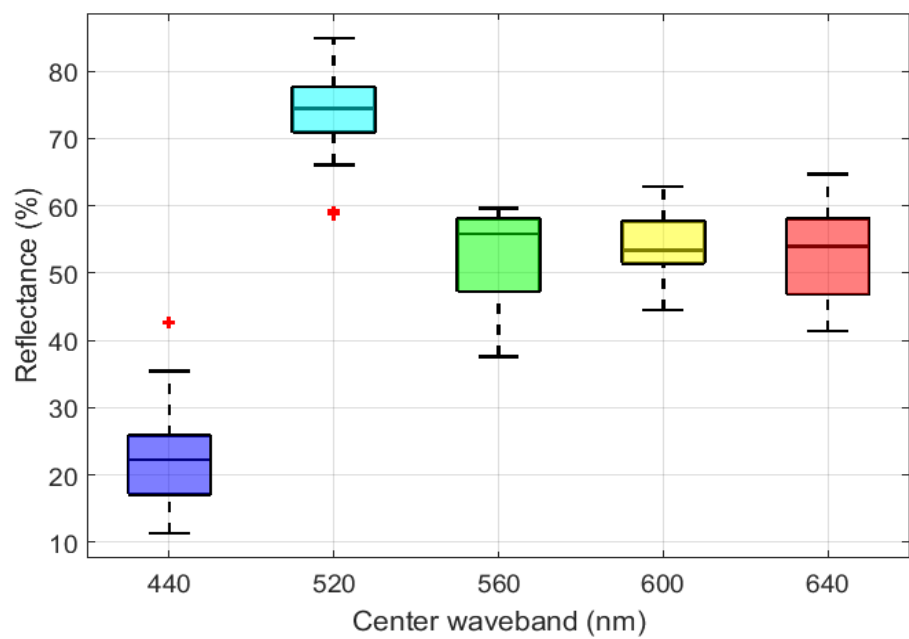


Figure 26. Distribution of samples with a healthy diagnosis.

The analysis of the spectra from pathological patients is shown in figure 27. We observed that the bands at 560 nm, 600 nm and 640 nm have statistical significance in order to identify the gastritis. In particular, the band at 560 nm had the minimum p-value among all the collected wavebands.

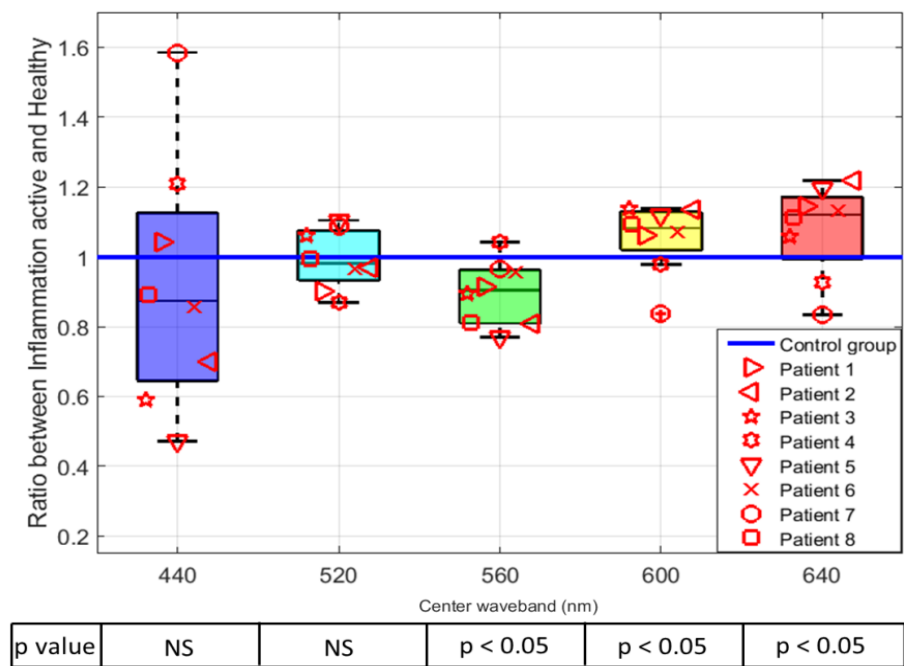


Figure 27. Ratio of variation in the spectrum from patients with active inflammation compared with the reference spectrum from control group.

The waveband of 560 nm showed a significant decrement of the reflected light with respect to the reference computed from the control group. On the other hand, we clearly observed a significant increment of the reflected light presented in the wavebands of 600 nm and 640 nm. These results are similar to what was observed in the mice model as can be seen in the chapter 3, so that the wavebands above 560 nm are identified as significant in both analyses. However, the red wavelengths showed an increment of reflectance in humans whereas in mice was observed a decrement of reflectance. The band at 440 nm displayed a decrement in the reflectance in both cases, but, it was not identified statistical significant for human diagnosis. The band at 520 nm was important for diagnosis in the mice, but it is not the case for humans. These new findings lead us to reduce the wavelengths which are candidates for the diagnosis of the gastritis, on which future studies could be based, in particular focusing on wavelengths above 540 nm.

We would expect the blood concentration as a main feature involved in the differentiation of the gastritis. This feature is mainly based on the amplitude of the spectrum as discussed in chapter 2, which measurement requires an acquisition of the reflectance under controlled conditions with a strictly constant distance and angle between the probe and the tissue. Unfortunately, these conditions cannot be achieved with this acquisition system.

Taking special attention to the wavelengths above 540 nm, we first consider the waveband at 560 nm, which could be related to the absorption peak of hemoglobin as was discussed in chapter 2 and 3. In particular, this waveband could be correlated to microvessels density, which is identified in intramucosal gastric carcinoma [116], [117].

We have no such clear explanation for the reflectance changes observed at the bands at 600 nm and 640 nm, but we have some hypotheses. During gastritis, the inflammatory cells such as neutrophils are recruited in the stroma. It could be evoked that as part of the defense mechanism of the cells the orientation and concentration of heavy proteins could be different and may also contribute to the modifications of the reflectance. Under this situation, we consider two cases; the first one is the laminin, a protein concentrated in the cells which main activities are related to repair the cells. The second case is the collagen network produced by the fibroblasts, which are also involved in tissue repair [118]–[120].

The density of inflammatory infiltration and edema are other hypotheses. It may be the case that these mechanisms of defense play an important role in the increase of reflectance due to the rearrangement of the cytoskeleton and the storage of water and other substances, included but not limited to a higher presence of oxyhemoglobin, whose reflectance is higher between 600 and 700 nm in comparison with deoxy-hemoglobin [121] as was observed in chapter 2.

Even though the results from this preliminary study are promising, the small sample of patients is considered as a limitation. Therefore, a comparative study on a large scale is

required for future studies. Since the gastritis is only one stage in the cascade of cancer development, the next analysis is oriented to the identification of precancerous lesions.

#### **4.4. Summary**

In the cascade of cancer development, gastritis originated in an infection by *H. pylori* is considered as an early stage which could evolve into other types of lesions if the long term infection is not treated.

In the tissue diagnosed as gastritis, the mechanism of defense and repair from the cells are activated, producing changes in the reflectance. In order to study these small changes between gastritis and normal mucosa we presented a first acquisition prototype based on a filter wheel which helped us to collect the spectra of gastric mucosa from patients diagnosed with two different pathologies: normal mucosa and gastritis.

The analysis of the collected spectra includes a qualitative and quantitative analyses to identify the changes in the tissue between pathological and normal mucosa. In this sense, we observe from the qualitative analysis wooly patches in the waveband at 560 nm from some patients diagnosed with gastritis. In contrast, none of the patients with normal mucosa displayed this feature.

The quantitative analysis highlighted some wavebands which are candidates to the identification of the gastritis. The results are consistent to what was observed in the mice model discussed in chapter 3. In particular, we observe that the bands above 540 nm are strong candidates for diagnosis. Relating these results with the model of light tissue interaction, we could consider two main features for diagnosis with this acquisition prototype: oxygen saturation and size of the scatters.

# Chapter 5

## Clinical studies on precancerous lesions

This chapter is devoted to two clinical studies of precancerous lesions in the stomach. The chapter is divided in two parts, according to the acquisition system used to acquire the reflectance of gastric tissues. The first clinical study is based on the collected data from the prototype based on a filter wheel, which was described in chapter 4. This prototype has some limitations, mainly on the acquisition time and the range of wavelengths to capture so that we develop a second prototype to overcome these limitations. Therefore the second clinical study is based on the collected data from the system GEMS (Gastro Endoscope MultiSpectral) which takes advantage of a multispectral camera Flux Data. Details about the system will be described in the following sections.

In the cascade of cancer development the precancerous lesions are diagnosed mainly from a not treated chronic gastritis by *H. pylori*. This infection leads to modifications in the tissue as was described in chapter 1 and later on into precancerous lesions. For these clinical studies, we included patients diagnosed with precancerous lesions, containing atrophy and intestinal metaplasia. Dysplasia was also considered but there were no patients with this diagnosis in our database.

In the analysis of the reflectance we perform a statistical analysis on the samples acquired from patients with precancerous conditions and those with healthy mucosa. We additionally implement machine learning techniques to identify the multispectral images collected from precancerous conditions.

### 5.1. Differentiation of precancerous lesions from the prototype based on a filter wheel

This subsection deals with the clinical study based on the reflectance spectrum acquired from the prototype based on a filter wheel which was described in chapter 4. It is important to mention that the preprocessing steps described in the same chapter are also applicable for this study, so that we will use a single normalized spectrum from each multispectral image. The normalization of the spectrum is L1-normalization as described in chapter 2.

### 5.1.1. Database

In this subsection are described the subjects and the multispectral images that were collected during gastroendoscopy.

#### 5.1.1.1. Subjects

Similar to the study of gastritis from chapter 4, the population for this clinical study included patients referred to endoscopic unit of the hospital Ambroise Paré, Boulogne-Billancourt, France, during the period of one year between October 2012 and November 2013. The characteristic of these patients is that they were scheduled for gastroendoscopy under general anesthesia with the indicator for collection of biopsies from antrum and corpus and that these patients showed no evidence of visible lesions during gastroendoscopy. The biopsies were histologically analyzed for the diagnosis of the patient.

The characteristics of the 17 patients are displayed in table 10. Most of the patients were diagnosed with healthy mucosa and therefore are placed in the control group. The results showed that 12 patients were diagnosed with healthy mucosa; 5 patients displayed precancerous lesions in their histological samples. It is also included the SEM to estimate the discrepancy on the ages of the patients. There were no significant differences in gender or age for this study between the two groups ( $p > 0.1$ ).

Table 10. Clinical features from the patients.

	<b>Number of patients</b>	<b>Age (+/-SEM)</b>	<b>Gender ratio (H:F)</b>
<b>Group with precancerous lesions</b>	5	68.6 (14.87)	3:2
<b>Control group</b>	12	64.5 (11.36)	1:1

#### 5.1.1.2. Collected multispectral images

From the 17 patients we use in total 102 multispectral images for this study, 74 correspond to normal mucosa and 28 to precancerous mucosa. Since the power of the source of light was constant, the observed tissue in the multispectral images could be overexposed or underexposed, depending if the gastroendoscope was close or far to the gastric tissue. In this sense, the low signal to noise ratio from the image makes them not suitable for this study. Additionally, involuntary movements of the gastric tissue could arrive during the

acquisition of the multispectral image. We use multispectral images where the images at each waveband display low movements between them so that they could be registered following the procedure described in chapter 4.

The mean number of studied images for each clinical condition is presented in table 11. There was no significant statistical difference between the two groups in terms of mean number of multispectral images for each patient ( $p > 0.05$ ).

Table 11. Multispectral images from the two clinical groups.

Diagnosis	Group with precancerous lesions (N=12)	Control group (N=5)
Mean number of multispectral images per patient (+/- SEM)	6.16 (3.38)	4.35 2.39)

### 5.1.2. Statistical analysis

For this study, the patients were grouped under one of two clinical conditions based on the gastroendoscopic and histological results: control group or group with precancerous lesions. Similar to the analysis performed on the gastritis, a reference spectrum from the control group is computed as the mean measured response from each waveband. This average spectrum was used as a reference to measure the percentage of variation of the group with precancerous lesions. We observe in figure 28 the box plot of samples from the patients with a healthy diagnosis.

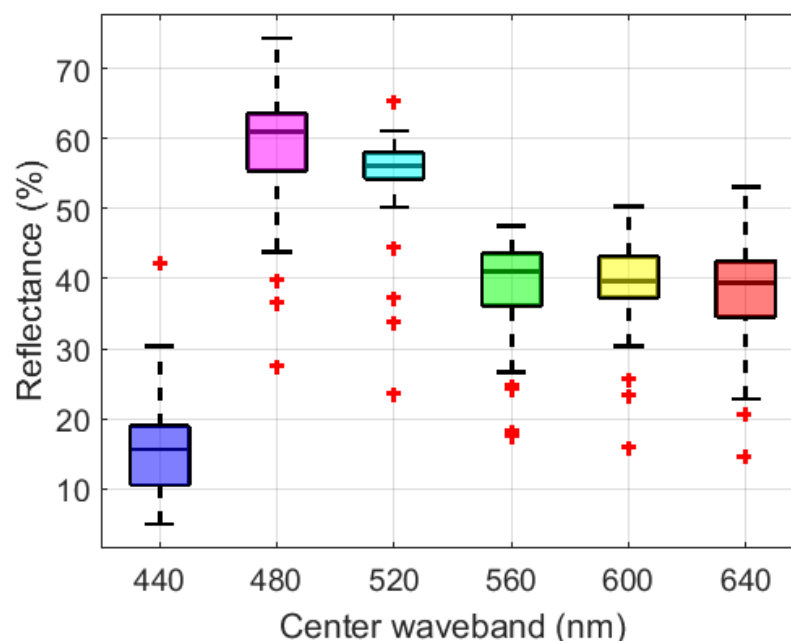


Figure 28. Box plot of samples from the control group having a healthy profile.

Taking in consideration the trends of the data, we immediately highlight the strong similitude with the control group discussed in chapter 4 and the observed homogeneous distribution with few outliers highlighted as a red cross.

The ANOVA statistical test was used to identify the statistical difference between the two groups. The results are displayed in figure 29. In this analysis we observe that only the wavebands at 480 and 520 nm were identified as significant for the differentiation of precancerous lesions. The patients with precancerous lesions showed an increment in the reflectance with respect to the reference spectrum of the control group. We must highlight that the band at 520 showed the minimum p-value.

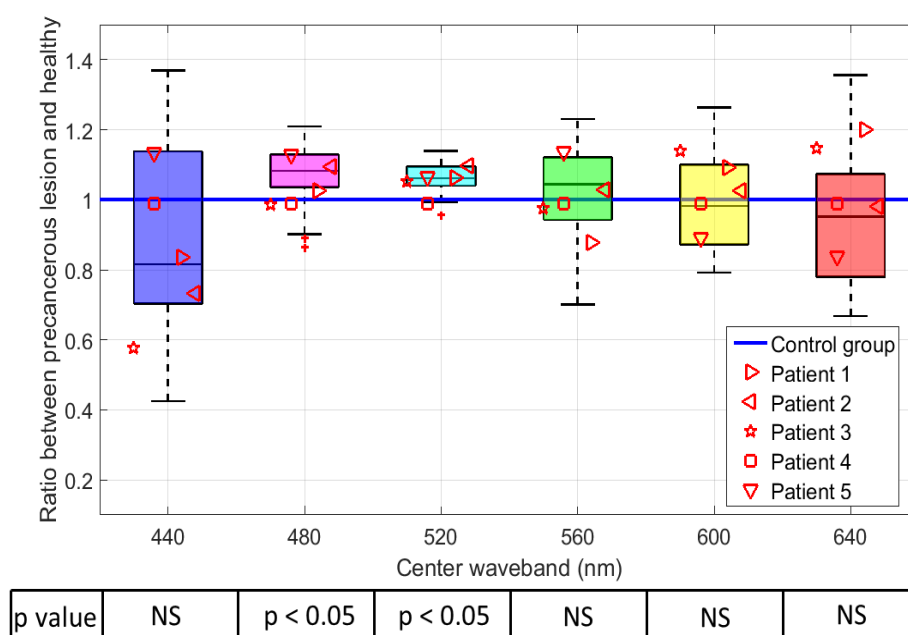


Figure 29. Ratio of variation in the spectrum from patients with precancerous lesions compared with the spectrum from the control group.

The wavelengths between 460 nm and 540 nm could be related to changes in the concentration of oxygen saturation as described in chapter 2. Additionally, the oxygen saturation could also be related to modifications in the bands above 600 nm. However, these wavebands were not identified as significant in this study. We have no clear explanation of this situation, but we consider that it could be related to the contributions on the spectrum from fibrous tissues. These fibrous tissues are associated with variations in the size of the scatters. In order to validate this hypothesis further studies are required, collecting the spectrum below 400 nm and above 600 nm, taking in consideration that above 700 nm the water content starts to be measured.

Another point to consider is that during the development of precancerous lesions, the space previously occupied by glands is replaced by fibrous tissues. In this sense, we expected significant modifications on the spectrum above 600 nm. However, this situation

was not identified; we consider that the acquisition system is not suitable to measure this small contribution to the spectrum. Further study is required including wavelengths below 400 nm and above 700 nm.

Another key point to consider is the similitude in the behavior of the reflectance with respect to the one acquired with the spectrometer in the mice model at 12 months after infection from chapter 3. In particular, we pay attention to the behavior of between 450 and 580 nm where it is observed an agreement in the increment of the reflectance. This situation makes us consider a link in the general behavior of the spectrum due to the development of malignancies in gastric tissues.

Based on these discoveries, the next step is oriented to differentiate precancerous tissues from our database by applying techniques of classification.

### **5.1.3. Classification of multispectral images with precancerous lesions.**

This subsection is oriented to describe a methodology to process the collected spectrum in order to differentiate between two clinical conditions: precancerous lesions and healthy mucosa.

The procedure selected to differentiate the tissue follows a computation of statistical features from the normalized spectrum. Then these features are ranked according to their discriminative power to differentiate between precancerous and healthy gastric tissues. After that a supervised approach of classification is applied to differentiate pathological tissues, including an evaluation of the performance of the classification in our database.

#### **5.1.3.1. Balance of the database for classification tasks**

In a classification task, it is known that classifiers could display a low performance when the database is imbalanced [122]. The reason is that the generation of classification rules leads to generalization of a single rule where all the samples are labeled with the same class. For instance, having 10% of samples from one class and 90% of samples from the other class, the learning algorithm could generalize to label all the samples as the second class and achieve 90% accuracy.

A popular approach for this issue is to balance the database so that both classes have the same number of samples. This can be done by oversampling the class with the minor number of samples.

In our case, the construction of the database follows a sampling procedure where 20 patches of 5 x 5 pixels are extracted and averaged to obtain a single spectrum from each



multispectral image, as was described in chapter 4. In the resulting database the control group have more multispectral images than the precancerous group.

In order to balance the database, we repeat this sampling procedure without replacement so that we obtain the same number of spectra for both clinical conditions. It is important to highlight that this situation is not an issue when using non parametric statistical test, which some of them are used in this doctoral work.

With a balanced database, the next step is the extraction of features from the spectrum.

### 5.1.3.2. Extraction of features

This step is oriented to obtain projections of the spectrum which can describe in a full or partial way the spectrum. For this purpose we assume that the spectrum follows a probability distribution which allows us to compute statistical features from it. In table 12 is displayed the list of features used for this doctoral work, which includes the features mentioned in chapter 2 and the normalized intensities from the collected wavebands. The ranking of the features will be explained in the next section.

Table 12. Ordered list of features.

Rank	Feature
1	Mean of absolute deviation
2	Mean deviation about median
3	Standard deviation
4	Median of absolute deviation
5	Variance
6	Waveband at 520 nm
7	Entropy
8	Waveband at 480 nm
9	Kurtosis
10	Waveband at 440 nm
11	Waveband at 640 nm
12	Waveband at 560 nm
13	Skewness
14	Waveband at 600 nm

### 5.1.3.3. Feature ranking

Between the different approaches to rank the features, we chose a filter approach to obtain a ranking according to their discriminative information that will not depend on the classifier. The metric used is the pooled variance t-test described in chapter 2, from which

the  $t$  value acts as a measurement of the discriminative potential of the features to differentiate the pathology. In figure 30 is displayed the measured  $t$  value for the features, following the ranking of table 12. From this ranking we must highlight that the statistical features display a higher rank than the single elements of the spectrum and therefore, they are considered as strong candidates to differentiate the precancerous lesions. Additionally, the two elements of the spectrum which appears top ranked are precisely those identified as significant from the statistical analysis previously described in this chapter namely 480 nm and 520 nm.

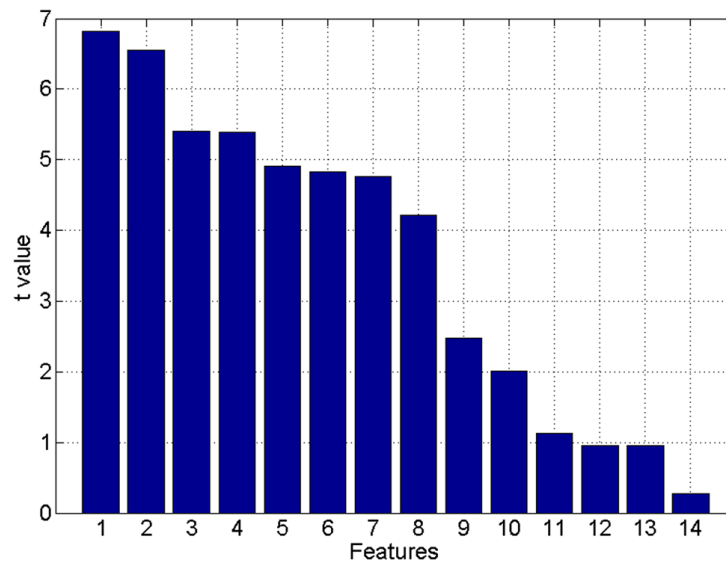


Figure 30. Measurement of the discriminative potential of the ranked features from table 12 by using pooled variance  $t$  test.

#### 5.1.3.4. Classification

In this doctoral work we apply three common supervised approaches to estimate the separation rules between healthy and precancerous tissues. These three methods are K-nn, SVM and NN which were described in detail in chapter 2.

Each of these techniques follows a step of training in order to learn the classes and a testing step on unknown data which is data that was not used for the training. In particular, this is a key point in the evaluation of the classifiers since the samples from the same patient display a strong correlation between them, so that the training and testing should not have samples from the same patient. Under these circumstances, we use LOPOCV previously described in chapter 2 to use all the samples from one patient at a time as unknown data and the remaining of the database is used for training the classifiers.

In order to avoid a bias, the ranking and classification should be performed in each iteration of the cross validation. Therefore, it is obvious that at each iteration the section of the database used for training contains always a different combination of the patients (total of patients – 1). Under these circumstances, a slightly different ranking of features is

obtained for each iteration. Then, we must highlight that the resulting position of the features is strongly similar in all the iterations so that a majority vote is implemented to obtain the general ranking of features, as displayed in table 12.

Besides the cross validation, the classifiers are trained and tested iteratively with an incremental number of features, starting from the top ranked and adding the next top ranked feature in each iteration so that in the last iteration all the features are used for the classification. The performance of the classification is quantitatively evaluated based on accuracy, sensitivity and specificity.

### 5.1.3.5. Results of the classification

In figure 31 we can observe the performance of the classifiers with a different number of features, increased progressively by order of rank. Each classifier reaches a maximum performance with a different number of features. This situation was expected since the features are ranked according to their discriminative information, so that when features with low discriminative potential are included, we identify a decrease on the performance of the classification.

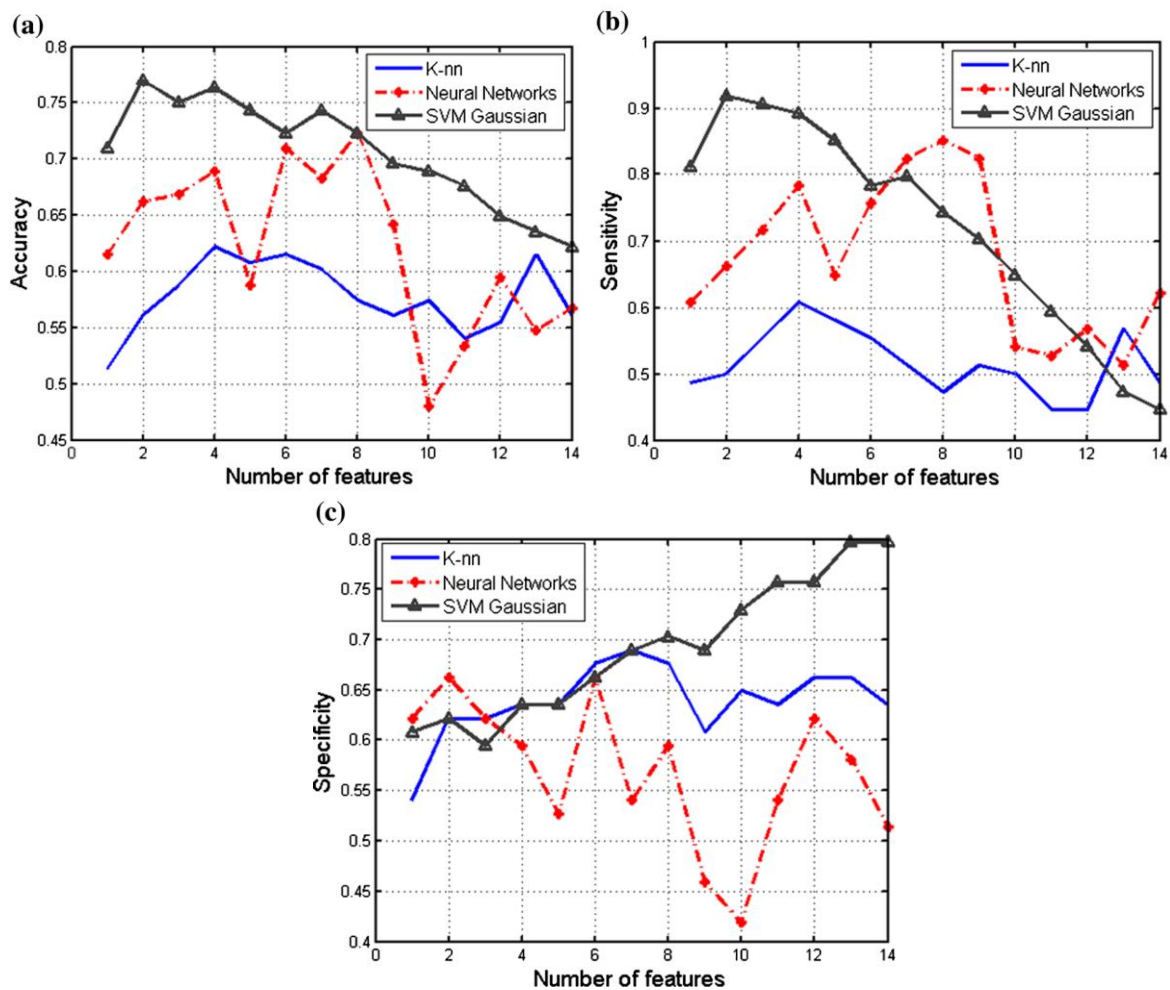


Figure 31. Quantitative evaluation of the classifiers with different number of features, increased progressively by order of rank, a) accuracy, b) sensitivity and c) specificity.

Table 13 displays the best performance of each classifier. For evaluation we consider three different aspects. The first one is the simplicity, where a low number of features is preferred over a complex and numerous set of features. The second one is the high sensitivity to detect precancerous lesions so that if a sample is classified as precancerous it is very likely that effectively is precancerous tissue. Generally speaking it is preferable to obtain false positive samples or samples of healthy tissue classified as precancerous that will follow further medical studies than missing a precancerous lesion. Finally, the accuracy to obtain the maximum number of samples from healthy and precancerous tissues correctly classified.

Table 13. Best performance of the classifiers.

	<b>SVM</b>	<b>NN</b>	<b>K-nn</b>
<b>Number of features</b>	2	8	4
<b>Accuracy</b>	0.77	0.72	0.62
<b>Sensitivity</b>	0.91	0.85	0.61
<b>Specificity</b>	0.62	0.59	0.63

The best performance of k-nn is achieved with 61% sensitivity and 4 top-ranked features, which is not acceptable for the identification of precancerous tissues. On the other hand, the 85% and 91% sensitivity of NN and SVM respectively are strongly remarkable. However, SVM outperforms the other classifiers in terms of accuracy, sensitivity and specificity with two or four top-ranked features. These strong differences on the classification performance are expected since each classifier has a different learning rate. Unfortunately, we do not have a clear explanation on the relation between the top ranked statistical features with respect to the biological conditions encountered in the gastric tissue.

These encouraging results show that it could be possible to identify patients with precancerous conditions. As part of the improvements, we consider that the inclusion of more features could help in the identification, in particular those that can be correlated with biological parameters such as the decomposition of the spectrum in absorption and scattering. Additionally, we consider that testing other classification approaches such as elastic nets and decision trees could provide a more robust solution for the identification of malignancies. Further studies should be performed including more patients and other gastric pathologies poorly identified during gastroendoscopy.

The main advantage of the acquisition system based on a filter wheel is that it allows us to collect multispectral images from gastric tissues during gastroendoscopy. Regrettably, it has two main limitations. The first one is related to the long time required to collect a multispectral image. This acquisition time is enough to produce motion artifacts which affect the image quality and risk the registration of the monoband images. The second one is with respect to the limitation to collect the spectrum above 640 nm, which reduces the

capability to analyze the effect of other biological conditions such as water content and the size of the scatters in the gastric tissues.

Taking these circumstances in consideration, we propose a different acquisition system, an updated version which includes a multispectral camera to collect the multispectral images in a single shot and covers a wider spectrum, including the red and near infrared bands. This system will be described in the following section.

## 5.2. Identification of precancerous lesions from the prototype GEMS (Gastro Endoscope MultiSpectral)

This subsection turns on the acquisition system GEMS. This system was conceived to overcome the limitations identified on the previous prototype which was based on a filter wheel. In particular, we increase the spectral range of the system by acquiring the NIR wavelengths and the reduction of the acquisition time by collecting a multispectral image in a single shot. In the next subsections we will explain the different parts of the acquisition system, the processing of the acquired multispectral images and finally, we use this system in a clinical study for the identification of precancerous lesions.

### 5.2.1. Acquisition system

The system GEMS is designed to acquire multispectral images from the gastric mucosa. The general diagram is displayed in figure 32. Similar to the prototype based on a filter wheel, it takes advantage of a gastroendoscope in order to access the stomach but this time the gastric mucosa is observed by two imaging systems. The first one is the camera integrated in the gastroendoscope, which we use as a white light image. The second one is from a microendoscope which collects the multispectral image.

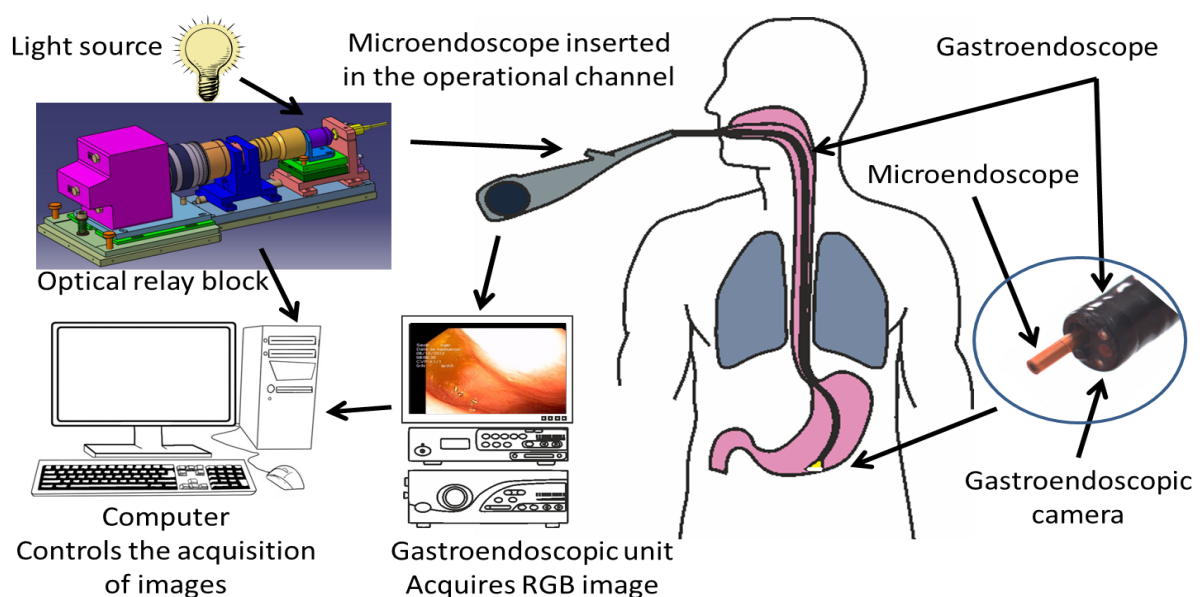


Figure 32. Elements of the system GEMS.

The main 5 parts of the system GEMS are the gastroendoscopic unit, the microendoscope, the source of light, the block of optics which allows us to transfer the image from the fibers to the sensor of the multispectral camera Flux Data and finally the software to pilot the acquisition of the images. We will describe each of these elements in the following subsections.

### 5.2.1.1. Gastroendoscopic unit

The gastroendoscopic unit is the Olympus Exera II which includes the gastroendoscope, a source of light and a video processing unit. The tip of the gastroendoscope includes the fibers to illuminate the gastric tissue, the gastroendoscopic camera, an injector of water and air for use during medical procedures and the operational channel. The other end of the gastroendoscope is bifurcated. One connector goes to the source of light, which also provides insufflation and water. The other one is connected to the video unit as displayed in figure 33.

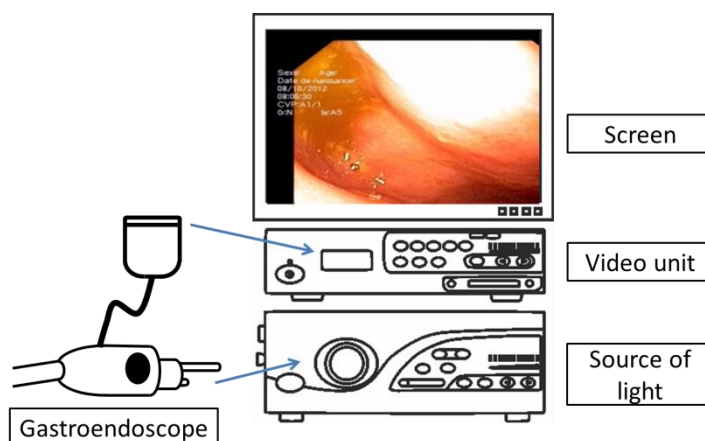


Figure 33. Gastroendoscopic unit. The gastroendoscope has two connections, one to the video unit and the other to the source of light.

The video unit processes the images acquired with the camera. It transfers the image to the screen to be observed by the practitioner. The image from the gastroendoscope is updated in real time. In this sense, we record the gastroendoscopic image displayed at the same time that the trigger of the multispectral camera.

### 5.2.1.2. Microendoscope

The microendoscope has a diameter of 2.5 mm, which fits perfectly into the operational channel of the gastroendoscope as observed in figure 34. Additionally in this image we can observe the different elements of the tip of the gastroendoscope.

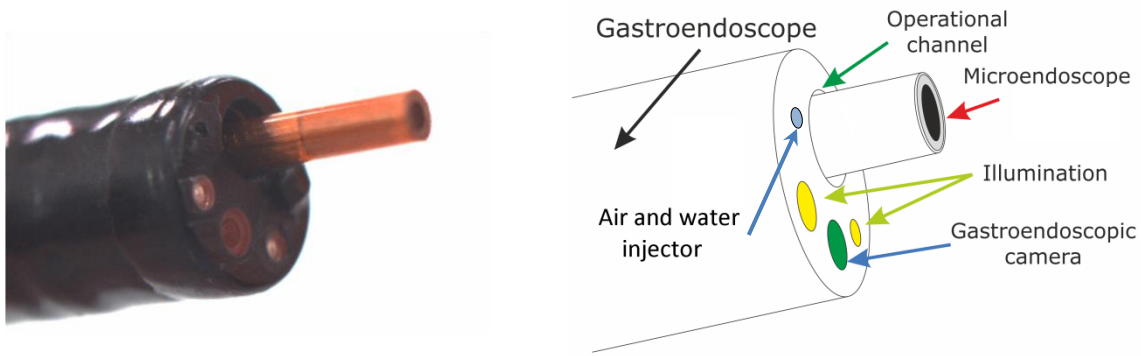


Figure 34. Elements at the tip of the gastroendoscope and the microendoscope in the operational channel.

The microendoscope has a length of 2,500 mm, a field of view of 60° and it includes 30,000 fibers to transport the image of the gastric tissue to the exterior of the body of the patient. The output of the optical fiber strand has a diameter of 0.8 mm and a numerical aperture of 0.4.

After the acquisition of gastric images, the microendoscope is disinfected, following standard medical disinfection and sterilization by using peracetic acid which do not damage the microendoscope [123].

In the next subsection we will describe the source of light and the connection with the gastroendoscope.

### 5.2.1.3. Source of light

As part of the characteristics to improve in the previous prototype based on a filter wheel, we identify that we were not able to acquire the reflectance in the red wavelengths and the NIR. We consider that this situation is mainly due to the fact that these wavelengths are filtered in the source of light of the gastroendoscopic unit displayed in figure 35.a. The filtering could be performed through a dichroic filter or an elliptical reflector which reflects only the wavelengths in the visible range.

In order to overcome this issue, we chose to illuminate the tissue with an external source of light. In this sense we chose a Xenon lamp which typically provides a relative flat spectrum in the visible range. The power of the source of light is 175 W and the NIR wavelengths are not filtered as can be observed in figure 35.b.

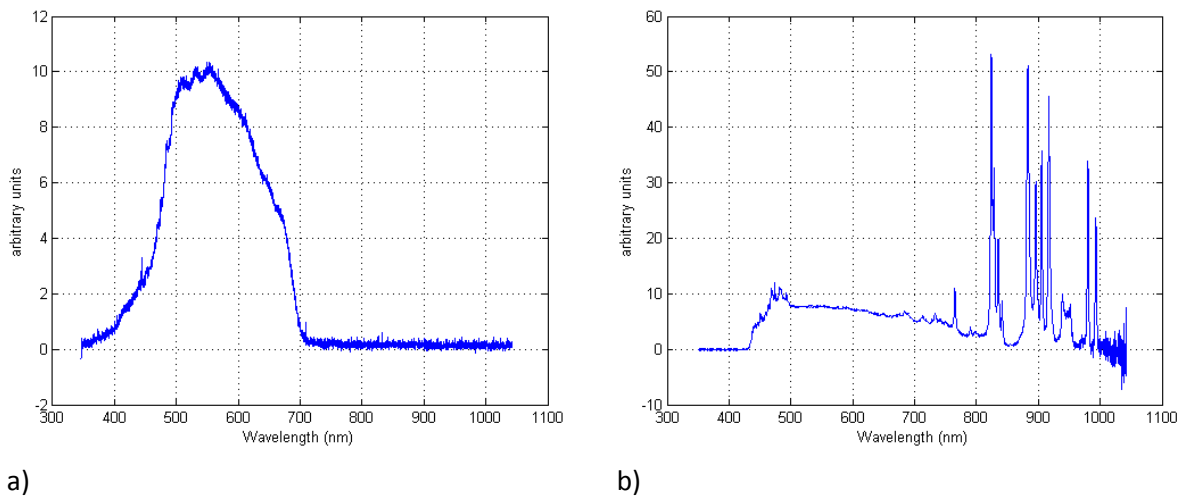


Figure 35. Spectrum from the light source of the a) Gastroendoscopic unit, which does not provide illumination above 700 nm and b) Xenon lamp from the system GEMS which includes the NIR.

The inclusion of this external source of light creates some issues. The first one is related to the distribution of the light. In figure 36 is observed the tip of the gastroendoscope which includes two groups of fibers oriented to illuminate the tissue and the microendoscope to collect the image in the operational channel. Under this geometrical configuration, the distance D1, D2 and D3 are not assured to be constant during the acquisition.

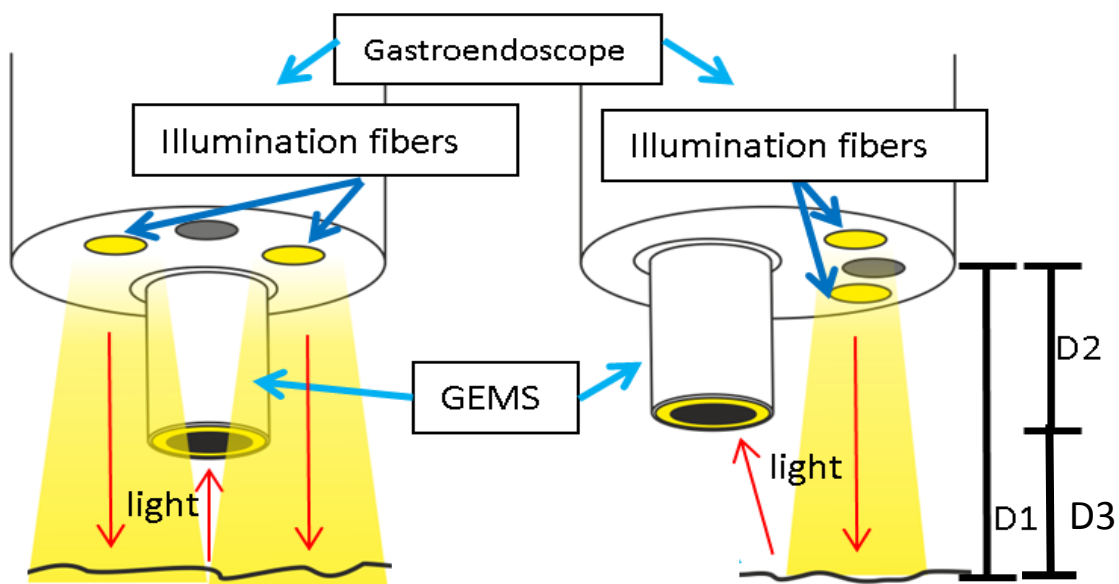


Figure 36. Distribution of light when using only the source of light from the gastroendoscope. The distances D1 (gastroendoscope to tissue), D2 (gastroendoscope to microendoscope) and D3 (microendoscope to the tissue) are not assured to be constant.

In figure 37 are displayed the test of this configuration in order to capture a chess pattern. We observe that using the fibers of the gastroendoscope to illuminate the scene the collected image from the microendoscope is considerably dark whereas the image from the gastroendoscope is close to saturation. Using this configuration could require to increase



the integration time of the camera to get an image with a better quality, but, the images could be blurry and display motion artifacts.

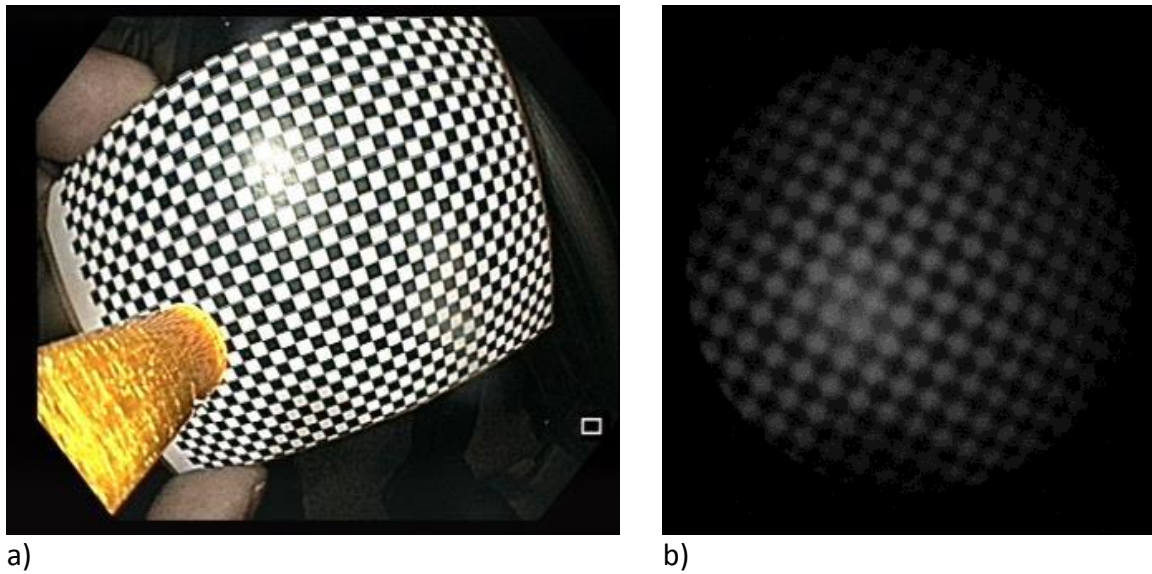


Figure 37. Acquisition of a chess pattern illuminated with the gastroendoscope. a) image from the gastroendoscope and b) image from the microendoscope in the first channel of the multispectral camera, which is considerably dark.

Under these circumstances, we connect the source of light to the illumination fibers from the microendoscope which are distributed in a ring around the imaging fiber bundle. The resulting geometrical configuration for the illumination is displayed in figure 38. Similar to the previous configuration, the distances  $D1$ ,  $D2$  and  $D3$  are not assured to be constant during the acquisition.

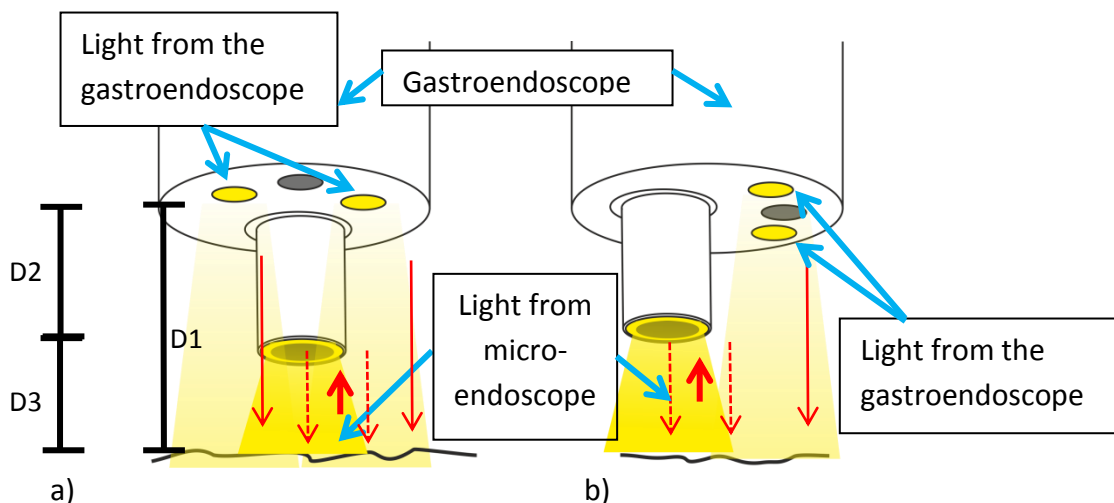


Figure 38. Illumination using the gastroendoscope and GEMS, the captured light (bold red arrows) is mainly the contribution from the microendoscope (dotted red arrows) and in lower amount the light from the gastroendoscope (thin red arrows).

The image captured by the microendoscope is the result from the contributions of the light from the gastroendoscope and the illumination from the microendoscope. In this sense, we

must highlight that the spectrum from the two light sources is different, which contribution varies depending on the distance with respect to the scene. This configuration induces significant uncertainties with respect to the lighting spectrum. In order to solve this issue, we take advantage that the contributions of the gastroendoscope are negligible when the power is reduced to a minimum value since the power of the light from the microendoscope is highly superior that the gastroendoscope. This configuration provides images from the microendoscope less dark and suitable to be exploited as observed in figure 39.

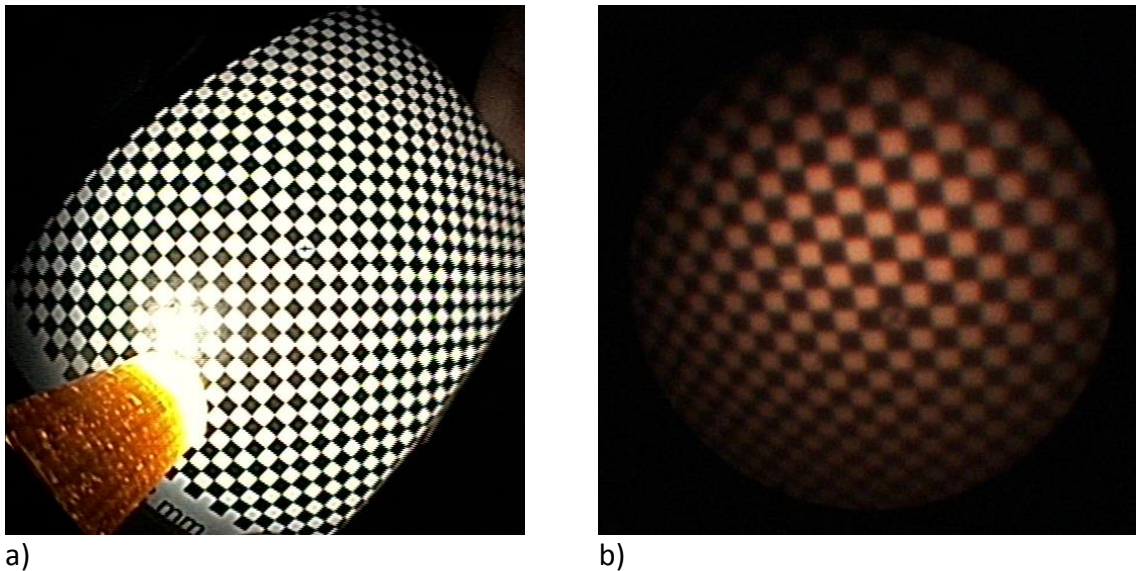


Figure 39. Acquisition of a chess pattern illuminated with the source of light from the microendoscope. a) image from the gastroendoscope and b) image from the microendoscope.

In order to avoid damaging the tissue with the delivered power, a typical gastroendoscope delivers 1.5 W. In our case, we measure the power from the microendoscope with the powermeter Gentec-EO TPM-300 and the sensor thermopile ps-330wb. The delivered power from the microendoscope was 0.28 W. Considering the source of light of 175 W and the delivered power of 0.28 W there is a significant loss of energy. This situation is due to different factors, for instance the conversion efficiency from electrical power to luminal power, the lamp produces light in all directions and it is only a part of it is collected for transportation and absorption by the fibers since we observe that the temperature of the microendoscope was increased after use.

#### 5.2.1.4. Optical relay block

This module is designed to transfer the output image from the microendoscope into the sensors of the multispectral camera Flux Data. As was previously mentioned, the output of the optical fiber strands has a diameter of 0.8 mm and a numerical aperture of 0.4. The photographic lens of the camera Flux Data has an effective focal length of 25 mm and the camera sensors have 658 x 492 pixels for the two sensors in the visible range and 659 x 494 for the sensor in the NIR with a pixel size of 9.9  $\mu\text{m}$  for both type of sensors. A rigid

registration was performed to achieve an overlap between the images from the three sensors.

This module transfers the image from the 0.8 mm diameter fiber bundle of the microendoscope on a disk with a diameter of 450 pixels on the sensor of the camera Flux Data. Then, the magnification is computed following equation 32, obtaining an expected magnification of ~5.6 times.

$$\text{magnification} = \frac{\left( \frac{\text{Diameter of the disk}}{\text{in the image in pixels}} \right) \left( \frac{\text{pixel size}}{\text{in mm}} \right)}{\text{Diameter of the fiber strands in mm}} = \frac{(450)(0.0099)}{0.8} \approx 5.6 \quad \text{eq (32)}$$

The optical relay block is designed to provide limited chromatic aberration between 400 nm and 1000 nm spectral range and to collect all the light that exits from the fiber bundle. This optical system is displayed in which was designed by MCF Hervé Sauer from the Institut d'Optique Graduate School. The description of the components is enlisted in table 14.

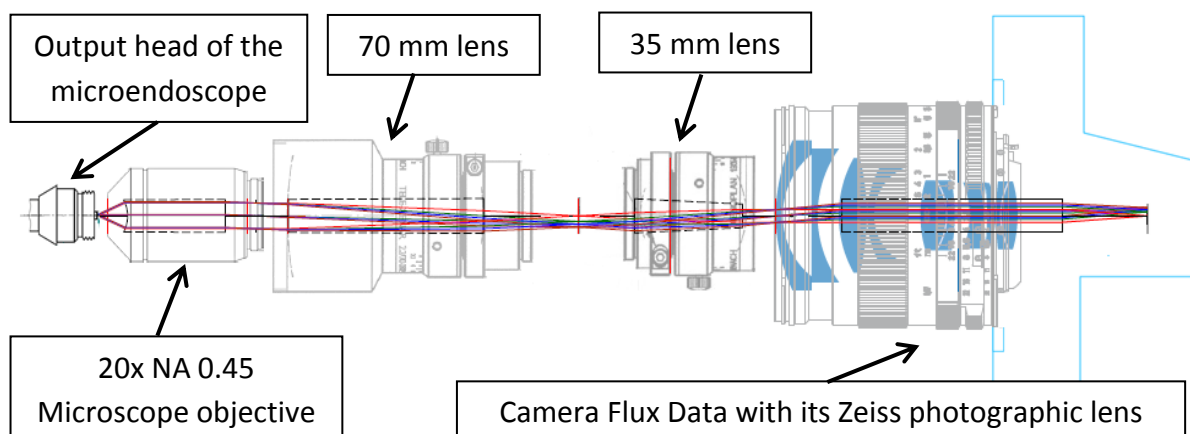


Figure 40. Optical design to transfer the image from the microendoscope to the sensor of the camera Flux Data.

Table 14. List of elements of the optical relay block.

Component	Characteristics
Microendoscope	30,000 fibers in a diameter of 0.8mm with a numerical aperture of 0.4
20x NA 0.45 Microscope objective	Olympus MPLFLN 20x/0.45 ∞/0
70 mm lens	VIS+NIR 2/3" Schneider-Kreuznach Tele-Xenar 2.2/70 kompakt
35 mm lens	VIS+NIR 2/3" Schneider-Kreuznach Xenoplan 1.9/35 non kompakt
Camera Flux Data	Objective Zeiss Distagon T* 2.8/25 ZF

The image at the output of the optical fiber strands is transferred to infinity with an infinity corrected flat-field semi-apochromatic commercial microscope objective, which has a 0.45 NA which is slightly bigger than the 0.40 NA of the microendoscope fibers and 9 mm focal length which is a 20x magnification for a 180 mm microscope tube lens. Such magnification leads to an object field of view largely greater than the required diameter of 0.8 mm of the microendoscope output. Then, to match the angular field of view of the multispectral camera with its Zeiss 25 mm lens, the image is magnified angularly by  $(-70.5/34.9) = -2.02$  by two commercial industrial vision lenses, specifically chosen to be simultaneously corrected for the visible and the NIR spectral ranges. The configuration head to tail builds an afocal system when the two objectives are each focused at infinity. We must highlight that this afocal system is a crucial element in the design as it also sends the exit pupil from the microscope objective close to the virtual entrance pupil of the Flux Data camera Zeiss lens. This pupil conjugation is absolutely required to avoid a strong vignetting that could reduce the field of view to a small part of the 0.8 mm output diameter from the microendoscope. Finally, the Flux Data camera lens is focused at infinity to collect the image of the afocal assembly. The expected magnification can be corroborated by equation 33.

$$\text{magnification} = \frac{25 \text{ mm (Zeiss)}}{9 \text{ mm (Olympus)}} \frac{70.5 \text{ mm (Schn - Kr)}}{34.9 \text{ mm (Schn - Kr)}} = 5.611 \quad \text{eq (33)}$$

The full optical relay is displayed in figure 41. The optomechanical setup was designed and built by the mechanical workshop from the Institut d'Optique Graduate School.

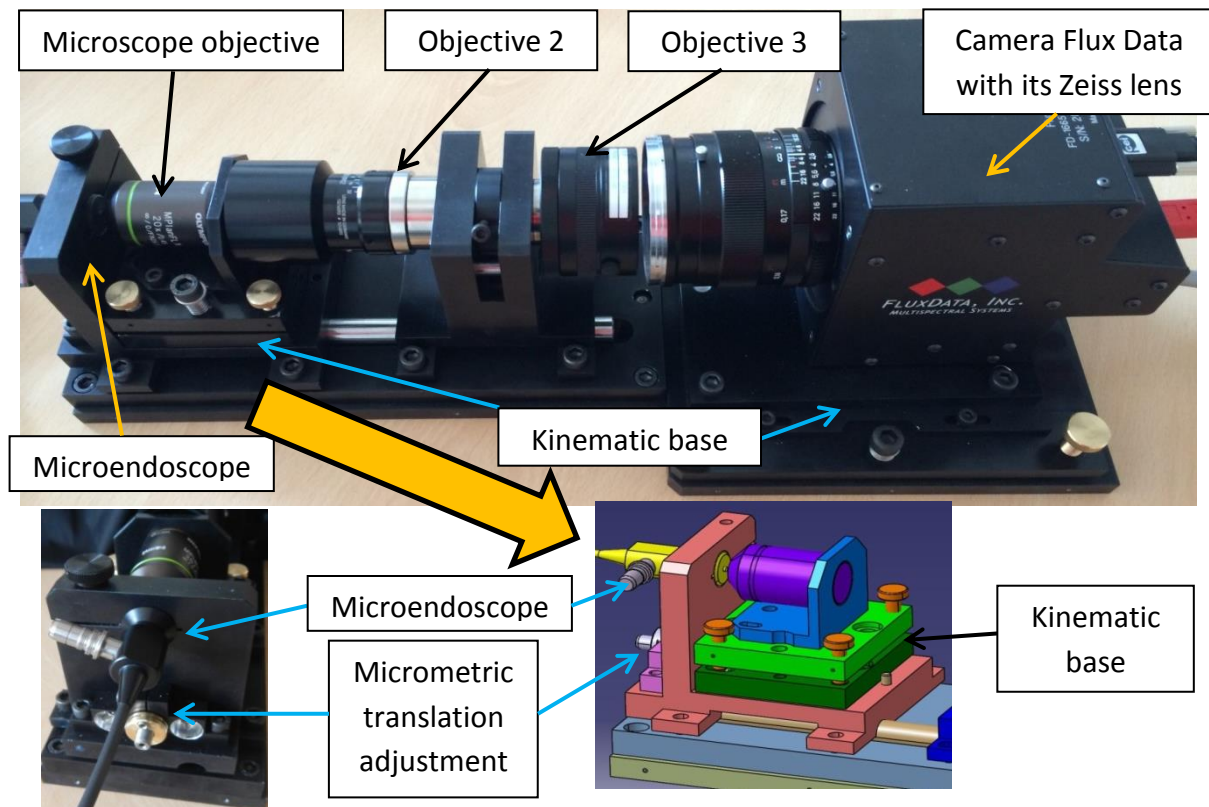


Figure 41. Mechanical components of the optical relay block.



It includes in the specifications an accuracy of  $\pm 1 \mu\text{m}$  in the axial position of the microendoscope and an accuracy of  $\pm 9$  arcmin between the optical axis of the microscope objective and the normal to the optical fiber strands.

We can notice that the mechanical setup includes an adjustment on the translation of the objective from the microscope to achieve  $\pm 1 \mu\text{m}$  accuracy and two kinematic bases, the first one to adjust the orientation of the optical axis of the microscope objective, the second one for the orientation of the camera Flux Data.

This system has some limitations, for instance we have low spatial resolution because the image transported by the fiber bundle is only a section of the size of the image that the multispectral camera can acquire. Additionally, the image formed on the fiber bundle output should be slightly blurred in order to avoid the Moiré pattern encountered when the optical relay block is in focus as observed in figure 42.

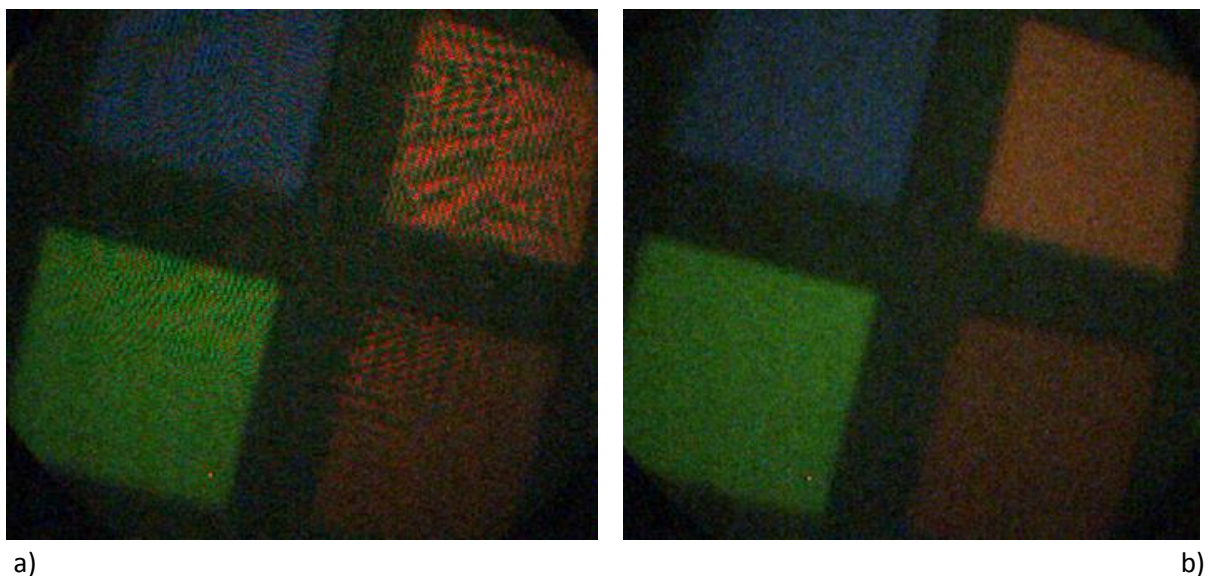


Figure 42. Image from the microendoscope a) In focus where the Moiré pattern is clearly observed, b) Image out of focus to be slightly blurred in order to avoid the Moiré pattern.

#### 5.2.1.5. Software for GEMS

In figure 43 is displayed the graphical visual environment that was developed for the system GEMS. It was coded in Microsoft Visual C++ Express edition 2010 to collect two types of synchronized images. The first one is the VGA image from the gastroendoscope acquired with a video acquisition card. The second one is the 7 channels multispectral image collected by a Fire-Wire port. The interface was designed to be user friendly, intuitive with 3 available buttons. The first one is used to start the acquisition, the second one to stop the acquisition and a third one to exit the application. The collected images are displayed in real time for the user. The program runs under a windows operating system (Windows 7). The microendoscope after insertion in the operational channel of the

gastroendoscope arrives up to a point that is visible by the camera of the gastroendoscope so that the practitioner can observe both images in the screen.

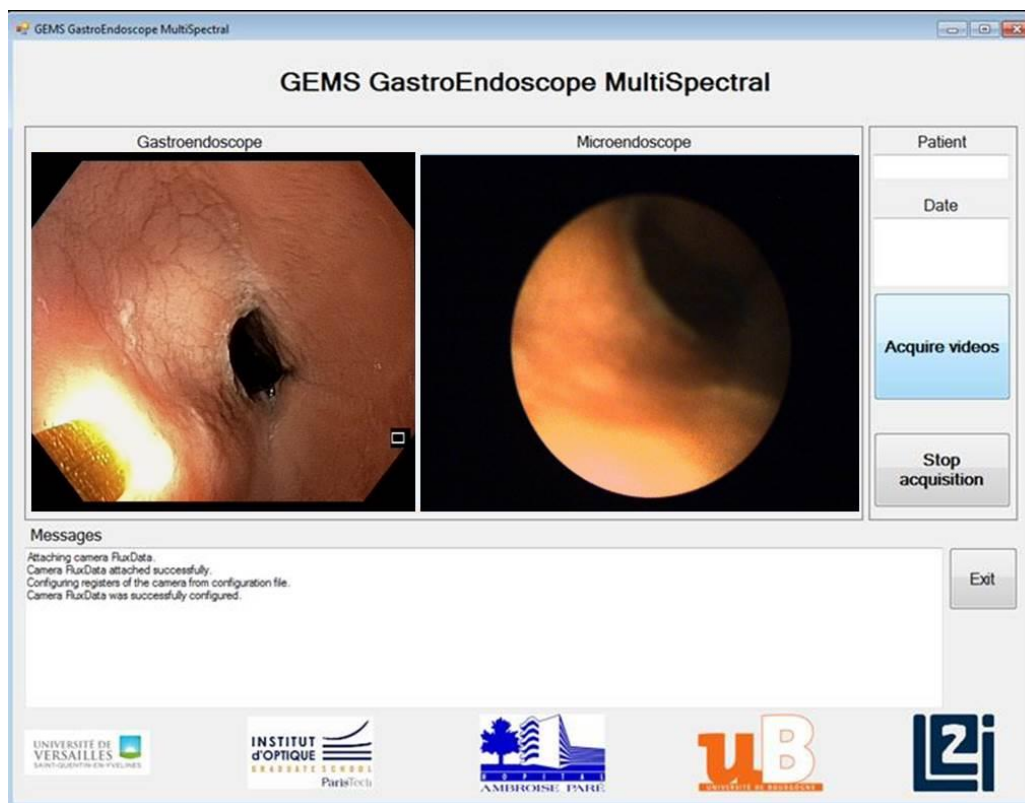


Figure 43. Graphical user interface for the system GEMS. On the left is the image from the gastroendoscope where the microendoscope is observed. On the right is the image collected by the microendoscope.

The description of the image processing methodology implemented for the collected multispectral images is detailed in the following subsection.

### 5.2.2. Preprocessing of multispectral images

For this clinical study, the acquired multispectral images were from the antrum. Similar to the acquisition system based on a filter wheel, the source of light is constant so that the collected images when the gastroendoscope is far away from the gastric tissue are considerably dark, producing a low signal to noise ratio. Under these circumstances, these multispectral images were removed.

The image of the gastric tissue collected by the microendoscope is observed in a circle, typically at the center of the picture. The position of this circle could be slightly shifted by some pixels between acquisitions. This situation is mainly due to the physical connection of the microendoscope to the block of optics.

In order to identify the active area of the microendoscope, we identify that sometimes during the acquisition the distance between the microendoscope and the tissue is considerably small, producing as a consequence a saturated image. This image is almost a perfect binary image where the working area is in white and the background is black. We approximate the area by using a circle Hough-transform obtaining a circle typically of 400 pixels diameter. We can observe in figure 44 the active area of the microendoscope in a blue circle.

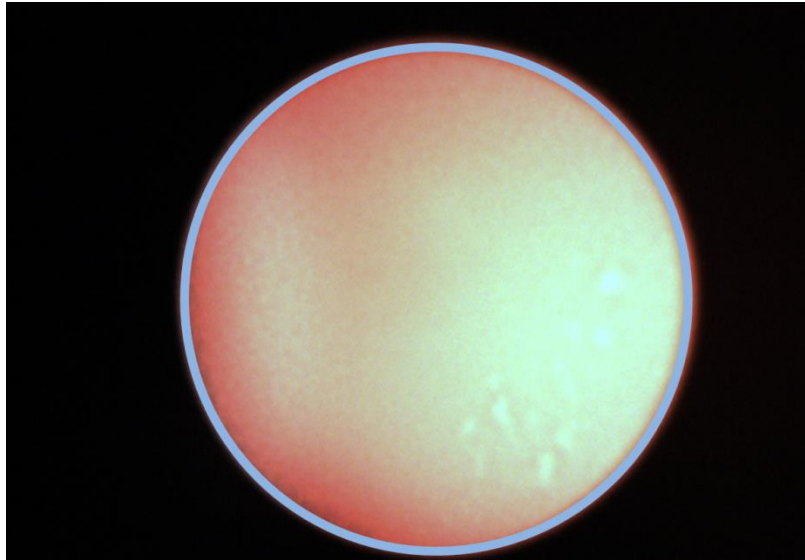


Figure 44. Active area of the microendoscope, identified with circular Hough transform.

After that, the user manually selects the region of interest in order to remove artifacts such as bubbles of gastric juice, border of folds of the gastric tissue and the pylorus sphincter. Then, the specular areas are removed by threshold with a value of 240/255. An example is displayed in figure 45 where the antrum and specular reflections are removed.

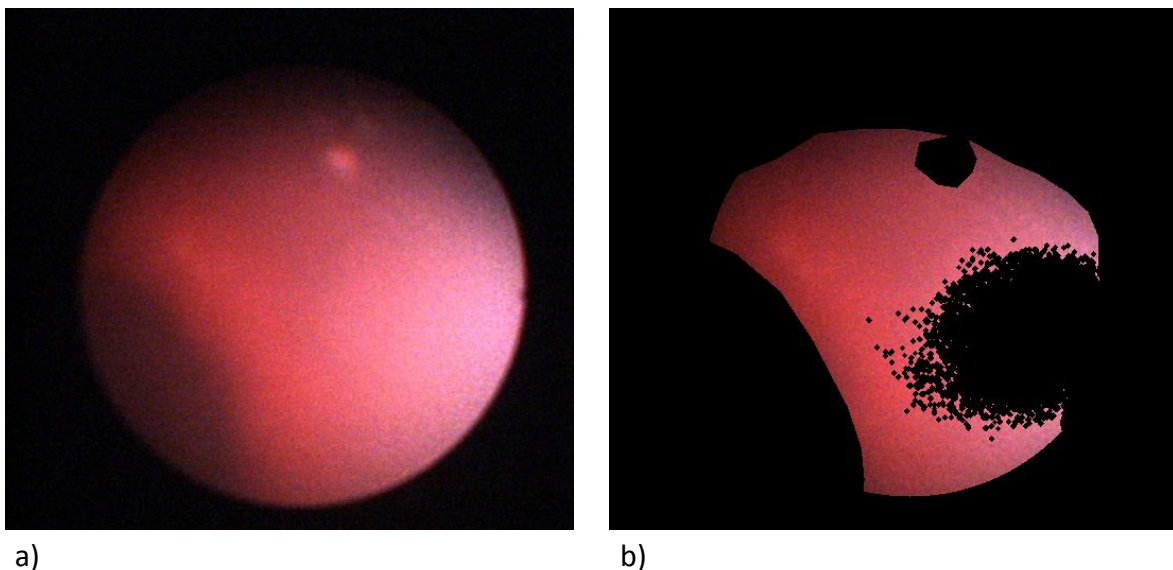


Figure 45. a) Simulation of white light image from the multispectral image where we observe the antrum (left) and specular reflections (top and right). b) Manually selection of the region of interest.

From the region of interest, we empirically chose 20 patches of size 5 x 5 pixels, which were randomly selected and averaged in order to obtain a single spectrum from each multispectral image. After that, the normalization L1 was used on the averaged spectrum. This procedure was repeated 10 times, oriented to include possible changes in the shape of the spectrum in the multispectral image. In the next section, we describe the characteristics of the database and the collected multispectral images.

### 5.2.3. Database

This subsection is devoted to describe the characteristics of the population of patients and the multispectral images that were collected.

#### 5.2.3.1. Subjects

This clinical study included patients referred to the endoscopic unit of the hospital Ambroise Paré, Boulogne-Billancourt, France, during the period of one year and a half, between July 2014 and December 2015. Similar to the previous clinical studies, the patients were scheduled for gastroendoscopy under general anesthesia. As part of the gastroendoscopy procedure, biopsies were collected from the antrum and corpus analyzed histologically to provide the diagnosis of the patient. Additionally, the infection from *H. pylori* was graded by immunochemistry by using PCR.

The characteristics of the patients from this clinical study are displayed in table 15. In total 20 patients take part of this study. They were separated in two groups according to their diagnosis: healthy or precancerous. The healthy group includes patients with normal mucosa and gastric inflammation which makes them part of the control group. The patients with precancerous conditions included atrophy and intestinal metaplasia. It is important to mention that there were no significant differences in age between the two clinical groups ( $p > 0.05$ ).

Table 15. Clinical features from the patients.

	<b>Number of patients</b>	<b>Age (+/-SEM)</b>	<b>Gender ratio (H:F)</b>
<b>Group with precancerous lesions</b>	5	74.4 (4.46)	2:3
<b>Control group</b>	15	59.20 (3.46)	4:11



### 5.2.3.2. Collected multispectral images

The 20 patients of this study include a total of 1383 multispectral images, 1143 are part of the control group and 240 are included in the precancerous group.

In table 16 are displayed the mean number of studied images for the two clinical conditions. There was no significant statistical difference between the two groups in terms of the mean number of multispectral images for each patient ( $p > 0.05$ ).

Table 16. Mean number of multispectral images for the two clinical groups.

Diagnosis	Group with precancerous lesions (N=5)	Control group (N=15)
Mean number of multispectral images per patient (+/- SEM)	76.2 (17.04)	48.0 (16.90)

The next section is oriented to the statistical analysis of the precancerous lesions.

### 5.2.4. Statistical analysis

The collected samples from the control group are displayed as box plots in figure 46. From this figure we observe that the samples show a trend to a homogeneous distribution with some outliers which are highlighted as a red cross.

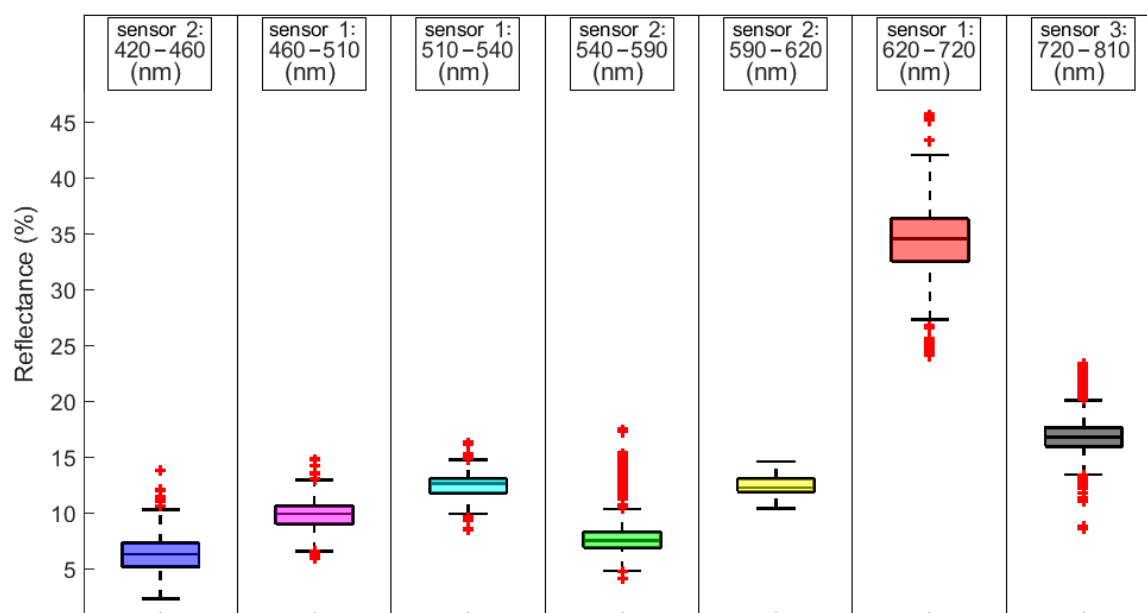


Figure 46. Distribution of samples from the control group.

Taking in consideration this behavior, we can estimate a reference spectrum based on the mean spectrum of the normalized data from the control group. Then, this reference spectrum is used to compare the normalized spectra from the precancerous group. The outcome of this comparison is oriented to identify the percentage of variation between the two groups, as displayed in figure 47.

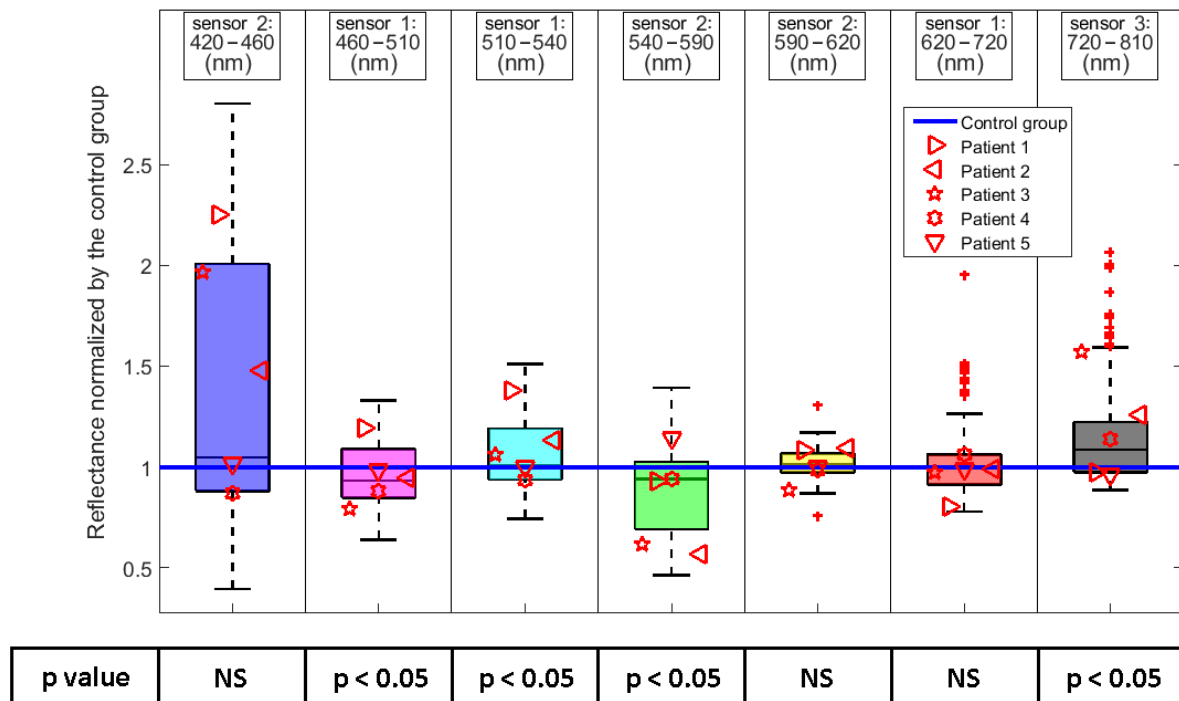


Figure 47. Ratio of variation in the spectrum from patients with precancerous lesions compared with the spectrum from the control group.

Additionally, in the same figure we observe the result from the statistical analysis ANOVA, which is used to identify significant statistical differences between the two groups at each waveband. We must highlight that the general trend of the patients with a precancerous profile is slightly different with respect to the one observed in the previous clinical study with the prototype with a filter wheel. However, there is an agreement between the two clinical studies with respect to the statistical significant wavebands, which are those between 460 nm and 540 nm. From the previous clinical study we hypothesize that these wavebands are related to the oxygen saturation, but we do not have a clear biological explanation for the differences on the measured reflectance with the two acquisition systems. In this sense, an increment of the reflectance with the system based on a filter wheel and a decrement in the reflectance with the system GEMS in the same region of the spectrum. We consider that this situation could be related to the spectral sensibility of the sensors and the cross talk, in particular with the system GEMS to the red wavebands as was previously discussed in chapter 3.

In contrast with the previous clinical study, the waveband between 540 to 590 nm was identified as statistical significant with the system GEMS; these wavebands could also be

related to the oxygen saturation. We consider that these wavebands were not identified in the previous study due to the spectral resolution of the acquired image.

We observe that waveband between 510 and 540 nm displayed a higher reflectance. We could relate the origin of these differences to the spectral sensibility of the filters and the cross talk with respect to other channels, in particularly with the red wavelengths as was mentioned in the previous chapter. Another important similitude with respect to the previous clinical study is that the red wavebands, between 600 nm and 700 nm were not identified as significant.

A main advantage from the system GEMS is that we have higher spectral resolution, so that we have access to the NIR. This waveband was identified as statistical significant for the diagnosis. The variation in the NIR could be related to biological changes in the water content and a smaller proportion to the size of the scatters and the oxygen saturation as mentioned in chapter 2. The precancerous group showed an increment in the reflectance with respect to the control group and it could be related to the development of precancerous tissues by the replacement of glands by fibrous tissues. Additionally the mucosa from precancerous tissues is mentioned by practitioners as thicker than normal mucosa. In this sense, we could consider that these thickness or turbidity with a high concentration of suspended materials or small scatters play an important role to increase the reflectance.

It is clear that a model of light tissue interaction applied to the collected spectra could be used to analyze the scattering originated in the size of the molecular structures. Additionally, it could provide significant information to improve the biological interpretation of the changes in the gastric tissues.

### **5.2.5. Classification of multispectral images with precancerous lesions.**

In this subsection we develop the methodology evaluated to differentiate the patient according to their clinical condition. We follow the procedure described for the differentiation of precancerous lesions from the prototype based on a filter wheel. It follows the computation of statistical features from the normalized spectrum, the evaluation and ranking according to their discriminative information to differentiate the clinical condition and the classification in order to differentiate pathological tissues.

#### **5.2.5.1. Balance of the database for classification tasks**

Similar to the database collected from the prototype based on a filter wheel, our database is imbalanced since we have more patients with healthy mucosa than precancerous lesions. In this sense, the images from precancerous lesions were resampled, following the

procedure described in section 2.2 from this chapter where 20 patches of 5 x 5 pixels were extracted and averaged in order to obtain additional measurements from the multispectral images of patients with precancerous lesions. This procedure was repeated until we obtain the same number of samples for the group of healthy mucosa and the group of precancerous tissues.

### 5.2.5.2. Extraction of features

Assuming that the spectrum follows a probability distribution, we can extract statistical features from it. We can observe in table 17 a list of features which were extracted from the spectrum, including those mentioned in the analysis of the precancerous lesions from the prototype based on a filter wheel and a new feature which is the interquartile range and the normalized intensities from the spectrum. The ranking of these features will be explained in the next section.

Table 17. Ordered list of features

Rank	Feature
1	Median of absolute deviation
2	NIR
3	Inter quantile range
4	Waveband between 540 – 590 nm
5	Kurtosis
6	Waveband between 460 – 510 nm
7	Waveband between 510 – 540 nm
8	Variance
9	Waveband between 590 – 620 nm
10	Skewness
11	Mean deviation about median
12	Waveband between 420 - 460 nm
13	Waveband between 620 – 720 nm
14	Standard deviation
15	Entropy
16	Mean of absolute deviation

### 5.2.5.3. Feature ranking

The features are ranked according to their discriminative information to differentiate between the two clinical conditions. Similar to the previous analysis, the metric is the pooled variance t-test as displayed in figure 48. We identify that the wavebands in the NIR as well as the channels identified as statistical significant from the statistical analysis are top ranked. Statistical features remain top ranked, but we identify that some of them

change its rank; this is expected, since the acquired spectrum is wider and it includes more samples than the one collected with the filter wheel. Additionally, it could also be due to the sensibility of the multispectral camera.

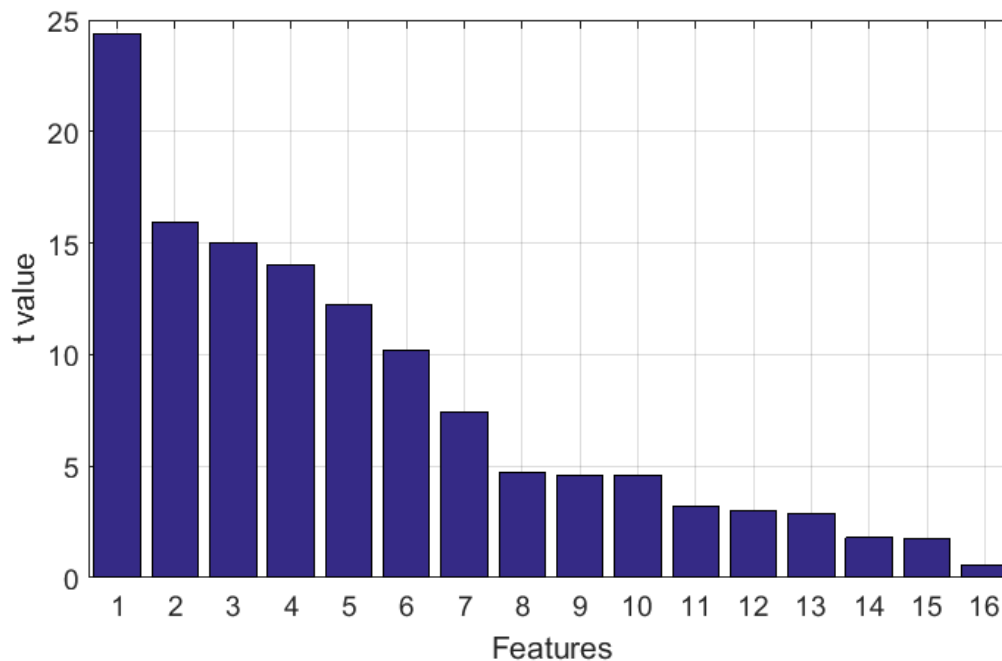


Figure 48. Measurement of the discriminative potential of the ranked features from table 17 by pooled variance t test.

#### 5.2.5.4. Classification

In order to evaluate our approach we follow the test of three common supervised classification approaches which are K-nn, SVM and NN which were described in chapter 2. We follow the procedure described for the differentiation of multispectral image from healthy and precancerous lesions described in the previous clinical study based on the prototype with a filter wheel.

As part of the evaluation of the classification, we use LOPOCV so that we take one patient at a time for testing whereas the classifier is trained with all the remaining patients. This separation in the database includes the feature ranking so that there is no information from the patient under test during the training. Additionally, each classifier was tested iteratively with an incremental number of features, according to their rank obtained from the feature ranking. Finally, the performance of the classification is evaluated quantitatively taking as a metric the accuracy, sensitivity and specificity.

#### 5.2.5.5. Results of the classification

The results of the classification are displayed in figure 49. We would expect a performance similar to the previous clinical study but it was not the case. This situation could be related to the low number of patients with precancerous lesions used for this study which could

display dispersion and limited overlap in their measurements, making difficult for the classifiers generate the classification rules. Other factor could be related to the sensibility of the system and that the measurements include cross talk between other channels, especially from the red wavelengths which are not candidates for the differentiation of the pathology as was previously identified in the statistical analysis.

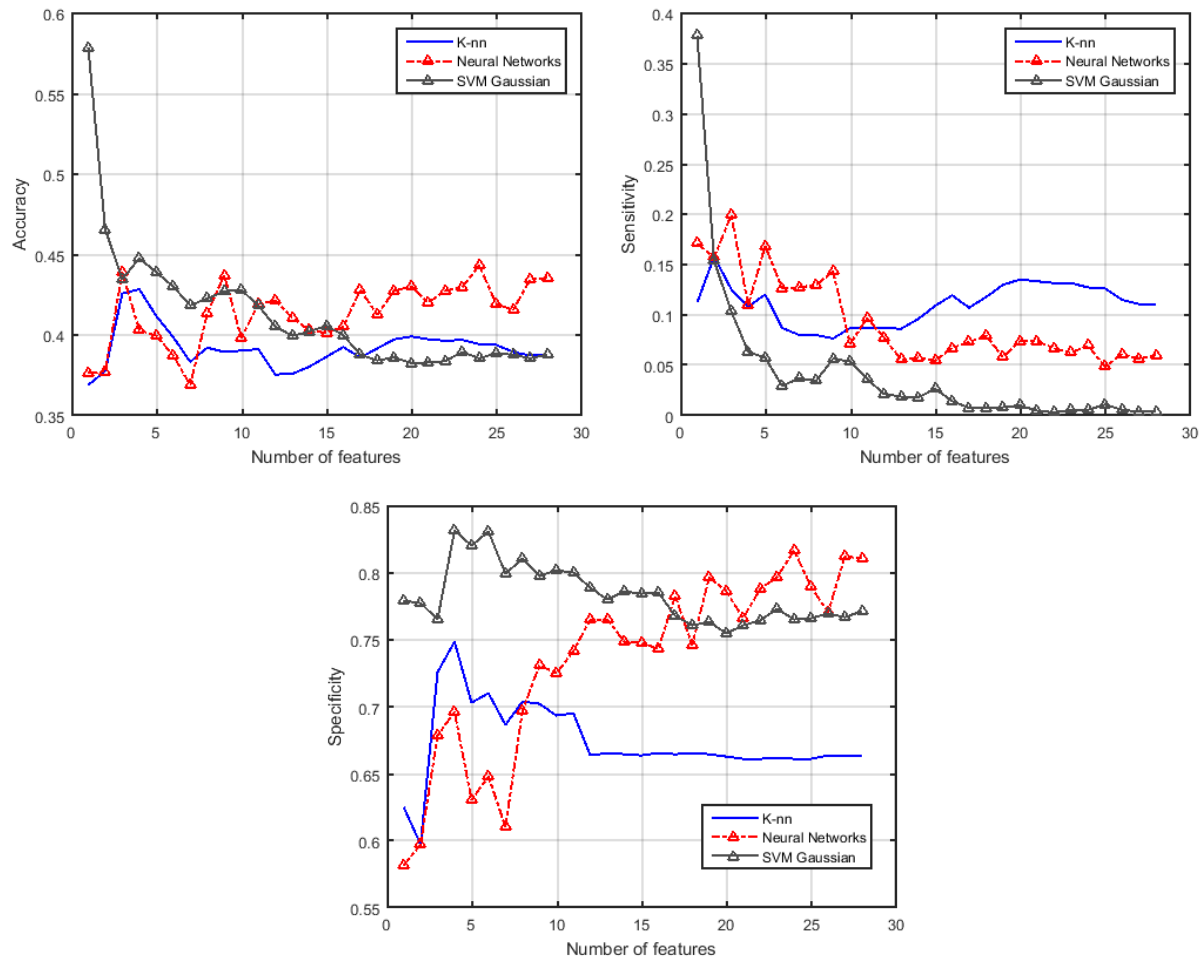


Figure 49. Quantitative evaluation of the classifiers with different number of features, increased progressively by order of rank, a) accuracy, b) sensitivity and c) specificity.

On the other hand, from this study we can analyze the identification of healthy mucosa; there are more patients with this clinical condition with respect to precancerous lesions. These samples will display some overlap or repeatability on the measurements which could be learnt by the classifiers, allowing us to reach specificity above 60 % and as good as 84 % when using SVM. The NN seems to need more features before achieving its maximum performance in terms of specificity.

Similar to the previous study, SVM overcome the other classifiers with a simple hypothesis. The sensitivity is in all the cases below 50 %. Then NN shows its best performance when learning with 17 or more features.

This performance is not satisfactory for a clinical study. Further analyses are required, with more data since it is known that with more examples of patients with pathological tissues,

the classifiers could easily learn the separation. Additionally, further studies are required including other pathologies in the stomach which are poorly identified.

### 5.3. Summary

In this chapter we discussed the clinical study of precancerous lesions from images acquired from two acquisition systems. The first acquisition system was based on a filter wheel whereas the second one is based on a multispectral camera (system GEMS).

The system GEMS is oriented to solve the main issues discovered from the prototype based on a filter wheel. Between the main improvements we highlight the acquisition of a multispectral image of 7 channels in a single shot, which allows us to avoid motion artifacts in the images. Other improvement is the increment in the spectral sensibility of the measuring system so that the collected spectrum included six wavebands in the visible range and one in the NIR.

In both clinical studies the samples were separated in two groups according to their clinical condition: healthy or precancerous lesions. The study included a statistical analysis and a classification task.

With respect to the statistical analysis we arrive to similar conclusions from both clinical studies since the wavebands between 460 and 580 nm were identified as statistical significant. The biological modification on this waveband is related mainly to the oxygen saturation.

The increment in the spectral sensibility of the system GEMS allowed us to evaluate the NIR for diagnosis of precancerous lesions. We found that this waveband could help in the diagnosis since it is related to changes in the water content, oxygen saturation and size of the scatters from the tissue. In particular the size of the scatters should be consider for future studies because we consider that the precancerous tissues included more scatters of small size in comparison with the control group. Additionally, we also consider that precancerous tissues have lower oxygen saturation that normal gastric tissue.

The classification task was satisfactory for the first acquisition prototype but not for the system GEMS. We consider that this situation could be related to the low number of patients with precancerous conditions which makes the learning step a difficult task for the classifiers. In this sense, further studies are required to include more patients and to evaluate other pathologies in the stomach which are poorly identified.

## Conclusions and future perspectives

Nowadays there is a strong interest to improve gastroendoscopic procedures to a further point in the diagnosis than the visualization of gastric tissue and the collection of biopsies. In particular, we are interested on the early detection of malignancies which could bring important advantages for the patients, including accurate diagnosis, low invasion and potentially less expensive.

Up to our knowledge, we are the first to perform multispectral analysis from gastroendoscopic images from the gastric mucosa. This exploratory study quantitatively analyzes the variation in the reflectance during the development of malignancies. The objective of this study is to identify wavebands that could be used in the diagnosis for the differentiation of the pathology.

The use of multispectral imaging is considered strongly promising for medical implementation. It has been proof to be practical in other medical domains, such as analysis of the skin. It is known that the light encodes chemical and architectural information from the tissue in a non-invasively way. In this sense, it could be used to provide quantitative information for objective diagnosis. Thanks to the development of new multispectral cameras, miniaturization of sensors and the capacity to handle high amount of data we can evaluate this approach in other medical domains, for instance in the stomach.

This exploratory study demonstrates the use of multispectral images in order to analyze the differences between the spectra of light collected from tissues with different pathologies. We propose two working systems for the acquisition of multispectral images from gastric tissues. The first one is based on a filter wheel whereas the second one is based on a multispectral camera and it was designed to overcome the main limitations from the first one. For instance, the spectral sensibility is increased to cover the visible and the NIR and the multispectral image is acquired in a single shot to avoid motion artifacts.

We first perform an exploratory study in a mice model of infection of *H. pylori* to evaluate the modifications due to the development of active gastritis. The use of animal models of infections allows us to study the bacterium under controlled conditions. In this doctoral work it was performed with NMRI mice. Under this model we can study chronic infection but a mild response of the tissue.



In the mice model of gastritis, we show a significant variation in the mucosa measured at different stages of the development of the inflammation. The analyses show that 3 bands of wavelengths are candidates for the diagnosis of gastritis. These bands are delimited to 430 to 450 nm, between 470 and 590 nm and between 620 and 680 nm and could be related to changes in the size of the scatters, blood concentration and increments in the oxygen saturation during the development of the pathology. The next study should be performed with the mice model C57BL/6 and the strain *H. pylori* SS1. Later on, it is suggested another study for dysplastic and precancerous lesions, including INS GAS mice infected with *H. pylori* SS1 or mice C57BL/6 but with the bacterium *H. felis*.

Taking advantage of the acquisition system based on a filter wheel we performed a clinical study from gastritis. We identify that gastritis in humans modifies the interaction between light and tissue, showing statistically significant modifications in the spectrum at 560 nm, 600 nm and 640 nm. We do not have a clear biological explanation for the modifications observed at these wavelengths. However, we have different hypotheses that could explain these modifications, for instance the microvessels density in inflammation, and the recruitment of neutrophils in conjunction with fibroblast activity in cell arrangements originated in the mechanism of defense and repair from cells. These conditions could impact the oxygen saturation and the size of the scatters.

Another identified feature from the patients diagnosed with gastritis was areas with a wooly dark weft appearance in the band at 560 nm. We believe that these patches could be related to changes in the size of the scatters.

We also identify the NIR as statistically significant and a strong candidate for the differentiation of the pathology. From the NIR we can differentiate the water content and a smaller proportion the size of the scatters and the oxygen saturation. Future studies should be oriented to this waveband or even at longer wavelengths. However, technical challenges include the difficulties related to the construction and calibration of the sensor and a clinical limitation is that the source of light at those wavelengths induces heat to the tissue.

The results of classification suggest the differentiation of type of inflammation by multispectral imaging based on the acquisition system with a filter wheel. The statistical features are considered candidates for the differentiation of the pathology. However, there is no biological interpretation.

In the analysis of precancerous lesions with GEMS prototype we identify the wavebands between 460 and 580 nm as statistical significant and could help in the diagnosis of precancerous lesions. We consider that these bands are related to the oxygen saturation.

During the development of the premalignant lesions, we identify that there is a modification in the size of the scatters. We hypothesize that it is related to the collagen which is recruited during the inflammation to replace at a later point the glands in the gastric tissues that shrink or disappear due to the development of the pathology. More work is required to understand the biological mechanisms that are involved in the development of the pathology.

The classification with the acquisition system GEMS shows a low accuracy, which could be related to the low number of patients used for training the classifiers. Future studies should be oriented to create a database with a sufficient number of clinical cases with their pathological definition and spectral signatures. This kind of database could lead to the estimation of a model for pathological tissues in gastric mucosa, which includes biological variations due to age, genetic variation, background and symptoms displayed. Even though the construction of such database to study the pathology is utopic, it is clear that a main objective is the model of light tissue interaction which takes in consideration more biological parameters. The main challenge is to reach a model from which we can reflect the observed changes in histology. This kind of model will require the combination of different techniques available such as MiE diffusion theory, Monte Carlo modeling finite element for the mechanical interactions among others. Taking the spectrum as an input, the outcome is a transversal cut of the simulated tissue that could include biological parameters or representative features. These features could also display a statistical significance for the differentiation in a classification task.

The results from this preliminary study for gastritis and precancerous lesions are promising and we consider that in the future, they could be used for diagnosis. Some limitations should be noted such as the small number of samples, the fact that this study included only patients from single center. With respect to the acquisition system, we consider to increase the spectral and spatial resolution to include more wavebands in the NIR taking in consideration that these wavelengths could induce heat to the tissues. Additionally, it should also include a study on the ultraviolet. The vision in a short term for this system is to be used as an additional tool during gastroendoscopy that could help in the diagnosis by indicating areas of tissues which are more likely to have precancerous lesions so that the practitioner could decide to collect biopsies.

The development in a long term is the automatic identification of pathologies. We consider a CAD (Computer Aided Diagnosis) system which integrates models of light tissue interaction which achieves high level of confidence oriented to facilitate the diagnosis of diseases for the doctors. Additionally, this could also help in order to relieve the workload of pathologist. In the development of such systems, we must also consider the analysis cost-benefit. The benefits should always be oriented for the patient, such as a faster and more accurate diagnosis, with a treatment that brings the higher prognosis. On the other hand, the cost of medical equipment is relevant since it should cover norms in its development, characteristics, components, materials and protocols to be used. The

inclusion of a multispectral camera could provide a strong advantage for the gastroendoscopic system since it is considered low-invasive. For this kind of study it required to evaluate other pathologies and also include other wavebands.

Another direction of this study is that we can study the biological changes involved during the development of pathologies.

With respect to the histological analysis, it will remain as the main tool for diagnosis. We expect more automatic computer vision tools integrated in the microscopes in order to reduce interobservability by identifying the main histological structures which could be used for the diagnosis. This could include the segmentation of a specific glands or pattern in the architecture of the tissues. This kind of automation could help to study the size, shape, morphological appearance, architecture, distribution, etc. of the structures at each stage of the development of the pathology.

With the advance of new technologies, we expect other approaches for diagnosis, such as the gene therapy expression and imaging biomarkers through the blood. In this case, multispectral imaging could play an important role to help in the diagnosis and also to follow the treatment. Before reaching that point, the large pattern variety in the gene expression should be resolved.

Another perspective of this doctoral work is to consider extending this technology to diseases which are poorly identified during endoscopy. In particular, inflammatory bowel diseases where multispectral imaging could help in the diagnosis and in the evaluation of the treatment.

We strongly believe that a minimally invasive diagnostic based on multispectral imaging could help in the diagnosis of pathologies during endoscopy.

## Annexe. Synthèse

# Imagerie multispectrale pour améliorer la détection des lésions précancéreuses en endoscopie digestive

L'évolution de la gastrite et des lésions précancéreuses suit une cascade de plusieurs étapes. Les modifications des tissus pathologiques affichent de faibles variations par rapport à la muqueuse normale d'un point de vue macroscopique. Même si certaines variations pourraient être identifiées, cela reste fortement subjectif. Le diagnostic classique des maladies de l'estomac est divisé en deux procédures. La première est une gastroendoscopie où l'estomac est visuellement exploré sous une lumière blanche. La seconde est une biopsie pour l'analyse histologique. Cette procédure a une forte probabilité d'établir le diagnostic correct mais elle dépend fortement d'un bon prélèvement des échantillons de tissus endommagés.

Ce travail porte sur l'étude de la muqueuse gastrique par imagerie multispectrale. La contribution principale est une étude clinique sur la gastrite et les lésions précancéreuses mettant en évidence les changements dans le tissu. A cet effet, nous avons effectué une étude ex-vivo dans un modèle murin de l'infection de *Helicobacter pylori*. Nous avons identifié que les bandes délimitées entre 430 et 450 nm, entre 470 et 590 nm et entre 620 et 680 nm comme candidates pour le diagnostic. Elles peuvent être liées à des changements de la taille des particules diffusantes, à la concentration de sang et à l'augmentation de la saturation en oxygène.

Pour les études cliniques nous proposons deux prototypes d'imageurs multispectral compatibles avec les gastroendoscopes actuels pour acquérir des images du tissu gastrique : le premier est basé sur une roue à filtres et le deuxième sur une caméra multispectrale qui permet d'acquérir une image multispectrale de 7 canaux en *single shot* avec six bandes dans le visible et un dans le NIR.

A partir de l'étude clinique de la gastrite nous observons des patches laineux dans la bande de 560 nm chez certains patients atteints de gastrite et qui ne sont pas visibles chez les patients avec une muqueuse normale. De plus, les bandes au-dessus de 540 nm sont

identifiées comme candidates pour le diagnostic. Ces bandes peuvent être liées à la saturation en oxygène et la taille des particules diffusantes. Dans l'étude des lésions précancéreuses, les bandes entre 460 et 580 nm sont identifiées comme candidates pour le diagnostic. Ces bandes peuvent être liées à la saturation en oxygène. En plus, nous avons proposé une méthodologie pour identifier les tissus pathologiques, qui est basé sur des caractéristiques statistiques extraites des spectres acquis, classées en fonction de leur pouvoir discriminants et une classification supervisée où nous cherchons la meilleure performance de trois algorithmes de classification: le plus proche voisin, un réseaux de neurones et une Support Vector Machine avec une évaluation de la performance rigoureuse en utilisant une validation de type Leave One Patient Out Cross Validation.

Nous avons trouvé que la bande NIR pourrait aider dans le diagnostic car elle est liée à des changements dans la concentration de l'eau, la saturation en oxygène et la taille des particules diffusantes. En particulier, les tissus précancéreux peuvent inclure principalement de diffuseurs de petite taille. De plus, nous considérons également que les tissus précancéreux ont moins de saturation en oxygène que le tissu gastrique normal.

Les résultats de classification ont été satisfaisants pour le premier prototype d'acquisition, mais pas pour le système GEMS. Nous considérons que cette situation pourrait être liée au faible nombre de patients avec des conditions précancéreuses qui rend l'étape d'apprentissage difficile pour les classificateurs. Dans ce cas-là, nous considérons que d'autres études incluent plus de patients sont nécessaires.

Les résultats démontrent la pertinence de l'imagerie multispectrale comme un outil supplémentaire pour un diagnostic objectif.

# Bibliography

- [1] J. Ferlay, I. Soerjomataram, M. Ervik, R. Dikshit, S. Eser, C. Mathers, M. Rebelo, D. Parkin, D. Forman, and F. Bray, *GLOBOCAN 2012 v1.0, Cancer Incidence and Mortality Worldwide: IARC CancerBase No. 11*. Lyon, France: International Agency for Research on Cancer, 2013.
- [2] T. Kamada, K. Haruma, M. Ito, K. Inoue, N. Manabe, H. Matsumoto, H. Kusunoki, J. Hata, M. Yoshihara, K. Sumii, T. Akiyama, S. Tanaka, A. Shiotani, and D. Y. Graham, "Time Trends in *Helicobacter pylori* Infection and Atrophic Gastritis Over 40 Years in Japan," *Helicobacter*, vol. 20, no. 3, pp. 192–198, 2015.
- [3] S.-M. Lee, K.-M. Kim, and J. Y. Ro, "Gastric Carcinoma: Morphologic Classifications and Molecular Changes," in *Gastric Carcinoma. New insights into Current Management*, D. Lazar, Ed. INTECH open science, 2013.
- [4] C. Gonen, I. Simsek, S. Sarioglu, and H. Akpinar, "Comparison of high resolution magnifying endoscopy and standard videoendoscopy for the diagnosis of *Helicobacter pylori* gastritis in routine clinical practice: a prospective study," *Helicobacter*, vol. 14, no. 1, pp. 12–21, Feb. 2009.
- [5] M. N. Gurcan, L. E. Boucheron, A. Can, A. Madabhushi, N. M. Rajpoot, and B. Yener, "Histopathological Image Analysis: A Review," *Biomed. Eng. IEEE Rev. In*, vol. 2, pp. 147–171, 2009.
- [6] D. W. Hay, "Stomach and Duodenum," in *The little black book of gastroenterology*, 2nd ed., Jones and Bartlett Publishers, 2002.
- [7] S. Tomatis, M. Carrara, A. Bono, C. Bartoli, M. Lualdi, G. Tragni, Ambrogio Colombo, and R. Marchesini, "Automated melanoma detection with a novel multispectral imaging system: results of a prospective study," *Phys. Med. Biol.*, vol. 50, no. 8, p. 1675, 2005.
- [8] M. Abeloff, *Abeloff's Clinical Oncology*, 4th ed. Churchill Livingstone/Elsevier, 2008.
- [9] P. Correa and M. B. Piazuelo, "The gastric precancerous cascade," *J. Dig. Dis.*, vol. 13, no. 1, pp. 2–9, 2012.
- [10] W. Nel, "Gastritis and gastropathy: More than meets the eye," *Contin. Med. Educ.*, vol. 30, no. 2, 2012.
- [11] D. A. Israel and R. M. Peek, "Review article: pathogenesis of *Helicobacter pylori*-induced gastric inflammation," *Aliment. Pharmacol. Ther.*, vol. 15, no. 9, pp. 1271–1290, 2001.
- [12] J. G. Kusters, A. H. M. van Vliet, and E. J. Kuipers, "Pathogenesis of *Helicobacter pylori* Infection," *Clin. Microbiol. Rev.*, vol. 19, no. 3, pp. 449–490, Jul. 2006.
- [13] G. Di Febo, C. Calabrese, G. Brandi, A. M. Morselli-Labate, A. Areni, M. Gandolfi, G. Biasco, and M. Miglioli, "Endoscopy fails in identifying the presence of *Helicobacter pylori* (Hp) in gastric antrum of adults," *Gastroenterology*, vol. 114, p. A103.
- [14] J. C. Atherton and M. J. Blaser, "*Helicobacter pylori* infections," in *Harrison's Gastroenterology and Hepatology*, D. L. Longo and A. S. Fauci, Eds. McGraw-Hill, 2010.
- [15] *IARC monographs on the evaluation of carcinogenic risk to humans, schistosomes, liver flukes and Helicobacter pylori*, vol. 61. World Health Organization, International Agency for Research on Cancer, 1994.
- [16] W. Shin, H. Kim, H. Song, S. Hong, K.-N. Shim, I.-K. Sung, and J. Kim, "Surveillance Strategy of Atrophic Gastritis and Intestinal Metaplasia in a Country with a High Prevalence of Gastric Cancer," *Dig. Dis. Sci.*, vol. 57, no. 3, pp. 746–752, 2012.
- [17] R. Dirnu, F. A. Secureanu, C. Neamtu, B. D. Totolici, O. T. Pop, P. Mitrut, D. G. Malaescu, and L. Mogoanta, "Chronic gastritis with intestinal metaplasia: clinico-statistical, histological and immunohistochemical study," *Rom J Morphol Embryol*, vol. 53, no. 2, pp. 293–7, 2012.

- [18] S. Hayashi, J. Imamura, K. Kimura, S. Saeki, and T. Hishima, "Endoscopic features of lymphoid follicles in *Helicobacter pylori*-associated chronic gastritis," *Dig. Endosc.*, vol. 27, no. 1, pp. 53–60, 2015.
- [19] L. Gutiérrez-González and N. A. Wright, "Biology of intestinal metaplasia in 2008: More than a simple phenotypic alteration," *Dig. Liver Dis.*, vol. 40, no. 7, pp. 510–522.
- [20] J. H. Lim, N. Kim, H. S. Lee, G. Choe, S. Y. Jo, I. Chon, C. Choi, H. Yoon, C. M. Shin, Y. S. Park, D. H. Lee, and H. C. Jung, "Correlation between Endoscopic and Histological Diagnoses of Gastric Intestinal Metaplasia," *Gut Liver*, vol. 7, no. 1, pp. 41–50, Jan. 2013.
- [21] P. Correa, M. B. Piazuelo, and K. T. Wilson, "Pathology of Gastric Intestinal Metaplasia: Clinical Implications," *Am. J. Gastroenterol.*, vol. 105, no. 3, pp. 493–498, Mar. 2010.
- [22] J. L. Madara and J. M. Anderson, "Epithelial: Biological principles of organization," in *Textbook of gastroenterology*, T. Yamada, D. H. Alpers, L. Laine, N. Kaplowitz, C. Owyang, and D. W. Powell, Eds. Lippincott Williams & Wilkins Publishers.
- [23] K. Tominaga, S. Fujinuma, T. Endo, Y. Saida, K. Takahashi, and I. Maetani, "Efficacy of the revised Vienna Classification for diagnosing colorectal epithelial neoplasias," *World J. Gastroenterol.*, vol. 15, no. 19, May 2009.
- [24] P. A. Kenny, *The biology of cancer: Stages of cancer development*, 1st ed. Chelsea House, 2007.
- [25] M. Stolte, "The new Vienna classification of epithelial neoplasia of the gastrointestinal tract: advantages and disadvantages," *Virchows Arch.*, vol. 442, no. 2, pp. 99–106, 2003.
- [26] M. Rugge, L. G. Capelle, R. Cappellesso, D. Nitti, and E. J. Kuipers, "Precancerous lesions in the stomach: From biology to clinical patient management," *Best Pract. Res. Clin. Gastroenterol.*, vol. 27, no. 2, pp. 205 – 223, 2013.
- [27] N. Goseki, T. Takizawa, and M. Koike, "Differences in the mode of the extension of gastric cancer classified by histological type: new histological classification of gastric carcinoma.," in *Gut*, vol. 33, 1992, pp. 606–612.
- [28] T. Takahashi, Y. Saikawa, and Y. Kitagawa, "Gastric Cancer: Current Status of Diagnosis and Treatment," *Cancers*, vol. 5, no. 1, p. 48, 2013.
- [29] H. M. El-Zimaity and D. Y. Graham, "Evaluation of gastric mucosal biopsy site and number for identification of *Helicobacter pylori* or intestinal metaplasia: role of the Sydney System," *Hum Pathol*, vol. 30, no. 1, pp. 72–7, Jan. 1999.
- [30] A. C. de Vries, J. Haringsma, R. A. de Vries, F. Ter Borg, N. C. T. van Grieken, G. A. Meijer, H. van Dekken, and E. J. Kuipers, "Biopsy strategies for endoscopic surveillance of pre-malignant gastric lesions," *Helicobacter*, vol. 15, no. 4, pp. 259–264, Aug. 2010.
- [31] L. G. Capelle, J. Haringsma, A. C. Vries, E. W. Steyerberg, K. Biermann, H. Dekken, and E. J. Kuipers, "Narrow Band Imaging for the Detection of Gastric Intestinal Metaplasia and Dysplasia During Surveillance Endoscopy," *Dig. Dis. Sci.*, vol. 55, no. 12, pp. 3442–3448, 2010.
- [32] R. Lambert, "Endoscopy in screening for digestive cancer," *World J. Gastrointest. Endosc.*, vol. 4, no. 12, pp. 518–525, Dec. 2012.
- [33] M. F. Dixon, R. M. Genta, J. H. Yardley, and P. Correa, "Classification and grading of gastritis. The updated Sydney System. International Workshop on the Histopathology of Gastritis, Houston 1994," *Am J Surg Pathol*, vol. 20, no. 10, pp. 1161–81, Oct. 1996.
- [34] R. M. Genta, "Chapter 68. Gastritis and Gastropathy," in *Textbook of Gastroenterology*, Lippincott Williams & Wilkins., T. Yamada, D. H. Alpers, N. Kaplowitz, L. Laine, C. Owyang, and D. W. Powell, Eds. 2003.
- [35] M. Dinis-Ribeiro, M. Areia, A. C. de Vries, R. Marcos-Pinto, M. Monteiro-Soares, A. O'Connor, C. Pereira, P. Pimentel-Nunes, R. Correia, A. Ensari, J. M. Dumonceau, J. C. Machado, G. Macedo, P. Malfertheiner, T. Matysiak-Budnik, F. Megraud, K. Miki, C. O'Morain, R. M. Peek, T. Ponchon, A. Ristimaki, B. Rembacken, F. Carneiro, E. J. Kuipers, European Society of Gastrointestinal Endoscopy, European *Helicobacter* Study Group, European Society of Pathology, and Sociedade Portuguesa de Endoscopia Digestiva, "Management of precancerous conditions and lesions in the stomach (MAPS): guideline from the European Society of Gastrointestinal Endoscopy (ESGE), European *Helicobacter* Study Group (EHSg), European Society of Pathology (ESP), and

- the Sociedade Portuguesa de Endoscopia Digestiva (SPED)," *Endoscopy*, vol. 44, no. 1, pp. 74–94, Jan. 2012.
- [36] L. G. Capelle, A. C. de Vries, J. Haringsma, F. Ter Borg, R. A. de Vries, M. J. Bruno, H. van Dekken, J. Meijer, N. C. van Grieken, and E. J. Kuipers, "The staging of gastritis with the OLGA system by using intestinal metaplasia as an accurate alternative for atrophic gastritis," *Gastrointest Endosc*, vol. 71, no. 7, pp. 1150–8, Jun. 2010.
- [37] M. Rugge, M. de Boni, G. Pennelli, M. de Bona, L. Giacomelli, M. Fassan, D. Basso, M. Plebani, and D. Y. Graham, "Gastritis OLGA-staging and gastric cancer risk: a twelve-year clinico-pathological follow-up study," *Aliment Pharmacol Ther*, vol. 31, no. 10, pp. 1104–11, May 2010.
- [38] L. M. Wong Kee Song, D. G. Adler, J. D. Conway, D. L. Diehl, F. A. Farraye, S. V. Kantsevov, R. Kwon, P. Mamula, B. Rodriguez, R. J. Shah, and W. M. Tierney, "Narrow band imaging and multiband imaging," *Gastrointest. Endosc.*, vol. 67, no. 4, pp. 581–589, 2008.
- [39] S. C. Reddymasu and P. Sharma, "Advances in Endoscopic Imaging of the Esophagus," *Gastroenterol. Clin. North Am.*, vol. 37, no. 4, pp. 763 – 774, 2008.
- [40] R. Singh, Owen V., A. Shonde, P. Kaye, C. Hawkey, and K. Ragunath, "White light endoscopy, narrow band imaging and chromoendoscopy with magnification in diagnosing colorectal neoplasia," *World J. Gastrointest. Endosc.*, vol. 1, no. 1, pp. 45–50, 2009.
- [41] L. M. Wong Kee Song, D. G. Adler, B. Chand, J. D. Conway, J. M. B. Croffie, J. A. DiSario, D. S. Mishkin, R. J. Shah, L. Somogyi, W. M. Tierney, and B. T. Petersen, "Chromoendoscopy," *Gastrointest. Endosc.*, vol. 66, no. 4, pp. 639 – 649, 2007.
- [42] P. Pimentel-Nunes, M. Dinis-Ribeiro, J. B. Soares, R. Marcos-Pinto, C. Santos, C. Rolanda, R. P. Bastos, M. Areia, L. Afonso, J. Bergman, P. Sharma, T. Gotoda, R. Henrique, and L. Moreira-Dias, "A multicenter validation of an endoscopic classification with narrow band imaging for gastric precancerous and cancerous lesions," *Endoscopy*, vol. 44, no. 3, pp. 236–246, Mar. 2012.
- [43] H. Osawa, H. Yamamoto, Y. Miura, M. Yoshizawa, K. Sunada, K. Satoh, and K. Sugano, "Diagnosis of extent of early gastric cancer using flexible spectral imaging color enhancement," *World J. Gastrointest. Endosc.*, vol. 4, no. 8, pp. 356–361, Aug. 2012.
- [44] I. Kikuste, R. Marques-Pereira, M. Monteiro-Soares, P. Pimentel-Nunes, M. Areia, M. Leja, and M. Dinis-Ribeiro, "Systematic review of the diagnosis of gastric premalignant conditions and neoplasia with high-resolution endoscopic technologies," *Scand. J. Gastroenterol.*, vol. 48, no. 10, pp. 1108–1117, Oct. 2013.
- [45] G. Gershman and M. Ament, *Practical Pediatric Gastrointestinal Endoscopy*. Blackwell publishing, 2007.
- [46] J. Cohen, *Successful training in Gastrointestinal Endoscopy*. Blackwell publishing, 2011.
- [47] M. Iwatate, T. Ikumoto, S. Hattori, W. Sano, Y. Sano, and T. Fujimori, "NBI and NBI Combined with Magnifying Colonoscopy," *Diagn. Ther. Endosc.*, vol. 2012, 2012.
- [48] M. Kida, K. Kobayashi, and K. Saigenji, "Routine Chromoendoscopy for Gastrointestinal Diseases: Indications Revised," *Endoscopy*, vol. 35, no. 7, pp. 590–596, 2003.
- [49] G. S. Henderson, D. R. Neuville, R. T. Downs, and M. S. of America, *Spectroscopic Methods in Mineralogy and Material Sciences*. Mineralogical Society of America, 2014.
- [50] B. Raychaudhuri, "Imaging spectroscopy: Origin and future trends," *Appl. Spectrosc. Rev.*, vol. 51, no. 1, pp. 23–35, 2016.
- [51] H. Workman and J. Workman, *Statistics in spectroscopy*, Elsevier Academic Press. 2003.
- [52] C. Balas, "Review of biomedical optical imaging—a powerful, non-invasive, non-ionizing technology for improving in vivo diagnosis," *Meas. Sci. Technol.*, vol. 20, no. 10, p. 104020, 2009.
- [53] Q. Li, X. He, Y. Wang, H. Liu, D. Xu, and F. Guo, "Review of spectral imaging technology in biomedical engineering: achievements and challenges," *J. Biomed. Opt.*, vol. 18, no. 10, pp. 100901–100901, 2013.
- [54] R. Leitner, M. D. Biasio, T. Arnold, C. V. Dinh, M. Loog, and R. P. W. Duin, "Multi-spectral video endoscopy system for the detection of cancerous tissue," *Pattern Recognit. Lett.*, vol. 34, no. 1, pp. 85 – 93, 2013.



- [55] C. Simon Chane, A. Mansouri, F. S. Marzani, and F. Boochs, "Integration of 3D and multispectral data for cultural heritage applications: Survey and perspectives," *Image Vis. Comput.*, vol. 31, no. 1, pp. 91–102, Jan. 2013.
- [56] E. Reinhard, E. A. Khan, A. O. Akyuz, and G. Johnson, *Color imaging. Fundamentals and applications*. A K Peters, 2008.
- [57] A. Ryer, *Light measurement handbook*, International Light, Inc. International Light, 1997.
- [58] G. Lu and B. Fei, "Medical hyperspectral imaging: a review," *J. Biomed. Opt.*, vol. 19, no. 1, pp. 010901–010901, 2014.
- [59] R. Liang, *Optical design for biomedical imaging*. SPIE press, 2010.
- [60] S. L. Jacques, "Optical properties of biological tissues: a review," *Phys. Med. Biol.*, vol. 58, no. 11, pp. R37–R61, Jun. 2013.
- [61] S. L. Jacques, R. Samatham, and N. Choudhury, "Rapid spectral analysis for spectral imaging," *Biomed. Opt. Express*, vol. 1, no. 1, pp. 157–164, Aug. 2010.
- [62] L. Yang and B. Kruse, "Revised Kubelka–Munk theory. I. Theory and application," *J Opt Soc Am A*, vol. 21, no. 10, pp. 1933–1941, Oct. 2004.
- [63] T. J. Farrell, M. S. Patterson, and B. Wilson, "A diffusion theory model of spatially resolved, steady-state diffuse reflectance for the noninvasive determination of tissue optical properties invivo," *Med. Phys.*, vol. 19, no. 4, pp. 879–888, 1992.
- [64] A. N. Bashkatov, E. A. Genina, V. I. Kochubey, A. A. Gavrilova, S. V. Kapralov, V. A. Grishaev, and V. V. Tuchin, "Optical properties of human stomach mucosa in the spectral range from 400 to 2000 nm: Prognosis for gastroenterology," *Med. Laser Appl.*, vol. 22, no. 2, pp. 95–104, Oct. 2007.
- [65] B. C. Wilson and S. L. Jacques, "Optical reflectance and transmittance of tissues: principles and applications," *Quantum Electron. IEEE J. Of*, vol. 26, no. 12, pp. 2186–2199, Dec. 1990.
- [66] D. S. Gareau, F. Truffer, K. A. Perry, T. H. Pham, C. K. Enestvedt, J. P. Dolan, J. G. Hunter, and S. L. Jacques, "Optical fiber probe spectroscopy for laparoscopic monitoring of tissue oxygenation during esophagectomies," *J. Biomed. Opt.*, vol. 15, no. 6, pp. 061712–061712–6, 2010.
- [67] P. R. Bargo, S. A. Prahl, T. T. Goodell, R. A. Steven, G. Koval, G. Blair, and S. L. Jacques, "In vivo determination of optical properties of normal and tumor tissue with white light reflectance and an empirical light transport model during endoscopy," *J. Biomed. Opt.*, vol. 10, no. 3, pp. 034018–03401815, 2005.
- [68] K. M. Giraev, N. A. Ashurbekov, and M. A. Lakhina, "Optical absorption and scattering spectra of pathological stomach tissues," *J. Appl. Spectrosc.*, vol. 78, no. 1, pp. 95–102, 2011.
- [69] J. Galeano, R. Jolivot, Y. Benezeth, F. Marzani, J. F. Emile, and D. Lamarque, "Analysis of Multispectral Images of Excised Colon Tissue Samples Based on Genetic Algorithms," in *Signal Image Technology and Internet Based Systems (SITIS), 2012 Eighth International Conference on*, 2012, pp. 833–838.
- [70] E. Claridge and D. Hidovic-Rowe, "Model Based Inversion for Deriving Maps of Histological Parameters Characteristic of Cancer From Ex-Vivo Multispectral Images of the Colon," *Med. Imaging IEEE Trans. On*, vol. 33, no. 4, pp. 822–835, Apr. 2014.
- [71] P. Sprent and N. C. Smeeton, *Applied nonparametric statistical methods*, 3rd ed. Taylor And Francis, 2000.
- [72] M. Neuhäuser, *Nonparametric Statistical Tests, a computational approach*. CRC Press, 2012.
- [73] J. D. Gibbons and S. Chakraborti, *Nonparametric statistical inference*, 5th ed. CRC Press, 2010.
- [74] G. James, D. Witten, T. Hastie, and R. Tibshirani, *An introduction to statistical learning with applications in R*, vol. 103. Springer, 2013.
- [75] P. H. Westfall and S. Young, *Resampling-Based Multiple Testing: Examples and Methods for P-Value Adjustment*. Wiley, 1992.
- [76] M. Hollander and D. A. Wolfe, *Nonparametric statistical methods*, 2nd ed. Wiley, 1999.
- [77] O. Zak and M. A. Sande, Eds., *Handbook of animal models of infection*, Academic Press. 1999.
- [78] D. Manolakis, R. Lockwood, T. Cooley, and J. Jacobson, "Is there a best hyperspectral detection algorithm?," 2009, pp. 733402–733402–16.

- [79] Y. Du, C.-I. Chang, H. Ren, C.-C. Chang, J. O. Jensen, and F. M. D'Amico, "New hyperspectral discrimination measure for spectral characterization," *Opt. Eng.*, vol. 43, pp. 1777–1786, Aug. 2004.
- [80] H. Akbari, K. Uto, Y. Kosugi, K. Kojima, and N. Tanaka, "Cancer detection using infrared hyperspectral imaging," *Cancer Sci.*, vol. 102, no. 4, pp. 852–857, 2011.
- [81] C. Lee and D. A. Landgrebe, "Analyzing high-dimensional multispectral data," *Geosci. Remote Sens. IEEE Trans. On*, vol. 31, no. 4, pp. 792–800, Jul. 1993.
- [82] I. Guyon and A. Elisseeff, "An Introduction to Variable and Feature Selection," *J Mach Learn Res*, vol. 3, pp. 1157–1182, Mar. 2003.
- [83] I. Guyon, S. Gunn, M. Nikravesh, and L. A. Zadeh, *Feature Extraction, foundations and applications*, 1st ed. Springer-Verlag Berlin Heidelberg, 2006.
- [84] Y. Saeys, I. Inza, and P. Larrañaga, "A review of feature selection techniques in bioinformatics," *Bioinformatics*, vol. 23, no. 19, pp. 2507–2517, 2007.
- [85] R. Kohavi and G. H. John, "Wrappers for feature subset selection," *Artif. Intell.*, vol. 97, no. 1–2, pp. 273 – 324, 1997.
- [86] T. Hastie, R. Tibshirani, and J. Friedman, *The Elements of Statistical Learning. Data Mining, Inference, and Prediction*, 2nd ed. Springer, 2009.
- [87] Y. Kim and J. Kim, "Gradient LASSO for Feature Selection," in *Proceedings of the Twenty-first International Conference on Machine Learning*, New York, NY, USA, 2004, p. 60–.
- [88] D. Barber, *Bayesian Reasoning and Machine Learning*. Cambridge University Press, 2012.
- [89] T. S. Furey, N. Cristianini, N. Duffy, D. W. Bednarski, M. Schummer, and D. Haussler, "Support vector machine classification and validation of cancer tissue samples using microarray expression data," *Bioinformatics*, vol. 16, no. 10, pp. 906–914, 2000.
- [90] B. Hammer and T. Villmann, "Generalized relevance learning vector quantization," *Neural Netw.*, vol. 15, no. 8–9, pp. 1059 – 1068, 2002.
- [91] P. Schneider, M. Biehl, and B. Hammer, "Distance Learning in Discriminative Vector Quantization," *Neural Comput.*, vol. 21, no. 10, pp. 2942–2969, Jul. 2009.
- [92] A. Sato and K. Yamada, "Generalized Learning Vector Quantization," in *Advances in Neural Information Processing Systems 8, NIPS, Denver, CO, November 27-30, 1995*, 1995, pp. 423–429.
- [93] M. Strickert, U. Seiffert, N. Sreenivasulu, W. Weschke, T. Villmann, and B. Hammer, "Generalized relevance {LVQ} (GRLVQ) with correlation measures for gene expression analysis," *Neurocomputing*, vol. 69, no. 7–9, pp. 651 – 659, 2006.
- [94] T. Villmann, F. Schleif, and B. Hammer, "Comparison of relevance learning vector quantization with other metric adaptive classification methods," *Neural Netw.*, vol. 19, no. 5, pp. 610 – 622, 2006.
- [95] G. Xu and J. Z. Huang, "Asymptotic optimality and efficient computation of the leave-subject-out cross-validation," *Ann. Statist.*, pp. 3003 – 3030, 2012.
- [96] I. J. Bigio and J. R. Mourant, Eds., *Optical Biopsy*. Marcel Dekker Press, 2003.
- [97] E. P. Costa, A. C. Lorena, A. C. P. L. F. Carvalho, and A. A. Freitas, "A review of performance evaluation measures for hierarchical classifiers.," in *Evaluation Methods for Machine Learning II: papers from the AAAI-2007 Workshop, AAAI Technical Report WS-07-05*, 2007, pp. 182–196.
- [98] A. Rogers and J. Houghton, "Helicobacter -Based Mouse Models of Digestive System Carcinogenesis," in *Inflammation and Cancer*, vol. 511, S. Kozlov, Ed. Humana Press, 2009, pp. 267–295.
- [99] A. Lee, J. O'Rourke, M. D. Ungria, B. Robertson, G. Daskalopoulos, and M. F. Dixon, "A standardized mouse model of Helicobacter pylori infection: Introducing the Sydney strain," *Gastroenterology*, vol. 112, no. 4, pp. 1386 – 1397, 1997.
- [100] J. M. Houghton, Ed., *Helicobacter species, methods and protocols*. London: Springer, 2012.
- [101] R. H. Hunt, "The Role of Helicobacter pylori in Pathogenesis: the Spectrum of Clinical Outcomes," *Scand. J. Gastroenterol.*, vol. 31, no. s220, pp. 3–9, 1996.

- [102] R. L. Ferrero, J.-M. Thiberge, M. Huerre, and A. Labigne, "Immune Responses of Specific-Pathogen-Free Mice to Chronic *Helicobacter pylori* (Strain SS1) Infection," *Infect. Immun.*, vol. 66, no. 4, pp. 1349–1355, Apr. 1998.
- [103] T. Yamada, *Textbook of gastroenterology*, 4th ed. Lippincott Williams & Wilkins Publishers, 2003.
- [104] S. Zhang and S. Moss, "Rodent Models of *Helicobacter* Infection, Inflammation, and Disease," in *Helicobacter Species*, vol. 921, J. Houghton, Ed. Humana Press, 2012, pp. 89–98.
- [105] E. B. Prophet and A. F. I. of P. (U.S.), *Laboratory methods in histotechnology*. American Registry of Pathology, 1992.
- [106] K. A. Eaton, M. J. Radin, and S. Krakowka, "An Animal Model of Gastric Ulcer Due to Bacterial Gastritis in Mice," *Vet. Pathol. Online*, vol. 32, no. 5, pp. 489–497, 1995.
- [107] R. Szeliski, *Computer Vision. Algorithms and Applications*, 1st ed. Springer-Verlag London, 2011.
- [108] R. Rubin, D. S. Strayer, E. Rubin, and J. M. McDonald, *Rubin's Pathology: Clinicopathologic Foundations of Medicine*. Lippincott Williams & Wilkins, 2008.
- [109] L. L. Lambrichs, *La vérité médicale: Claude Bernard, Louis Pasteur, Sigmund Freud, légendes et réalités de notre médecine*. Robert Laffont, 1993.
- [110] S. Hegenbart, A. Uhl, G. Wimmer, and A. Vecsei, "On the effects of de-interlacing on the classification accuracy of interlaced endoscopic videos with indication for celiac disease," in *Computer-Based Medical Systems (CBMS), 2013 IEEE 26th International Symposium on*, 2013, pp. 137–142.
- [111] K. Zuiderveld, "Contrast Limited Adaptive Histogram Equalization," in *Graphics Gems IV*, P. S. Heckbert, Ed. San Diego, CA, USA: Academic Press Professional, Inc., 1994, pp. 474–485.
- [112] B. Kurt, V. V. Nabiyev, and K. Turhan, "Medical images enhancement by using anisotropic filter and CLAHE," in *Innovations in Intelligent Systems and Applications (INISTA), 2012 International Symposium on*, 2012, pp. 1–4.
- [113] L. G. More, M. A. Brizuela, H. L. Ayala, D. P. Pinto-Roa, and J. L. V. Noguera, "Parameter tuning of CLAHE based on multi-objective optimization to achieve different contrast levels in medical images," in *Image Processing (ICIP), 2015 IEEE International Conference on*, 2015, pp. 4644–4648.
- [114] A. J. Vyavahare and R. C. Thool, "Segmentation using region growing algorithm based on CLAHE for medical images," in *Communication and Computing (ARTCom2012), Fourth International Conference on Advances in Recent Technologies in*, 2012, pp. 182–185.
- [115] J. Bergen, P. Anandan, K. Hanna, and R. Hingorani, "Hierarchical model-based motion estimation," in *Computer Vision — ECCV'92*, vol. 588, G. Sandini, Ed. Springer Berlin Heidelberg, 1992, pp. 237–252.
- [116] K. Yao, T. Yao, T. Matsui, A. Iwashita, and T. Oishi, "Hemoglobin content in intramucosal gastric carcinoma as a marker of histologic differentiation: a clinical application of quantitative electronic endoscopy," *Gastrointest. Endosc.*, vol. 52, no. 2, pp. 241–245, Aug. 2000.
- [117] A. Goto, J. Nishikawa, S. Kiyotoki, M. Nakamura, J. Nishimura, T. Okamoto, H. Ogihara, Y. Fujita, Y. Hamamoto, and I. Sakaida, "Use of hyperspectral imaging technology to develop a diagnostic support system for gastric cancer," *J. Biomed. Opt.*, vol. 20, no. 1, pp. 016017–016017, 2015.
- [118] A. Filer, K. Raza, M. Salmon, and C. D. Buckley, "Targeting Stromal Cells in Chronic Inflammation," *Discov. Med.*, vol. 7, no. 37, pp. 20–26, Feb. 2007.
- [119] A. J. Naylor, A. Filer, and C. D. Buckley, "The role of stromal cells in the persistence of chronic inflammation," *Clin. Exp. Immunol.*, vol. 171, no. 1, pp. 30–35, 2013.
- [120] H. M. McGettrick, L. M. Butler, C. D. Buckley, G. Ed Rainger, and G. B. Nash, "Tissue stroma as a regulator of leukocyte recruitment in inflammation," *J. Leukoc. Biol.*, vol. 91, no. 3, pp. 385–400, 2012.
- [121] J. E. Bender, A. B. Shang, E. W. Moretti, B. Yu, L. M. Richards, and N. Ramanujam, "Noninvasive monitoring of tissue hemoglobin using UV-VIS diffuse reflectance spectroscopy: a pilot study," *Opt Express*, vol. 17, no. 26, pp. 23396–23409, Dec. 2009.

- [122] R. Akbani, S. Kwek, and N. Japkowicz, "Applying Support Vector Machines to Imbalanced Datasets," in *Machine Learning: ECML 2004: 15th European Conference on Machine Learning, Pisa, Italy, September 20-24, 2004. Proceedings*, J.-F. Boulicaut, F. Esposito, F. Giannotti, and D. Pedreschi, Eds. Berlin, Heidelberg: Springer Berlin Heidelberg, 2004, pp. 39–50.
- [123] A. A. STOLOV, "Sterilization Effects on Optical Fibers for Clinical Use," *BioPhotonics*, Sep-2015.





**Titre :** Imagerie multispectrale pour améliorer la détection des lésions précancéreuses en endoscopie digestive

**Mots clés :** Apprentissage automatique, informatique de l'image, endoscopie, traitement du signal, gastritis

**Résumé :** L'évolution de la gastrite et des lésions précancéreuses suit une cascade de plusieurs étapes. Les modifications des tissus pathologiques affichent de faibles variations par rapport à la muqueuse normale d'un point de vue macroscopique. Même si certaines variations pourraient être identifiées, cela reste fortement subjectif. Le diagnostic classique des maladies de l'estomac est divisé en deux procédures. Le premier est une gastroendoscopie où l'estomac est visuellement exploré sous une lumière blanche. Le second est la biopsie pour l'analyse histologique. Cette procédure a une forte probabilité d'établir le diagnostic correct mais il dépend fortement de la sélection correcte des échantillons de tissus endommagés.

Ce travail porte sur l'étude de la muqueuse gastrique par imagerie multispectrale. La contribution principale est l'étude clinique de l'imagerie multispectrale afin de différencier les pathologies mal diagnostiquées ou qui ne peuvent être diagnostiquées que par l'analyse histologique. A cet effet, nous avons effectué (1) une étude ex-vivo dans

un modèle de souris de l'infection de *Helicobacter pylori* dans le but d'identifier les longueurs d'onde qui pourraient être utilisées pour le diagnostic. (2) Nous proposons deux prototypes compatibles avec les gastroendoscopes actuels pour acquérir des images multispectrales du tissu gastrique : le premier est basé sur une roue à filtres et le second sur une caméra multispectrale avec sept canaux. De plus, (3) nous présentons une méthodologie pour identifier les tissus pathologiques, qui est basé sur des caractéristiques statistiques extraites des spectres acquis, classées en fonction de leur pouvoir discriminants et une classification supervisée, où nous cherchons la meilleure performance de trois algorithmes de classification: le plus proche voisin, un réseaux de neurones et une Support Vector Machine avec une évaluation de la performance rigoureuse en utilisant une validation de type Leave One Patient Out Cross Validation. Les résultats démontrent la pertinence de l'imagerie multispectrale comme un outil supplémentaire pour un diagnostic objectif.

**Title :** Multispectral imaging to improve the detection of precancerous lesions in digestive endoscopy

**Key words :** Machine learning, computer vision, endoscopy, signal processing, gastritis

**Abstract:** The evolution of gastritis into precancerous lesions follows a cascade of multiple stages. The modifications of the pathological tissues display low variations with respect to normal mucosa from a macroscopical point of view. Even though some features could be identified, they remain strongly subjective. The current gold standard for diagnosis of gastric diseases is divided in two procedures. The first one is gastroendoscopy where the stomach is visually explored under white light. The second one is biopsy collection for histological analysis. This procedure has a high probability of establishing the correct diagnosis but it strongly depends on the accurate collection of samples from damaged tissues.

This doctoral work focuses on the study of gastric mucosa by multispectral imaging. The main contribution is the clinical study of multispectral imaging to differentiate pathologies poorly diagnosed or that can only be diagnosed by

histological analysis. For this purpose, we performed (1) ex vivo studies in a mice model of infection of *Helicobacter pylori* in order to identify the wavelengths which could be used for diagnosis. (2) We propose two prototypes compatible with current gastroendoscopes to acquire multispectral images from gastric tissue: the first one is based on a filter wheel and the second one on a multispectral camera with seven channels. Additionally, (3) we present a methodology to identify pathological tissues, which is based on statistical features extracted from the acquired spectra, ranked according to their discriminative power and a supervised classification, where we search for the best performance of three classification algorithms: Nearest Neighbor, Neural Networks and Support Vector Machine with a rigorous performance evaluation by using leave one patient out cross validation. The results demonstrate the relevance of multispectral imaging as an additional tool for an objective diagnosis.

